

Carnegie Mellon University
MELLON COLLEGE OF SCIENCE

THESIS

SUBMITTED IN PARTIAL FULFILLMENT OF THE REQUIREMENTS
FOR THE DEGREE OF

DOCTOR OF PHILOSOPHY IN THE FIELD OF PHYSICS

TITLE: "Electric field control of magnetization switching in magnetic tunnel junctions"

PRESENTED BY: Mukund Bapna

ACCEPTED BY THE DEPARTMENT OF PHYSICS

Sara Majetich	4/19/18
SARA MAJETICH, CHAIR PROFESSOR	DATE

Scott Dodelson	4/19/18
SCOTT DODELSON, DEPT HEAD	DATE

APPROVED BY THE COLLEGE COUNCIL

Rebecca Doerge	4/20/18
REBECCA DOERGE, DEAN	DATE

ELECTRIC FIELD CONTROL OF MAGNETIZATION SWITCHING IN MAGNETIC TUNNEL JUNCTIONS

A dissertation submitted
to Carnegie Mellon University in partial
fulfillment of the requirements for the
degree of Doctor of Philosophy

by
Mukund Bapna
April 2018

Doctoral dissertation written by

Mukund Bapna

M.S., Carnegie Mellon University, Pittsburgh PA, USA 2015

B.S. M.S. Dual Degree, Indian Institute of Science Education and Research Bhopal,
India, 2013

© 2018 Mukund Bapna

ALL RIGHTS RESERVED

Dedication

To my dear Dadaji and Nanaji

Acknowledgments

There's been a strong influence of my teachers, colleagues, family, and friends on my research work that has culminated in this thesis, some influences were not so direct and apparent than others, but were crucial.

First and foremost, I would like to thank my advisor Prof. Sara Majetich who has been a source of constant guidance and motivation. She is an authority in the field of magnetism and magnetic materials. Her knowledge of wide range of magnetic materials and experimental techniques is staggering. I am lucky to have had the opportunity to work under her supervision and learn from her. She firmly believed in me and my capability to excel in research. She monitored my progress closely and took time to meet with me frequently each week or as her busy schedule would permit. With her supervision, I never felt lost in research even when things were not working the way I was hoping. She was always very prompt at getting back with feedbacks that significantly accelerated my research work. Each manuscript that I wrote under her supervision has gone through multiple iterations of corrections and this, in turn, has improved my scientific writing skills manifolds. Her attention to details and emphasis on clarity is truly impressive. Sara is a leader by example; she works hard along with the students.

I am also very thankful to my group members- Stephan Piotrowski, Samuel Oberdick, Brad Parks, and Ahmed Abdelgawad who were all very pleasant personalities to work with. Thanks to Stephan Piotrowski who diligently trained me on the Conductive atomic force microscope and several tools in the nanofabrication facility which I used extensively in my research. Stephan had impressive Matlab

coding skills and I got to learn some from him. I am thankful to Sam Oberdick who taught me electron beam lithography and ion milling which I later extensively used in preparing samples needed for my research. Ahmed Abdelgawad who joined the group the same year I did, work extremely hard and would always be eager to extend help whenever it was needed. He helped me build the electromagnets at the machine shop and worked with me on the 3D CAD designing of the electromagnet setup for CAFM. All the group members were very cheerful even through the strenuous times.

I am also grateful to have found a bunch of fun-loving and caring friends at CMU. I ended up sharing an apartment with some of them (which we named nineteen-hundred after the easy to remember street address), and the place turned out to be definite stress buster each day after work. We made lots of wonderful memories living here cooking, partying and watching movies. The place was home away from home and I am truly grateful to have found friends who have been there with me through all times. I wish them all the best in their career.

My parents who live in India were geographically the farthest yet remained closest to my heart. I am forever indebted to my mom and dad who chose a life of austerity to support me through my education and gave me a bright future. My parents would unfailingly call me every other day to talk to me and ensure my physical and emotional well-being. Being away from my grandparents was hard too; they take a lot of pride and joy seeing me work towards my PhD degree which kept me motivated. I wish I had more time to spend with them the last few years. My grandfather would always prod me to aim higher in education and to never fear failures. I wish to thank all my family members who cherished and celebrated all the success milestones I hit along the way.

Finally, I would like to thank my dear wife, Nancy. She accepted my long hours at work gracefully and with full-hearted support. She stood by me through the difficult times and has helped a great deal by taking burdens off my shoulders at home. All this while managing her own time and studies for her actuarial sciences exams. I wish her all the best in her career and hope to support her the same way she supports me. She makes me feel special and motivates me each day. I am lucky to have found her.

Mukund Bapna

April 16, 2018

Pittsburgh, Pennsylvania

Preface

Magnetic tunnel junctions (MTJs) are the fundamental building blocks for technology such as magnetic random access memory (MRAM) and hard disk drives (HDD). MTJs store information in form of magnetization direction of its recording layer with respect to its reference layer. The process through which magnetization reversal can be achieved is thus fundamental and of great interest for MRAM technology. Magnetization switching can be achieved for example using a magnetic field, spin-transfer torque or by spin-orbit torque. The first commercially available MRAM were based on switching the MTJs with magnetic fields. Due to architectural and energy concerns with field driven operations it was difficult to meet the demand of ever increasing computational needs. The discovery of spin transfer torque (STT) in 1996 led to a surge in research and development of STT based memory that later became a mainstream technology. MRAM based on STT technology were commercially available around 2006. However, the need of large current densities $\sim 10^6$ A/cm² to perform read and write operations resulted in significant heat dissipation for high bit densities and with bit sizes less than 50 nanometers. This still continues to impede the development of STT based MRAM technology for future computational needs. The MRAM technology is still evolving, and new phenomenology and materials are been extensively explored by industries, universities and research institutes across the globe.

In this thesis I present the experimental study of device level physics on patterned magnetic tunnel junctions that are less than 100 nm in size. In Chapter 1, I describe the technique of Conductive atomic force microscopy (C-AFM) which is central to the research presented in this thesis. C-AFM provides with a sharp conductive probe (~ 20 nm tip radius of curvature) that can allow for electrical measurements on nano-size devices that otherwise need complicated interconnects. The C-AFM accelerates research at prototype state by eliminating the need of hardwiring the nanoscale devices.

In Chapter 2, I discuss the basics of magnetic tunnel junctions and the physics of tunneling magneto-resistance which is used for read and write operations. I then discuss CoFeB-MgO based MTJs and its superior magnetic properties over other known materials that make it lucrative for technological applications. I also discuss niche for high and low thermal stability MTJs and present a brief overview of research progress in this area over the last decade.

In Chapter 4, I explore how magnetostatic effects between the different magnetic layers have an effect on magnetization switching from P to AP state and AP to P state through both experimental observations and through COMSOL simulations. I present a systematic theoretical investigation using COMSOL simulations of the stray field distributions and their typical strength arising from PMA materials of varying diameters and fixed thickness values that are typically used in actual devices.

In Chapter 5, I present fabrication and device testing of thermally robust sub-100 nm Mo/CoFeB/MgO tunnel junctions with perpendicular magnetic anisotropy. The samples were annealed at 400 °C before patterning to investigate if the magnetic properties are still maintained for integration with CMOS technology wherein the

back-end processes are usually running at such temperatures. I also investigate voltage effect on magnetic anisotropy and field assisted switching in Mo-in such pMTJ structures with diameters ranging from 25 to 100 nm.

Low thermal stability MTJ for stochastic computing are discussed in Chapter 6 and Chapter 7, where switching speed is controlled by STT in case of in-plane MTJs with low RA product, and with VCMA in case of pMTJs with high RA product. Low thermal stability MTJs are of increasing interest for stochastic computing applications where the fluctuations in TMR are random in nature and arise due to exchange of thermal energy with surroundings. The fluctuations are truly random in nature which makes it useful for applications such as random number generation and stochastic operation of multiplication of analog numbers.

In Chapter 8, I show a demonstration of spin-orbit torque (SOT) switching in a small 20 nm perpendicular magnetic tunnel junction (MTJ). The layer switched by SOT has extremely high thermal stability. Magnetic recording media and MRAM target a thermal stability parameter $\Delta = E_{\text{switch}}/k_B T$ of 60-80, and the devices studied here have $\Delta = 85$, more than double that of comparable diameter MTJs switched by spin transfer torque (STT). Here I demonstrate SOT is switching in devices with the characteristics needed for magnetic random access memory (MRAM). Many earlier approaches focused on in-plane magnetized materials where the SOT switching mechanism is similar to STT, and hence rendered no advantage with regards to energy consumption, relative to current technology. I will show that switching using SOT along with a small STT current requires a current density only 15% of that required for pure STT switch. This is expected to dramatically reduce the energy consumption per switch in the memory cell from $\sim \text{pJ}$ to $\sim \text{fJ}$.

In Chapter 9, I showcase how an electric field effect in $L1_0$ FePd based FePd/Ru/FePd synthetic antiferromagnetic structure can be used to change the

coupling of SAF to the free layer between Ferromagnetic and Antiferromagnetic. This E-field effect along with the VCMA effect can be used to toggle the magnetization of the free layer between parallel and anti-parallel configurations without an external magnetic field or a large current density. This simple and efficient switching mechanism may eliminate the main obstacle to the development of energy efficient nonvolatile memory and can provide an attractive pathway for future MRAM technology.

Parts of this thesis have been published in the following journal articles:

- [1] B. Parks, M. Bapna, J. Igbokwe, H. Almasi, W. Wang, S. A. Majetich, I. Julianne, H. Almasi, W. Weigang, and S. A. S. A. Majetich, AIP Adv. **8**, 55903 (2018).
- [2] M. Bapna and S. A. Majetich, Appl. Phys. Lett. **111**, 243107 (2017).
- [3] M. Bapna, S. K. Piotrowski, S. D. Oberdick, M. Li, C. L. Chien, and S. A. Majetich, Appl. Phys. Lett. **108**, 22406 (2016).
- [4] S. K. Piotrowski, M. Bapna, S. D. Oberdick, S. A. Majetich, M. Li, C. L. Chien, R. Ahmed, and R. H. Victora, Phys. Rev. B-Condensed Matter **94**, 14404 (2016).
- [5] L. Tryputen, K.-H. Tu, S. K. Piotrowski, M. Bapna, S. A. Majetich, C. Sun, P. M. Voyles, H. Almasi, W. Wang, P. Vargas, J. S. Tresback, and C. A. Ross, Nanotechnology **27**, 185302 (2016).
- [6] S. K. Piotrowski, M. Bapna, H. Almasi, W.-G. Wang, L. Tryputen, C. A. Ross, M. Li, C.-L. Chien, and S. A. Majetich, IEEE Trans. Magn. **51**, 4400504 (2015).

And presented in the following symposiums and conferences:

- Magnetism and Magnetic Materials conference (MMM) 2017, Pittsburgh PA, USA
- Magnetism and Magnetic Materials conference (MMM) 2016, New Orleans LA, USA
- Non Volatile Memory Technology Symposium (NVMTS) 2016, Pittsburgh PA, USA
- Joint MMM-Intermag conference 2016, San Diego CA, USA
- Center for Spintronics Annual Review Meeting 2016, Minneapolis MN, USA
- IEEE Magnetics Society summer school 2015, Minneapolis MN, USA

Table of Contents

DEDICATION	IV
ACKNOWLEDGMENTS.....	V
PREFACE.....	IX
LIST OF FIGURES	XIX
LIST OF TABLES.....	XXVII
CHAPTER 1 CONDUCTIVE ATOMIC FORCE MICROSCOPY TECHNIQUE.....	1
1.1 Introduction to Atomic Force Microscopy	1
1.2 Electrically Conductive Tips.....	4
1.3 Current Amplifiers	6
1.4 RHK C-AFM	8
1.5 Measurement methodology	9
CHAPTER 2 MAGNETIC TUNNEL JUNCTIONS	12
2.1 Typical MTJ Stack Design.....	12
2.2 Tunneling Magnetoresistance	13
2.3 Tunneling characteristics with MgO tunnel barrier	17
2.4 Effect of annealing in CoFeB-MgO based MTJs	19
2.5 Perpendicular Magnetic Anisotropy (PMA)	21
2.6 Voltage Control of Magnetic Anisotropy (VCMA)	22
2.7 Thermal stability factor	24
2.8 Niche for High and Low thermal stability MTJs	26
2.9 Notable developments so far	28
CHAPTER 3 MAGNETIZATION DYNAMICS.....	30
3.1 LLG equation	30
3.2 Spin Transfer Torque switching.....	32
3.3 Spin-Orbit Torque switching.....	36

3.4	Combining SOT with STT for switching	41
CHAPTER 4 MAGNETO-STATIC EFFECTS IN PATTERNED MTJS		43
4.1	Introduction	43
4.2	Sample Information.....	44
4.3	Measurement of telegraph signal using CAFM	44
4.4	Slope asymmetry.....	46
4.5	Calculation of H_{ms} using COMSOL.....	47
4.6	Effect of size on x and z component of H_{ms}	50
4.7	Effect of Magnetic dead layer	52
4.8	Conclusion	53
CHAPTER 5 THERMALLY ROBUST SUB 100 NM MO/COFEB/MGO TUNNEL JUNCTIONS WITH PERPENDICULAR MAGNETIC ANISOTROPY		54
5.1	Introduction	55
5.2	Experimental	57
5.3	Imaging post patterning	58
5.4	Variation in H_c , TMR and $H_{ms,z}$ with size.....	61
5.5	Thermal stability analysis of a 55 nm device	63
5.6	Field assisted unipolar switching	64
5.7	Scaling to 25 nm device size	66
5.8	Summary	68
CHAPTER 6 LOW THERMAL STABILITY PMTJS FOR STOCHASTIC COMPUTING.....		70
6.1	Introduction	71
6.2	Background: Effect of bias on lifetime	72
6.3	Sample preparation and experimental setup.....	73
6.4	MTJ Performance under multiplication operation using AND gate.....	79
6.5	MTJs as RNG – NIST STS Analysis	80
6.6	Conclusion	82
CHAPTER 7 ELECTRICAL CONTROL OF MAGNETIZATION VIA STT		83
7.1	Introduction	83
7.2	Patterning and experimental setup	85

7.3	Imaging and RH measurements of ellipses	86
7.4	Control over time averaged magnetization using STT	88
7.5	Performance as a <i>true</i> Random number generator	92
7.6	Performance in Logical AND Gate	93
7.7	Tuning telegraphing STT region with an external field	94
7.8	Summary and Future	95
CHAPTER 8 ELECTRICAL CONTROL OVER MAGNETIZATION VIA SPIN-ORBIT		
INTERACTION		97
8.1	Background	97
8.2	Sample information and nanofabrication of devices on Hall cross	99
8.3	C-AFM setup for SHE measurements.....	101
8.4	Size vs. H_c and TMR.....	103
8.5	SOT switching a 20 nm pMTJ	104
8.6	Estimation of field-free critical current densities and write energies	108
8.7	Summary	110
CHAPTER 9 ELECTRIC-FIELD CONTROLLED BIDIRECTIONAL MAGNETIZATION		
SWITCHING IN FEPD/TA/COFEB SAF		111
9.1	Introduction.....	112
9.2	VCMA and E-field control of FM-AFM coupling in SAF	112
9.3	Stack preparation: p-MTJ with FePd SAF	114
9.4	Nanofabrication and device testing setup.....	115
9.5	Variations with voltage bias and size.....	116
9.6	Bi-directional switching with voltage	120
9.7	Conclusion	122
APPENDIX A BUILDING IN-PLANE AND OUT-OF-PLANE ELECTROMAGNETS		123
APPENDIX B IMPROVEMENTS IN ION MILLING PROCEDURE		125
APPENDIX C SHAPE ANISOTROPY.....		127
APPENDIX D CHIP CARRIERS AND WIRE BONDING.....		130
APPENDIX E CURRENT SPREAD IN HALL CROSS- COMSOL SIMULATIONS		131
REFERENCES		132

List of Figures

Figure 1.1 LJ potential (equation 1.1). AFM is said to operate in contact mode when the force between the tip and the surface repulsive and in the non-contact mode when it is attractive.	4
Figure 1.2 SEM images of C-AFM tips (a) commercially available Arrow EFM tip with 20 nm Pt coating. Top view of used tips showing different failure modes: (b) wear of the conductive coating after multiple scans (c) debris on a 200 nm Pt tip.....	6
Figure 1.3 Schematic of a current gain amplifier typically used for current gain in C-AFM.....	6
Figure 1.4 (a) RHK CAFM scan head design (b) Sample holder with clamps that press on the sapphire washer and sample to hold the sample in place during the scan. Ti coated ramps are used to move the piezo legs of the Bettie for z motion.	9
Figure 1.5 SEM images of device layout (at different magnifications) written by electron beam lithography for easy location and electrical testing with C-AFM.10	
Figure 1.6 (a) topographic map (b) cross-section of topographic map along the line marked as 1 in (a). (c) Current map where the colors indicate the amount of current that was detected at each point during the topography scan when a voltage bias was applied between the sample and the tip.	11
Figure 2.1 Typical stack structure implemented for MRAM. The magnetization direction (black arrows) can be in the plane (as shown) or out of the plane (vertical in the schematic). In some cases, the SAF structure may not be needed if the reference layer is fixed and highly stable on its own. Different interactions between the magnetic layers are shown on the right.	13
Figure 2.2 (a) Rigid band model for transition metal ferromagnets (b) Schematic of metal insulator metal tunnel junction, the tunnel barrier of thickness t leads to a	

linearly decreasing voltage to the left and also shift the relative Fermi energy by eV for an electron passing through it.	14
Figure 2.3 (a) Wave function coupling between the Bloch states in Fe and evanescent states in the MgO tunnel barrier for $(k_z, k_{ }=0)$ direction. (b) Tunneling DOS of majority spins. Figure taken from [6].	18
Figure 2.4 (a) cross sectional TEM of CoFeB/MgO/CoFeB based MTJ. (b) Schematically shows the transformation of a-CoFeB to BCC CoFeB upon annealing at 250 °C. Figure taken from [10]	20
Figure 2.5 Effect of an Electric field on coercivity of top and bottom CoFeB layers. Figure taken from [14].	23
Figure 2.6 RV loop for a low thermal stability device. Lesser telegraphing is seen for negative bias where the free layer becomes stable and more telegraphing behavior is seen for positive bias which lowers the stability.....	25
Figure 2.7 Contour plot of temperature of a pMTJ for depending on the lifetime and the applied voltage bias.	28
Figure 3.1 LLG dynamics (Equation 3.1). The magnetization (m) precesses about the effective field direction (H_{eff}). The purple arrow illustrates the direction of dissipative (damping) torque that directs m towards the effective field direction. The spin-transfer torque acts opposite to the damping torque, and the red arrow shows the field-like torque for an electron with spin polarization parallel to the effective field.....	31
Figure 3.2 Different regions of telegraph noise based on external applied field H and applied voltage bias V (based on theoretical calculations). The solid and dotted lines designate AP-P and P-AP boundaries. Lines α and α' : a bias-independent zero-temperature H_k . Lines β and β' are the thermal-activation boundaries with spin-torque and finite temperature. Lines γ and γ' are the bias-dependent H_k . Lines δ and δ' are the thermal-activation boundaries with bias dependent H_k . The horizontal arrow shows a sweep of switching voltage from an AP-P	

switching to a crossing from P into the telegraph region, partially reverting to AP states, corresponding to the back hopping. Figure taken from Reference [38].	36
Figure 3.3 Direction of spin polarization of the accumulated spins at the surface in case of β -Ta and Pt (b) due to charge current J_c .	38
Figure 3.4 SOT in the case of (a) an in-plane easy axis with due to in-plane magnetic anisotropy (IMA) (b) an out-of-plane easy axis due to perpendicular magnetic anisotropy (PMA). In case of IMA the SOT competes directly with damping torque, whereas in the case of PMA, SOT may not compete directly with damping torque, depending on the azimuthal angle (in-plane).	39
Figure 3.5 Stable magnetization switching direction due to SOT for of a PMA material depends on the direction of the charge current flow in β -Ta and on the direction of external field B_{ext} .	40
Figure 3.6 STT can be used along with SOT to switch a pMTJ. (a) A contour plot of the switching probability for different combinations of J_c and J_{STT} . Figure adapted from Brink et al. 2014 [40](b) The perpendicular magnetization evolves in the presence of a STT current density of 1.5 MA/cm^2 and different values of J_{SHE} . Figure adapted from Wang et al. 2015 [41].	42
Figure 4.1 (a) TMR minor loop (solid line) for a 70 nm diameter MTJ, measured with a ramp rate of 345 Oe/s and bias of + 100 mV. At 140 Oe, the MTJ is stable in the AP state, and at 100 Oe it is stable in the P state. At fixed fields in between (dashed lines) it switches thermally as a function of time, as seen in (b). As the field is reduced, fluctuations to the P state appear at 131 Oe. By 113 Oe the MTJ is spending most of the time in the P state. Reprinted from [43].	46
Figure 4.2 (a) $\ln(\tau/\tau_0)$ versus H_{appl} , measured at 300 mV, showing data for the same 70 nm MTJ initialized with the hard layer magnetized downward (a) and upward (b). Reprinted from [43].	47
Figure 4.3 Snapshot of the geometry used in COMSOL simulation. The bottom disk acts as fixed PMA layer and stray field is calculated at the middle of disk on top	

which acts as a free layer. The disks are surrounded by air in the simulation marked by the spherical boundary as shown.....	48
Figure 4.4 (a) Height-averaged $H_{ms,z}$ at the soft layer, due to a hard layer magnetized downward, for an MTJ with diameter $d = 70$ nm. Solid arrows indicate the direction of $H_{ms,z}$. The dashed arrows indicate the direction of H_{appl} , which is spatially uniform. (b) $H_{eff,z}$ when $H_{appl} = 130$ Oe. For the range of H_{appl} where telegraphing occurs, $H_{eff,z}$ is positive in the center of the soft layer but negative near the edges. Reprinted from [43].	49
Figure 4.5 Vertical (a) and radial (b) components of \vec{H}_{ms} for MTJs of different diameters.	51
Figure 4.6 H_x and H_z components of the magnetic stray field with and without the 0.5 nm magnetic dead layer in.	53
Figure 5.1 (a) SEM image of multiple 25 nm MTJs. (b) Magnified SEM image of a single 25 nm device. (c) XTEM cross section of a 150 nm diameter feature (d) EDX elemental mapping on the bottom of the patterned structure (red box in (c)) showing tapering but no re-deposition. (e) AFM topography of devices showing uniform height, as can be seen in the line profile (f). Color maps showing current through devices in the P (g) and AP states (h).	60
Figure 5.2 (a) top layer coercivity vs size (b) TMR vs. size (c) Resistance vs. inverse of area of the MTJs (d) perpendicular component $H_{ms,z}$ of the stray field.....	62
Figure 5.3 RH loops for a 55 nm size device measured 100 times at bias voltage values of (a) -0.5 V and (b) +0.5 V. The VCMA effect causes H_c to change with bias, as can be seen from change in average loop widths between (a) and (b). (c) K_{eff} vs Bias, where a linear fit gives the value of the VCMA coefficient $\xi=19$ fJ/Vm. (d) Thermal stability factor variation with bias value. The dotted red line is a guide to the eye.....	64
Figure 5.4 Unipolar switching achieved using magnetic field and VCMA effect in a 55 nm pMTJ device.....	66

Figure 5.5 (a) minor RH loop for a 25 nm pMTJ device showing 138% TMR. The loop is shifted from the center due to stray field from the bottom reference layer. (b) RV loop showing switches on the positive and negative sides without stray field compensation.	68
Figure 6.1 VCMA effect causes the switching frequency to change upon application of a voltage by changing the energy barrier between P and AP states.....	73
Figure 6.2 (a)CAFM setup (b)SEM of 25 nm device (c) Digitized telegraph noise from 25 nm device showing two states.	74
Figure 6.3 (a) SEM image of the bond pads connecting to individual MTJ devices showing a zoomed in made of an individual hard wired device. Four leads connect to the electrode on top and four leads connect to the bottom of MTJ at the center of the cross as can be seen schematically in (b). (c) A chip carrier (CC) carrying a chip with 25 Hardwired devices, some of the devices are connected via the gold leads from bond pads to gold pads on the CC.	75
Figure 6.4 Minor RH loops (digitized): (a) A 60 nm CFB442 showing telegraphing, (b) 60 nm showing stable switches, (c) a 25 nm CFB262 showing telegraphing. The red curve in (a) and (c) is a sigmoidal fit to show tunability between P and AP with the field. Loops are shifted due to the stray field from the reference layer. Sweep rate ranged from 250-1500 mV/sec.	76
Figure 6.5 Lifetime of the high and low current states shows a non-linear trend for (a) 60 nm CFB442 and (b) 25 nm CFB 262.....	78
Figure 6.6 (a) Schematic of an AND gate which multiplies the probabilities of two Random Telegraph Noise input signals being in P state with probability= x . (b) percentage error which is small and decreases with increase in the input signal duration.....	80
Figure 7.1 Schematic of C-AFM setup used for electrical measurements of MTJs. The devices are patterned till the MgO, and the reference layer CoFe is coupled to	

CoFe/Ru/PtMn underneath in a synthetic antiferromagnetic arrangement. The numbers in brackets are thickness values in nm. Figure taken from [77].	85
Figure 7.2 (a) SEM images of patterned ellipses (b) AFM topography (c) current map at 100 mV bias voltage and (d) RH loops for ellipses with different orientation across rows and different sizes across columns (relative size and orientation shown in inset similar to (a)).	87
Figure 7.3 (a) The resistance vs. magnetic field loop taken at 10 mV bias voltage shows telegraphing between two states, which can also be observed as a function of time in (b). At $H_{\text{ext}} = 12.5$ Oe the external field cancels the dipolar field and the device telegraphs between the P and AP states (solid red curve) with equal lifetimes and the inset shows the number of counts vs. lifetimes in a semilog plot for the same trace. Figure taken from [77].	88
Figure 7.4 (a) R(V) loop for a 20 nm x 60 nm ellipse measured at $H_{\text{ext}} = 0$ showing telegraphing signal at positive bias. The red curve is guide to the eye for the telegraphing region. (b) Resistance vs. time traces measured at different bias values (c) average lifetimes in P and AP states and (d) time-averaged magnetization (circles) with the sigmoidal fit (blue curve) versus bias. Figure taken from [77].	90
Figure 7.5 Error minimization with time for multiplication of two number encoded as the probability of signal being in state $m=1$. Here two inputs come from two different MTJs operating at two different bias voltages, V_A and V_B . Figure taken from [77].	94
Figure 7.6 (a) Telegraph noise observed around 0.25 V when the external field H_{ext} and stray field H_s add up to a positive value and (b) at -0.25 when they add up to a negative value.	95
Figure 8.1 Side view and top view of the stack structure through the process flow for device and hall cross fabrication. Not to scale.	100
Figure 8.2 Optical and SEM images of the patterned Hall cross sample.	101

Figure 8.3 (a) Schematic of the experimental setup. A charge current pulse for SOT switching and detection of the MTJ resistance state using C-AFM. A sharp conductive tip with a ~ 20 nm radius of curvature provides a point contact on top of the MTJ. Tunnel magnetoresistance (TMR) is measured to detect the state of the device, parallel (P) or antiparallel (AP). The tip is retracted (along z) while a charge current pulse J_c (positive along x) passes underneath the MTJ. The spin current σ provides torque along y . A net external field $H_{\text{ext}}=100.7$ Oe, at an angle $\theta=87.5^\circ$ is kept constant during the current pulse. The tip is brought in contact after the pulse to re-measure the TMR. (b) Optical image of CAFM tip over the hall cross, markings show the electronic read and the write path.	102
Figure 8.4 Variation in the minor loop coercivity H_c and TMR for the <i>top</i> CoFeB layer for different size devices. H_c decreases below 50 nm but is still sizeable at 20 nm. The bottom layer H_c exceeded the maximum field of the in situ electromagnet (1300 Oe) for all sizes.	104
Figure 8.5 Four different combinations between the magnetization of the bottom layer and the charge current direction. Only two such combinations a SOT switch can be obtained. An external field assist was used to obtain a deterministic switch.	105
Figure 8.6 SEM image of a 20 nm device. Current maps measured using C-AFM of the device initially in the AP state (b), and after SOT switching to the P state (c). Minor loop resistance for the 20 nm MTJ at 10 mV bias, showing different loop shift directions before (d) and after (e) the current pulse. The top layer coercivity is 353 Oe, and the loop shift is 161 Oe.	106
Figure 9.1 (a) SEM image of the patterned devices of different sizes. Using CAFM (b) topography map and (c) current map measured at 100 mV was obtained. Very few devices below 60 nm survived the patterning process post Ion milling due to high aspect ratio during the step as can be seen through the topography and current maps.	116

Figure 9.2 Comparison of the coercivity change with the different applied bias voltages. The bias voltage (V_{bias}) can modify the magnetic anisotropy of interfacial perpendicular magnetic materials. Here we compare the coercivity (H_c) change between FePd SAF p-MTJs and CoFeB p-MTJs with the different applied V_{bias} . For FePd SAF p-MTJs, the H_c shows a steeper change with bias than for CoFeB/MgO/CoFeB pMTJs..... 118

Figure 9.3 (a) The minor M-H loops of 100-nm diameter FePd SAF p-MTJ devices with the different V_{bias} swapping H_{ext} from -1200 Oe to +1200 Oe. (b) The H_c vs. V_{bias} curve and (d) the $K_{u,\text{eff}}$ vs. V_{bias} for a 100-nm diameter FePd SAF p-MTJ device. Here the H_c (coercivity) and $K_{u,\text{eff}}$ (effective magnetic anisotropy) values are obtained by fitting the switching field distribution (SFD) with the Kurkijärvi-Fulton-Dunkelberger equation. The efficiency (ξ) of the voltage-controlled magnetic anisotropy (VCMA) for 100-nm diameter FePd p-SAF p-MTJ devices was obtained from the linear fit. (d) Effect of size on coercivity which is found to be increasing with decreasing size..... 119

Figure 9.4 E-field switching of p-MTJs. (A) The current vs. voltage (I-V) curve for a 100-nm diameter FePd SAF p-MTJ device measured by C-AFM without applying H_{ext} . The sharp magnetization switching was observed by applying a negative $V_{\text{bias}} \sim -0.46$ V ($I = -8.92$ μA) and a positive $V_{\text{bias}} \sim +0.48$ V ($I = +8.73$ μA), respectively, indicating the AP-P and P-AP states. (B) The current vs. time trace measured for the same device. The negative and positive 0.85 V voltage pulse was applied for a *write* operation, and a positive 0.1 V was used to *read* the current levels to check the device state (P or AP state)..... 121

List of Tables

Table 1.1 Different current amplifier their gain, bandwidth RMS noise and max current limits.	8
Table 4.1 Average in-plane and perpendicular magnetostatic fields at different locations of the soft layer	52
Table 6.1 The NIST STS tests for randomness were applied to the time-resolved resistance measurements with different degrees of whitening. Bold-faced p-values indicate a passed test.	82
Table 7.1 P-values for randomness for different NIST STS tests vs XOR operations performed on a telegraph signal generated by MTJ operating near the critical current I_c . Non-zero values (in green) show passed tests.	93

Chapter 1 Conductive Atomic Force Microscopy Technique

The technique of Conductive Atomic Force Microscopy (C-AFM) is central to the research presented in this thesis. C-AFM as a tool was indispensable for making electrical measurements on sub-micron size devices that I fabricated for my experimental investigations. In this chapter, I will describe the underlying principles of working of AFM and C-AFM.

1.1 Introduction to Atomic Force Microscopy

Atomic force microscopy (AFM) is a surface topography mapping technique, which utilizes a cantilever with a sharp probe to scan the specimen surface. The cantilever beam is attached at one end to a piezoelectric displacement actuator controlled by AFM. At the other end of the cantilever tip is a probe, which interacts with the surface. At near the surface, the probe experiences a force (attractive or repulsive) due to surface interactions, which introduces a bending moment on the cantilever. In response to this moment, the cantilever gets deviated from its normal position. This deviation is measured using a four quadrant photodiode and laser beam reflected from the coated surface of the cantilever. The change in beam deflection on quadrant photodiode is used to generate the feedback signal.

The force most commonly associated with the scanning force microscopy is the inter-atomic van der Waals force. The dependence of the van der Waals force upon the distance between tip and sample is described by Lennard-Jones potential:

$$\varphi(z) = Az^{-12} - Bz^{-6}. \quad 1.1$$

As the tip approaches the surface, attractive forces (e.g., the van der Waals force) act between the tip and sample before repulsive forces due to the overlap of electron orbitals (e.g. Pauli repulsion) start to dominate. The force between the tip and the sample surface can then be found using $F = -\partial\varphi/\partial z$. The different regions of attractive and repulsive regimes are shown in Figure 1.1.

In an AFM, the tip is attached to a flexible cantilever (for example see Figure 1.2(a)), which is subject to Hooke's law:

$$U_{cantilever}(z) = k \frac{(z - z_0)^2}{2} \quad 1.2$$

where k is the spring constant of the cantilever and z_0 is the tip-sample distance for an unbent cantilever. The tip is mounted on a piezo stage which consists of separate electrodes to scan precisely the sample in the x - y plane in a raster pattern and to move the tip holder assembly in the vertical (z) direction. A sharp tip at the free end of a flexible cantilever is brought in contact with the sample. Features on the sample surface cause the cantilever to deflect in the vertical and lateral directions as the sample moves under the tip. A laser beam from a diode gets directed onto the back of a cantilever near its free end. The reflected beam from the vertex of the cantilever is directed onto a split photo-detector with four quadrants. The differential signal from the top and bottom photodiodes provide the AFM signal which is a sensitive

measure of the cantilever vertical deflection. Topographic features of the sample would cause the tip to deflect in the vertical direction as the tip scans the sample. This tip deflection changes the direction of the reflected laser beam, changing the intensity difference between the top and bottom sets of photodetectors (AFM signal). To measure topographic features of the sample surface, the distance between tip and sample is kept constant, and a feedback circuit is used to modulate the voltage applied to the piezo scanner to adjust the height of the piezo stage, so that the cantilever vertical deflection (given by the intensity difference between the top and bottom detector) will remain constant during scanning. The piezo scan head height variation is thus a direct measure of the surface roughness of the sample.

During imaging, an AFM can be set to obtain an image in contact mode or noncontact mode. In contact mode, the tip raster scans the surface in the repulsive regime. The feedback parameter in this mode is the bending of the cantilever, which ensures a constant force between the tip and sample. The up and down deflections are recorded as topography. This is a preferred mode for features on the sample that strongly adhere to the substrate. For particles that are either soft or weakly bound to the substrate noncontact contact or tapping mode is preferred in this mode cantilever is oscillated at its resonance frequency with a free amplitude A_0 . While the cantilever is approaching the surface, the oscillating amplitude is damped to a value A , which depends on the distance to the surface. The ratio $r = A/A_0$ defines the damping of the amplitude while the tip is in contact with the surface and is proportional to the applied force. By keeping the damping of the amplitude constant, the surface topography can be imaged. The interaction between the tip and the sample surface is predominantly vertical. Consequently, noncontact mode AFM does not suffer from the tip or sample degradation effects that are frequently observed in contact mode AFM.

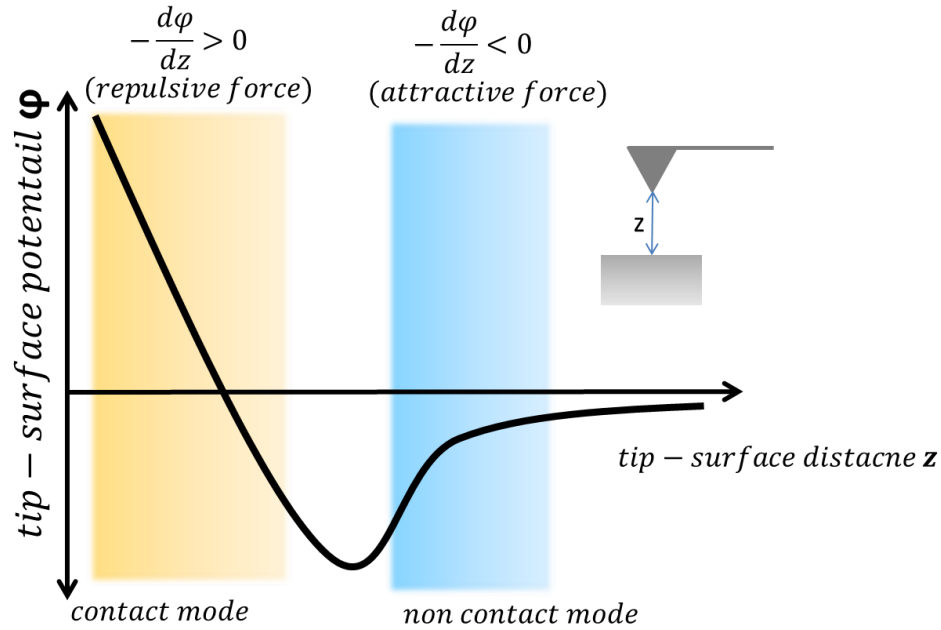


Figure 1.1 LJ potential (equation 1.1). AFM is said to operate in contact mode when the force between the tip and the surface repulsive and in the non-contact mode when it is attractive.

1.2 Electrically Conductive Tips

The tips used in C-AFM are usually Si-based tip with conductive Pt coating of varying thickness depending on the target application. For small device sizes where the lateral resolution of less than or equal to 20 nm is needed, tips with a 20 nm Pt coating and a tip radius of curvature less than 25 nm are used. For experiments where high current densities are needed such as STT, experiments where typically current densities of the order of 10^6 A/cm^2 are used, 200 nm coated Pt tips work best without the problem of the tip wearing out. With each scan, the tip wears out part of its conductive coating. If the sample surface is not clean the tip can pick up debris from the surface and could result in loss of conductivity. Figure 1.2 shows

SEM image of an AFM tip (a) as prepared by the manufacturer and (b) after about 20 scans. In some experiments, commercially available Si tips were coated with 10 nm Ti followed by 200 nm Pt thin film by DC sputtering to increase the life of the tip against wear due to contact mode scanning, and to allow for high current densities to flow through the tip without damaging it. The increased coating thickness compared to commercial conductive probes combined with the larger contact area due to larger tip radius of curvature allows for high currents ~ 10 mA before the coating melts or deforms significantly. The Pt deposition process flow on AFM tips was originally developed by Eric Evarts, a former student in the group and more details about the deposition can be found in his Ph.D. thesis. While the 200 nm Pt-coated tips are highly wear resistant, however they are still prone to failure due to any nonconductive contamination that could stick on the tip from the sample surface. Since most of the measurements are done in ambient atmospheric conditions, extreme care must be taken to clean the sample surface using acetone and isopropyl alcohol to remove as many contaminants from the sample surface as possible through rinsing and ultrasonication.

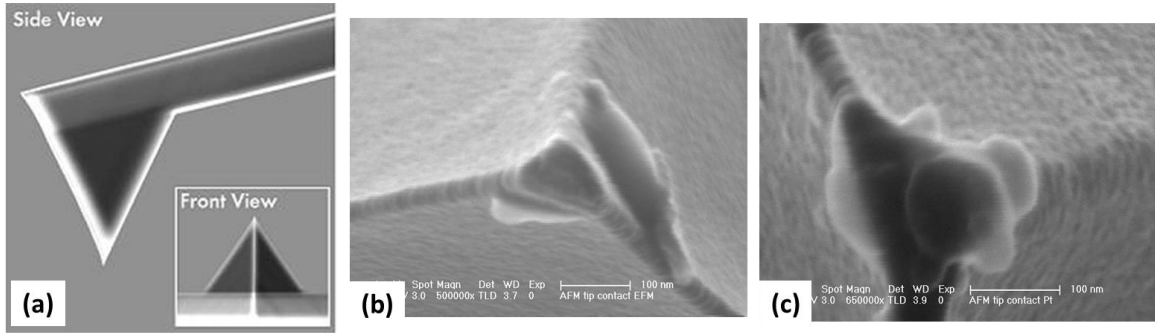


Figure 1.2 SEM images of C-AFM tips (a) commercially available Arrow EFM tip with 20 nm Pt coating. Top view of used tips showing different failure modes: (b) wear of the conductive coating after multiple scans (c) debris on a 200 nm Pt tip.

1.3 Current Amplifiers

Amplifiers are needed to read small current signals that otherwise may not be detectable. The current amplifiers used here are basically Operational Amplifiers (Op-Amps) which convert a current signal to a readable voltage signal due to amplification. A schematic of an Op-amp is shown in Figure 1.3.

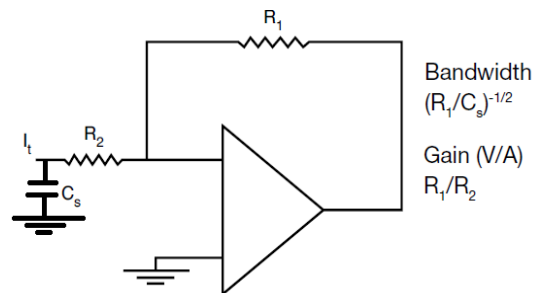


Figure 1.3 Schematic of a current gain amplifier typically used for current gain in C-AFM

The gain of an amplifier characterizes the amplification and typically has units of voltage per unit current. The gain is determined by the ratio of R_1 and R_2 ,

and the bandwidth is determined by the product of R_1 and the unavoidable stray capacitance of the tip along with the wire that carries the tunneling current from the tip to the input of the amplifier. As this capacitance is decreased, the bandwidth would increase for a fixed gain. The bandwidth (BW) is related to the rise time (RT) by the empirical relation $BW \text{ (GHz)} = 0.35/RT(\text{ns})$. With the present RHK scan head design, we typically get a 400 ns rise time. This value was confirmed by pulsing a voltage pulse through a fast pulse generator and reading the output through an oscilloscope. For measurements where faster rise times are needed the devices were hardwired (see Chapter 6), which allows for connection to a faster set of electronics (pulse generators, amplifiers and oscilloscopes). Different types of commercially available current gain amplifiers were used in the different C-AFM measurements that are presented in this thesis. The different amplifiers that I used with their current compliance, RMS noise, bandwidth and gain values are tabulated in Table 1.1. When testing a device an amplifier is chosen such that the gain value allows for readout of the maximum current value that may appear during device testing and at the same time maintaining low signal to noise ratio to see desired features in the output current signal. As discussed above, the gain and bandwidth are dependent on the resistors and capacitors that are used in the circuit. In some case cases custom preamps are available (from Femto Electronics) where jump resistors can be used which provides the convenience of switching between the different values of gain and bandwidth easily during measurements without the need to disconnect the electronics.

Table 1.1 Different current amplifier their gain, bandwidth RMS noise and max current limits.

	Gain	Bandwidth	RMS noise	Max current limit
IVP 400	10^3	10 MHz	1 nA	1 mA
IVP 300	10^9	5 kHz	0.3 pA	10 nA
IVP 200	10^8	30 kHz	1 pA	100 nA
IVP 100	10^7	250 kHz	2 pA	1 μ A

1.4 RHK C-AFM

The instrument used in the all the transport studies reported in this thesis is a UHV300 C-AFM with R9 controller electronics from RHK technologies. The instrument was first commissioned around 2005 at the time of a former Ph.D. student Eric Evarts who used the instrument to study spin-transfer torque switching in small magnetic tunnel junctions [1]. The instrument was later used by another former Ph.D. student Stephan Piotrowski for his research work. Technical support was provided by Kenneth Collin from RHK for all the upgrades and troubleshooting related to the C-AFM.

The RHK CAFM scan head is shown in **Figure 1.4**. The scan head sits in an inverted vertical column arrangement. To start the approach procedure, the scan head is initially lowered towards the sample through a mechanical rotation of a screw head on top. After the beetle legs land on the sample holder, a coarse approach using controls from R9 software can be performed to bring the tip in proximity $< 100 \mu\text{m}$, after which the automated fine approach procedure is used to bring the tip in contact with the sample.

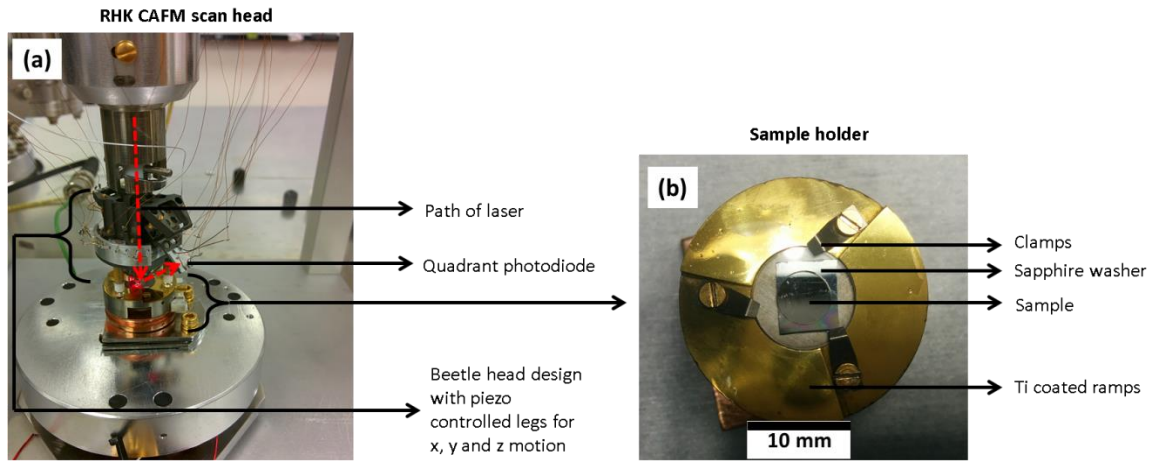


Figure 1.4 (a) RHK CAFM scan head design (b) Sample holder with clamps that press on the sapphire washer and sample to hold the sample in place during the scan. Ti coated ramps are used to move the piezo legs of the Beetle for z motion.

1.5 Measurement methodology

In all the measurements the sample remains stationary and the x, y and z motion of the tip relative to the sample is achieved through the piezo motors attached to the legs which move the beetle head. The legs of the beetle rotate clockwise or counterclockwise through a coordinated movement on the Ti ramps for the z motion. The instrument has a low drift rate of <1 nm/min. This drift rate can significantly increase due to factors ambient noise or temperature fluctuations. The sample is held in place in the sample holder using a set of washers above and below. The sapphire washer is used to electrically insulate the sample (on top or bottom) from the sample holder, and metal washers are used when a conductive contact is needed. For samples which are grown on insulating substrates (such as MgO) a metal washer needs to be used on top, and the sample should have a metallic seed

layer below the device and extend through the top surface of the sample towards the edge(s) to allow for a conduction channel. The sample size that can fit in the sample holder is limited by the outer diameter of the washer which is 11 mm. I typically cleave the samples with edge lengths between 5-7 mm for C-AFM. The area of interest for CAFM measurements with e-beam written devices on the sample surface is usually within $500\text{ }\mu\text{m} \times 500\text{ }\mu\text{m}$ area, hence the sample is centered such that this region roughly lies at the center where the tip would likely land.

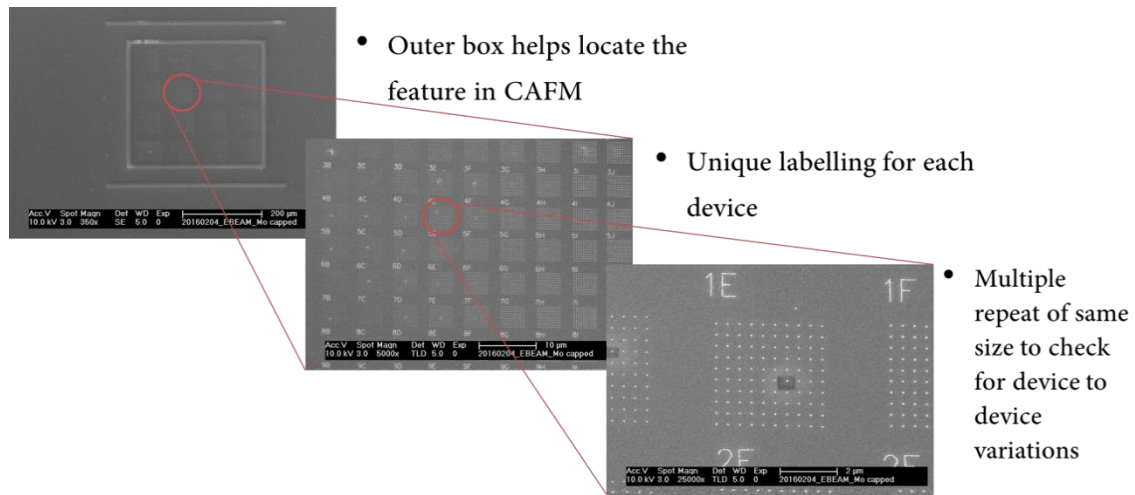


Figure 1.5 SEM images of device layout (at different magnifications) written by electron beam lithography for easy location and electrical testing with C-AFM.

A CCD camera with high zoom in capability is used identify the location of the e-beam patterned region and land the tip in the area. The e-beam written region imaged at different length scales is shown in Figure 1.5. The outer box with an edge thickness of about $10\text{ }\mu\text{m}$ is written such that it is visible with the CCD camera (also with a microscope with 10x magnification). Inside the box are multiple repeats of devices that are grouped in arrays of 10×10 devices and each array is uniquely labeled with a digit followed by a letter. The unique labels can be easily read during

imaging in conductive or non-conductive modes and help locate the same device during different measurement attempts. Since the maximum scan size is limited to $6\ \mu\text{m} \times 6\ \mu\text{m}$, having multiple repeats of devices with the relatively small device to device distances $\sim 200\ \text{nm}$ increases the likelihood of landing on an area and finding a device as good as finding it in other areas. Figure 1.6 shows a topographic map, line profile and current map of devices imaged with CAFM.

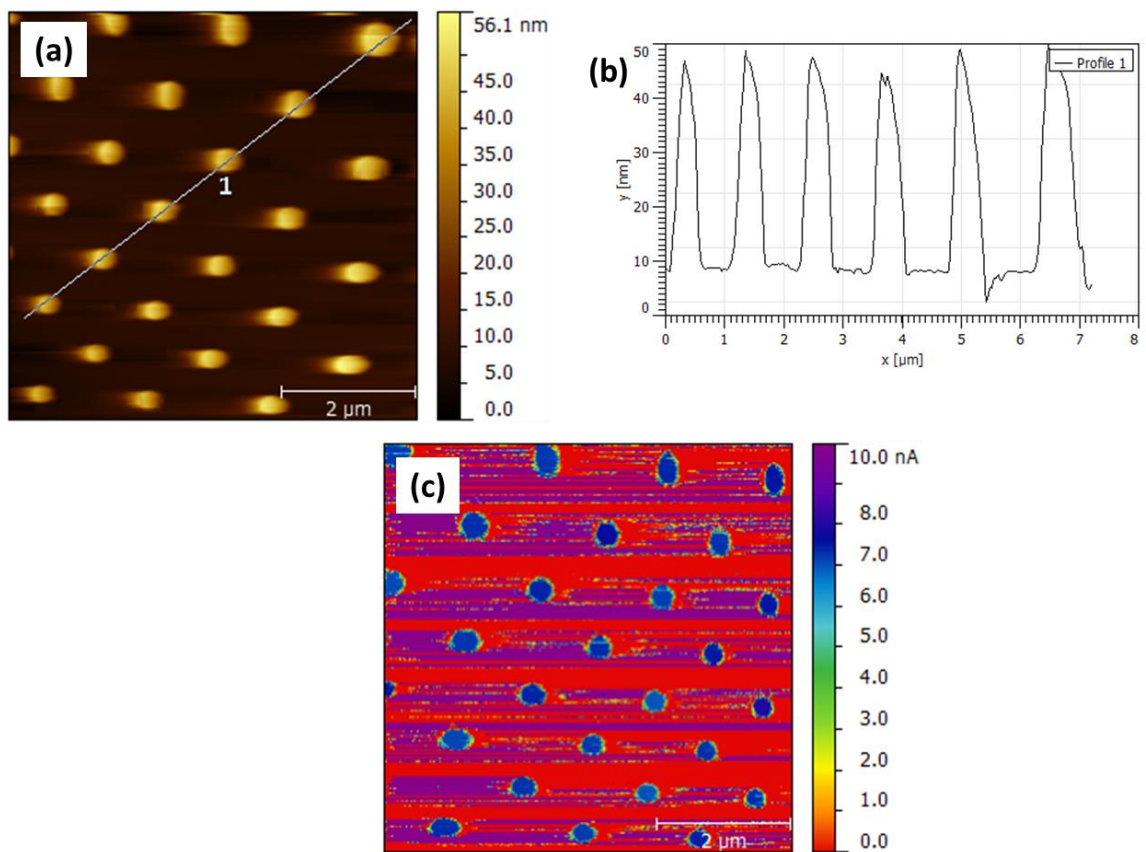


Figure 1.6 (a) topographic map (b) cross-section of topographic map along the line marked as 1 in (a). (c) Current map where the colors indicate the amount of current that was detected at each point during the topography scan when a voltage bias was applied between the sample and the tip.

Chapter 2 Magnetic Tunnel Junctions

Magnetic tunnel junctions (MTJs) typically consists of an ultrathin insulating layer, which acts as a tunnel barrier, sandwiched between two conducting ferromagnetic electrode layers, and exhibit magnetoresistance at room temperature. This phenomenon, known as the tunneling magnetoresistance (TMR) effect, has been studied extensively in attempts to develop magnetic random-access memory (MRAM) and read heads for magnetic sensors for hard disk drives.

In this Chapter, I go through the stack design, physics of tunneling magnetoresistance, parameters that are typically used to characterize MTJs, recent developments and its applications.

2.1 Typical MTJ Stack Design

A magnetic tunnel junction (MTJ) consists of an ultrathin insulating layer (tunnel barrier) sandwiched between two ferromagnetic (FM) metal layers (electrodes). A generalized layer stacking structure of MTJ for MRAM and related applications is shown in Figure 2.1. In an MTJ, the magnetization switching of one of the ferromagnetic electrodes can be achieved by an external magnetic field or a spin current passed through the MTJ. This layer is termed as the “free layer” or “recording layer”. The free layer typically has some uniaxial magnetic anisotropy due to its shape magnetic anisotropy or magneto-crystalline anisotropy, which should direct the magnetization along a certain axis or the easy axis. It is due to this uniaxial magnetic anisotropy that the free layer magnetization will rest in one of the two directions set by the easy axis. In this way, the free layer can store one bit of information in the form of the magnetization direction. The

orientation of the magnetization of the other ferromagnetic electrode is fixed and is termed “fixed layer” or “reference layer.” The fixed layer acts as a reference for the “read” and “write” operations.

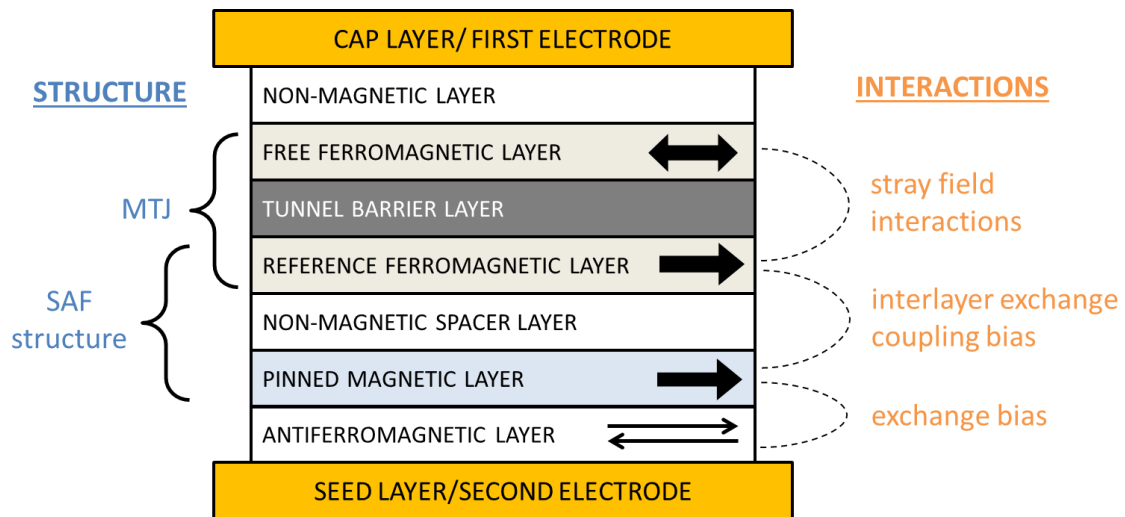


Figure 2.1 Typical stack structure implemented for MRAM. The magnetization direction (black arrows) can be in the plane (as shown) or out of the plane (vertical in the schematic). In some cases, the SAF structure may not be needed if the reference layer is fixed and highly stable on its own. Different interactions between the magnetic layers are shown on the right.

The fundamental property that allows for the read and writes operation to be performed in MTJs is the property of Tunnel Magnetoresistance (TMR). In the next section, I go through the basic theory of TMR that was first developed in the 1970s that led to the proliferation of research and development of MTJs for practical applications.

2.2 Tunneling Magnetoresistance

In the seminal work by Julliere in 1975, a model for tunneling in ferromagnet-insulator-ferromagnet junctions was proposed [2]. Two basic

assumptions were made. The first concerned spin conservation; tunneling is only possible between bands of same spin orientation in either ferromagnetic layer, i.e from an up spin to up spin band or from a down spin to down spin band. The second key assumption, was that the tunneling probability is independent of spin or magnetization orientation, that is, the spin reservoirs on either electrode are coupled in the same way for a given spin orientation. The role of spin can be understood by understanding the electronic structure of transition metal ferromagnet. A simple model of transition metal ferromagnetism is the rigid band model Figure 2.2(a), where the bands in transition metal ferromagnets comprising of the 4s and 3d atomic orbitals are considered. The 3d bands are more localized than the 4s bands, and they are exchange split. If Fermi level is in the 3d bands, then it leads to a net magnetic moment.

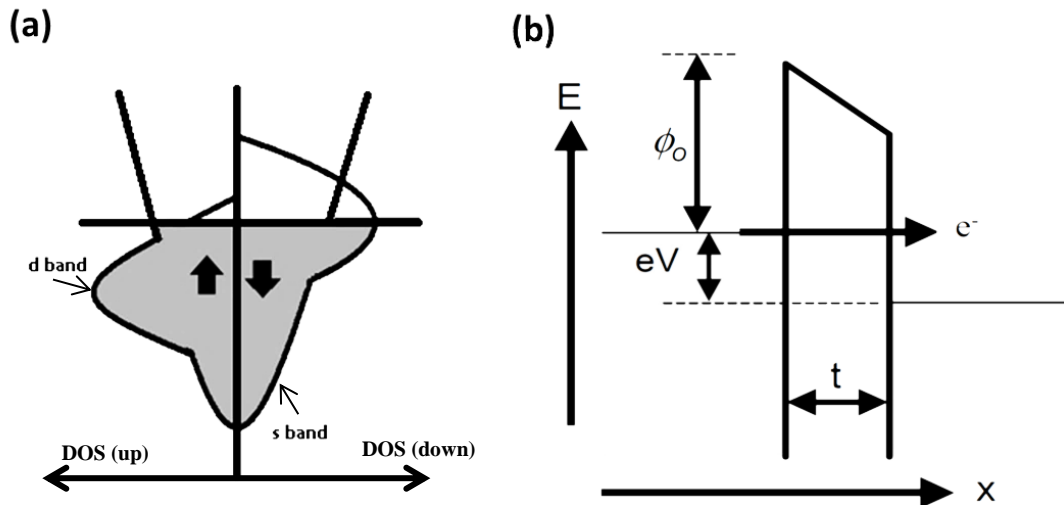


Figure 2.2 (a) Rigid band model for transition metal ferromagnets (b) Schematic of metal insulator metal tunnel junction, the tunnel barrier of thickness t leads to a linearly decreasing voltage to the left and also shift the relative Fermi energy by eV for an electron passing through it.

Julliere discovered the dependence of resistance of magnetic tunnel junction depends on the relative orientation of the FM layers. This is a direct consequence of having a spin-dependent density of states, using a Wentzel Kramers Brillouin(WKB) approximation we can see that how this comes into play [3]. Consider electron current through a potential barrier as shown in Figure 2.2(b). When the voltage across the junction is zero, the two metals electrodes will equilibrate, and the Fermi levels will be at the same energy for the two. When a bias V is applied, the two Fermi levels will differ by eV relative to the other, where e is charge of an electron. The number of electrons tunneling from left to right is then given by the product of the density of states at energy E in the left electrode multiplied by the density of states in the right electrode at the same energy level, multiplied by the transmission probability $|M|^2$. We must also then multiply this quantity by the occupancy probability defined by the Fermi distribution $f(E)$ for the left electrode and the vacancy probability, $1-f(E+eV)$, in the right electrode. The tunnel current from left to right is then:

$$I_{L \rightarrow R}(V) \propto \int dE [f(E)\rho_L(E)|M|^2(1 - f(E + eV))\rho_R(E + eV)], \quad 2.1$$

where the subscript L(R) refers to the left(right) electrode. We can then define the total current through the tunnel junction $I = I_{L \rightarrow R} - I_{R \rightarrow L}$. Since the Fermi level cuts across exchange split bands, this leads to a net imbalance in the spin population at energies corresponding to tunneling, that is $\rho_{\uparrow}(E) \neq \rho_{\downarrow}(E)$ where ρ_{\uparrow} and ρ_{\downarrow} are the density of states of the majority and the minority spins. When the magnetization of the electrodes are aligned parallel, the tunneling probability in equation 2.1 depends instead on the product of $\rho_{\uparrow, \downarrow}$ and $\rho_{\uparrow, \downarrow}$ whereas if they are anti-parallel it depends on the product of $\rho_{\uparrow, \downarrow}$ and $\rho_{\downarrow, \uparrow}$. This means that for a given value of bias, the two different magnetic configurations (parallel or antiparallel) allow for two

different current values (high or low), hence the ratio V/I is interpreted as the resistance also differs. Furthermore, the tunnel current-voltage $I(V)$ characteristics for moderate voltage values can be reasonably fit to the following expression: $I(V) = \alpha V + \beta V^3$, where α and β are fitting parameters that relate to the tunneling parameters as described above [4]. A more exact but still approximate form that is useful for fitting $I(V)$ curves was derived by Simmons [4] and can be used to extract tunneling parameters such as M , ϕ_0 , and t from data.

Since spin is a conserved quantity in the absence of spin scattering, a characteristic quantity called polarization can be defined as

$$P = \frac{\rho_{\uparrow} - \rho_{\downarrow}}{\rho_{\uparrow} + \rho_{\downarrow}}. \quad 2.2$$

Julliere further introduced a simple expression to relate polarization of the layers with the resistance change, for parallel and anti-parallel alignment of the layers, normalized by the low resistance value:

$$TMR = (R_{ap} - R_p)/R_p = 2P_1P_2/(1 + P_1P_2). \quad 2.3$$

Here R_p is low resistance corresponding to a parallel state, R_{ap} is high resistance corresponding to anti-parallel state and P_1 and P_2 defines polarization of first and second layer respectively. This expression is called the Julliere formula and it provides a simple qualitative interpretation of TMR values in MTJs. This expression, however, omits contributions from the tunnel barrier and the interfaces which could affect the TMR. For example, surface roughness in the ferromagnetic layer can lead to dipolar coupling between the bottom and top FM electrodes preventing independent switching of the magnetization. Second, depositing a thin insulating tunnel barrier over the bottom layer becomes difficult if the bottom layer is rough.

For instance, if we choose MgO as the insulating layer it must be about 8-20 Å and yet should be atomically smooth to observe tunneling effects with high TMR. Also, the presence of domain walls can cause coupling of the magnetization, leading to a reduced magnetic response of junction [5]. Other effects that can lead to deviation from the expected value could be direct coupling between the two FM layer and surface degradation of films.

Higher magnetoresistance ensures higher signal which is necessary for easy and reliable detection of the binary high and low resistance states for storing the data. In the next section, we see how MgO-based MTJs offer the possibility to effectively obtain high TMR based on symmetry preserving tunneling of electron waves through the MgO barrier.

2.3 Tunneling characteristics with MgO tunnel barrier

Crystalline MgO with 001 texture can be epitaxially grown on a bcc Fe(001) layer to obtain an MTJ with crystalline Fe(001)/MgO(001)/Fe(001). Considering the $(k_z, k_{||}=0)$ direction, three kinds of evanescent tunneling states can be present in crystalline MgO: Δ_1 , Δ_2 , and Δ_5 . To conserve orbital momentum as the electrons tunnel through the barrier, electrons tunnel coherently such that the electrons wave functions in the FM layer couple with evanescent wave functions having the same symmetry in the barrier. Theoretically, it is predicted that the tunneling probability depends strongly on the orbital symmetries of the Bloch waves, leading to symmetry filtering of the tunneling current [6]. Figure 2.3 (a) shows the rules of orbital selection for the tunnel conductance in Fe(001)/MgO/Fe(001) systems for electron flowing along the $(k_z, k_{||}=0)$ direction.

Figure 2.2(b) shows the partial DOS (obtained by ab-initio calculations) of the three different evanescent states in the MgO tunnel layer for the case of parallel alignment of magnetic moments. Among these three states, the Δ_1 evanescent states decay slowest (with the longest decay length). Hence the dominant tunneling channel for the parallel magnetic state is the Fe- Δ_1 /MgO- Δ_1 /Fe- Δ_1 channel.

Band structure calculations can be used to obtain the polarization and density of states corresponding to the three symmetry states mentioned above. For Fe, the energy splitting between the up and down spin Bloch states, $\Delta_{i\downarrow}$ and $\Delta_{i\uparrow}$ (for $i=1, 3, 5$), respectively, is such that only the majority spins fill the Δ_1 symmetry, hence giving a high polarization. Figure 2.3 presents the probability for incoming majority electrons to tunnel through. For the thickness of MgO of about nine monolayers, which is a reasonable barrier thickness (~ 2 nm) in MTJs, the transmitted density of Δ_1 states is larger than that of Δ_5 states by five orders of magnitude. Additionally, since there is no minority Δ_1 state to tunnel from or to, only the $\Delta_{1\uparrow} \leftrightarrow \Delta_{1\uparrow}$ channel contributes to the conduction. Similarly, for the AP configuration, $\Delta_{1\downarrow} \leftrightarrow \Delta_{1\uparrow}$ and $\Delta_{1\uparrow} \leftrightarrow \Delta_{1\downarrow}$ channels theoretically have zero tunneling probability.

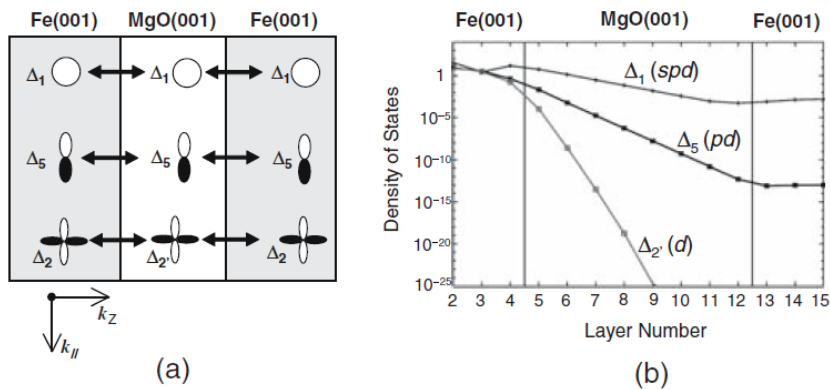


Figure 2.3 (a) Wave function coupling between the Bloch states in Fe and evanescent states in the MgO tunnel barrier for $(k_z, k_{||}=0)$ direction. (b) Tunneling DOS of majority spins. Figure taken from [6].

There is, therefore, an interesting mechanism of spin filtering of the wave functions due to their symmetry, which results in a dramatic increase in the net spin polarization of the tunneling current. Therefore significant conduction difference can be seen for P and AP configurations. It is due to this spin filtering effect that yields very large TMR which is predicted and have been actually measured in textured MgO-based MTJs. So far, MTJs with MgO give the best results regarding TMR.

Soon after 1000% TMR was theoretically predicted in MTJs with the crystalline Fe/MgO/Fe structure by preferential tunneling of Δ_1 symmetry states, TMR ratios ranging from 80% to 355% at room temperature were experimentally demonstrated for fully [100] oriented epitaxial Fe/MgO/Fe MTJs and sputter-deposited highly [100] oriented CoFeB/MgO/CoFeB MTJs. A key step in obtaining a high MR ratio particularly in CoFeB-MgO based MTJs is annealing which helps obtain epitaxial crystallinity of CoFeB over MgO thus allowing for the tunneling process with high selectivity for Δ_1 symmetry states and thus a high TMR, as discussed above.

2.4 Effect of annealing in CoFeB-MgO based MTJs

While huge TMR values $> 100\%$ were reported in some of the early works using fully epitaxial MTJs [7–9], from an application viewpoint, the bottom ferromagnetic electrode would need to be grown on on Pt-Mn or Ir-Mn exchange-biasing layer via Ru-based synthetic ferromagnetic structure. These bottom pinned-layer structures usually have fcc[111] texture, and so bcc FeCo[001] layers cannot be grown on the fcc[111] layers epitaxially. This problem was solved by Ikeda et al. [10] using

amorphous CoFeB bottom electrode layer, where MgO[001] can readily be grown on the amorphous CoFeB layer by simple RF sputtering. Top amorphous CoFeB layer was then grown on the crystalline MgO, and after post-annealing the MTJs at 360 °C, MR ratios above 200% at room temperature was observed. It is interesting to note that while the most stable structure of CoFeB is fcc, the CoFeB layers that lay adjacent to MgO[001] layer crystallizes into bcc structure upon annealing. This indicates that the process of crystallization is solid-phase epitaxy as a result of the good lattice matching between bcc CoFeB[001] and MgO[001].

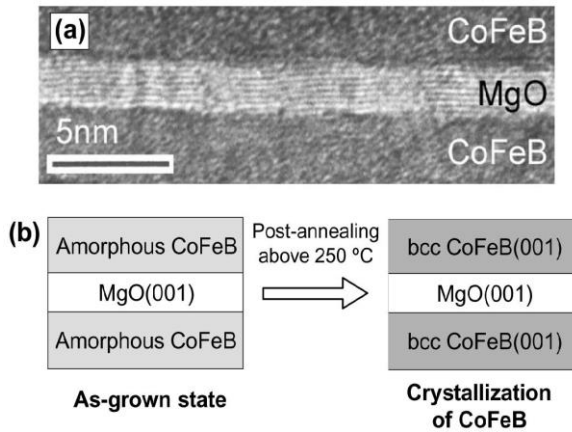


Figure 2.4 (a) cross sectional TEM of CoFeB/MgO/CoFeB based MTJ. (b) Schematically shows the transformation of a-CoFeB to BCC CoFeB upon annealing at 250 °C. Figure taken from [10]

Since the deposition method is highly compatible with manufacturing, this process of making MTJs with CoFeB/MgO interfaces have been used for research and development for many practical devices. CoFeB-MgO based MTJs has become irreplaceable in TMR read-write heads, conventional MRAM and spin-transfer torque MRAM (see section 3.2). The switching currents in case of MRAM with in-plane MTJs were very high, typically in 10^7 - 10^8 A/cm² range due to the relatively low degree of spin polarization in such metallic structures using spin transfer torque (STT). As the development of perpendicular MTJs progressed, a natural idea was to use STT method as a write mechanism. The first demonstration of STT switching in MgO-based MTJs was

made by Diao et al. [11] in 2005. Due to enhancement in polarization, the switching currents were reduced to about $\sim 10^6$ A/cm². Since then, much effort has been made in this field to reduce the current density requirements further by through improvements in fabrication tools, introduction of additional spacer layers like Ta, Mo, Hf and W in the stack, and through use of effects such as spin-orbit torque and electric field control of perpendicular magnetic anisotropy. Developed rapidly in the last decade or so, such devices which utilize CoFeB-MgO based perpendicular magnetic tunnel junctions (pMTJs) have already become mainstream and are in significant commercial use.

2.5 Perpendicular Magnetic Anisotropy (PMA)

The process of annealing has an important consequence in that it makes the magnetization point perpendicular to the plane due to induction of interfacial magnetic anisotropy. Particularly, the hybridization of Fe 3d_{z2} and O 2p_z orbitals for minority spins leads to perpendicular anisotropy, where an electric field can be used to change electron density near interface and hence K_{eff} . Regardless of the mechanisms causing the strong interfacial PMA, a phenomenological description is that an interfacial anisotropy overcomes the demagnetization field and increases the PMA as the thickness of CoFeB decreases. In Ta/CoFeB/MgO thin films, the uniaxial anisotropy will have contributions from the bulk and interface. Therefore, the effective anisotropy K_{eff} is a combination of bulk crystalline K_b , shape anisotropy K_s , and interfacial anisotropy K_i with the following relation:

$$K_{eff} = K_u + \frac{K_i}{t} + K_s, \quad 2.4$$

where t is the thickness of the ferromagnetic layer. By tuning the thickness of the ferromagnetic layer, different magnitudes of uniaxial anisotropy can be obtained,

and if the demagnetization energy or the shape anisotropy is overcome by the interface anisotropy, we get layers with perpendicular magnetization. In Equation 2.4, the value of K_u and K_s are taken as negative values and the anisotropy K_i term is taken as positive. We can now see that the system has perpendicular magnetic anisotropy if the values of $K_{eff} \cdot t$ is positive, whereas the system has in-plane anisotropy for negative values. Thus, the critical CoFeB layer thickness t where the in-plane anisotropy turns into perpendicular magnetic anisotropy can be obtained from $K_{eff} \cdot t = 0$.

2.6 Voltage Control of Magnetic Anisotropy (VCMA)

Many theoretical and experimental works have shown that the perpendicular magnetic anisotropy energy (MAE) in ferromagnetic layers can be modulated by an electric field, which can significantly reduce the energy required for switching the magnetization of the free layer as opposed to using only an external magnetic field for switching. Through first principle calculations, Niranjana et al. [12] investigated the effect of an external electric field on the magnetization due to the Fe/MgO(001) interface. The calculations show that the spin density and the magnetic moment of Fe atoms at the interface of Fe/MgO strongly depend on the strength of the electric field at the MgO. Upon application of an electric field interfacial magnetic anisotropy energy changes significantly due to the changes in relative occupancy of the 3d-orbitals of Fe atoms at the Fe/MgO interface. Furthermore, in work by Maruyama et al. [13], it was shown that a relatively small electric field (less than 0.1 V/nm) could cause a large change of about ~40% in the magnetic anisotropy of a bcc Fe(001)/MgO(001) junction. The effect was attributed to the change in the relative occupation of 3d orbitals of Fe atoms adjacent to the MgO barrier.

In Piotrowski et al. [14] we experimentally reported the effect of an electric field on the effective anisotropy values in sub-100 nm CoFeB/MgO/CoFeB MTJs with interfacial perpendicular magnetic anisotropy. A linear variation in the effective anisotropy values was observed with the bias as can be seen for devices of different sizes in Figure 2.5.

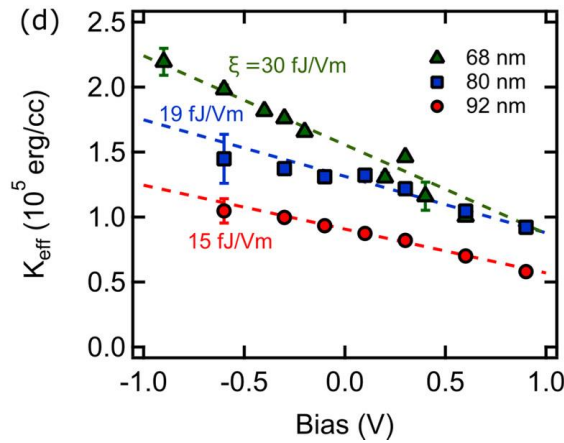


Figure 2.5 Effect of an Electric field on coercivity of top and bottom CoFeB layers. Figure taken from [14].

The linear behavior of the effective anisotropy with the bias voltage can phenomenologically be described using the following equation:

$$K_{eff} = K_{eff}^0 + \xi \frac{V}{t_{MgO}^2}, \quad 2.5$$

where, t_{MgO} is the thickness of MgO layer, V is the voltage across the magnetic tunnel junction, and the VCMA coefficient ξ parameterizes the PMA dependence on the applied electric field. The VCMA coefficient, typically in units of fJ/Vm, is a material and interface dependent parameter that quantifies the change in interfacial anisotropy energy (typically reported in units of fJ/m²) per unit of applied electric field (in units of V/m). Reported values of interface anisotropy and VCMA coefficient for Ta/CoFeB/MgO based MTJs typically are $K_i \sim 1\text{--}2$ mJ/m², and for the VCMA coefficient typically $\sim 20\text{--}50$

fJ/Vm [12] [15] [16] [17] [18]. The choice of the capping/seed metal layer can also change the PMA and VCMA of MTJs. For example, it has been shown that by replacing Ta layers with Hf and Mo layers can result in a larger K_i , leading to improvement in the thermal stability and TMR as well [19] [20].

2.7 Thermal stability factor

A high thermal stability is deemed necessary for data storage so that data is not erased due to random thermally induced magnetization reversals. In the simplest form, the thermal stability factor Δ due to the magnetic anisotropy and finite temperature is defined by

$$\Delta = \frac{E_b}{k_B T} = \frac{K_{eff} V}{k_B T}, \quad 2.6$$

where E_b is the energy barrier between P and AP configuration of the recording or the free layer of MTJ concerning the reference layer, k_B is the Boltzmann constant, T is the temperature, V is the magnetic volume of the layer and K_{eff} is the effective anisotropy energy. Here the energy barrier can also be expressed in terms of the effective anisotropy field and saturation magnetization as $E_b = M_s H_k V / 2$.

In the presence of effective magnetic field H and an STT current I through the MTJ, the thermal stability factor is modified according to the following equation [21]:

$$\Delta = \Delta_o \left(1 - \frac{H}{H_k}\right)^n \left(1 - \frac{I}{I_c}\right), \quad 2.7$$

where Δ_0 is the thermal stability factor with no effective field and current, I_c is the critical switching current for STT, n is a factor that depends on whether the device switches as a single domain or not. For coherent rotation $n=2$.

In the case of materials with perpendicular magnetic anisotropy, the thermal stability factor is modified:

$$\Delta = \Delta(V_{bias} = 0) - \frac{\xi A}{t_{MgO} k_B T} V_{bias} , \quad 2.8$$

where ξ is the VCMA coefficient, A is the area, V_{bias} is the voltage bias across the MgO based pMTJ, and t_{MgO} is the MgO thickness. The thermal stability factor of the MTJ during standby mode, when no voltage bias or an electric field acts on the device, is obtained by setting $V_{bias} = 0$. As an example, in Figure 2.6 the effect of voltage on thermal stability can be seen when measuring an RV loop. Switching between P and AP states can be seen and as the voltage bias is varied the thermal stability caused the frequency of switching to change in the loop. The RV loop was measured for an 80 nm pMTJ device with thermal stability $\Delta(V_{bias} = 0) = 15$ and at a sweep rate of 250 mV/sec (details about the stack can be found in [22]).

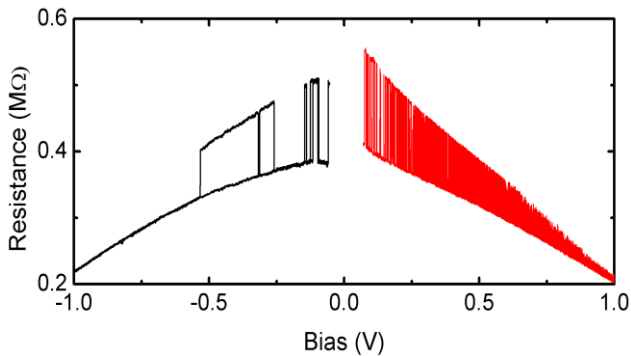


Figure 2.6 RV loop for a low thermal stability device. Lesser telegraphing is seen for negative bias where the free layer becomes stable and more telegraphing behavior is seen for positive bias which lowers the stability.

2.8 Niche for High and Low thermal stability MTJs

Results work reported in Chapter 6 and Chapter 7 of this thesis utilizes low thermal stability MTJs for applications whereas in Chapter 8 and Chapter 9 focused on switching high thermal stability devices. In the discussion below, I discuss application niche for high and low thermal stability MTJs.

Depending on the target of an application MTJs of with a particular thermal stability values may be needed. High $\Delta > 45$ corresponds to data retention time > 10 years. Magnetic Random Access memory or MRAM requires data retention time > 10 years and hence thermal stability values > 45 for non-volatile memory applications. Moreover, the thermal stability should be high enough even at 400°C which is the Back-end of the line (BEOL) temperature for the CMOS architecture during usual operation. For $\Delta \sim 30$ we get a data retention time of about 3 hours, which may be adequate for applications such as embedded memory with a relaxed retention time requirement. Applications such as stochastic computing and spiking neural networks where bit stream at high frequency is needed for faster performance, typically would need retention time in the range μs - ns and $\Delta < 10$ is desired.

Low thermal stability MTJs are of growing interest for a wide range of applications such as probabilistic computing [23–25], random number generators (RNGs) [26–28] and neuromorphic computing [29,30]. In simulation work by Camsari et al. [25], it was shown that the natural physics of stochastic fluctuations in MTJs very much mimics the mathematics of Boltzmann Machines and can thus provide the basis for probabilistic spin logic for a wide variety of low power computing applications. Some simulations [25] [23] that exemplify the performance of low thermal stability MTJs include- implementation of any given truth table reliably and reconfigurable, for example, AND, OR, XOR gates and character recognition; solving

difficult optimization problems, for example, traveling salesman problem and; implementation of relatively large logic operations by connecting basic probabilistic spin logic blocks in a directed manner, for example, 4-bit multipliers and 32-bit adders.

A MTJ with low thermal stability can also be used as a temperature sensor where recording the telegraph noise through the MTJ can be used to estimate the temperature of the MTJ. From equation 2.8, we can see that for a fixed value of VCMA coefficient and thermal stability factor at zero applied bias, the temperature can be calculated from the lifetime and the voltage that is applied across the MTJ. In Figure 2.7, we show as an example contour plot of temperature for a pMTJ device with a VCMA coefficient of 25 fJ/Vm and a thermal stability factor of 8 at zero applied bias voltage. The straight lines in the plot correspond to the contours of constant temperature and the red region corresponds to temperature values > 700 K where the device would be damaged. The distinct advantage of using MTJ as a temperature sensor lies in the fact that it could be used to sense temperatures at microscopic scales, with low current densities by using high RA product, and with very high accuracies depending on the time averaging to obtain the lifetimes, and would be easy to connect to, read and most importantly the integration compatibility with the present CMOS architecture.

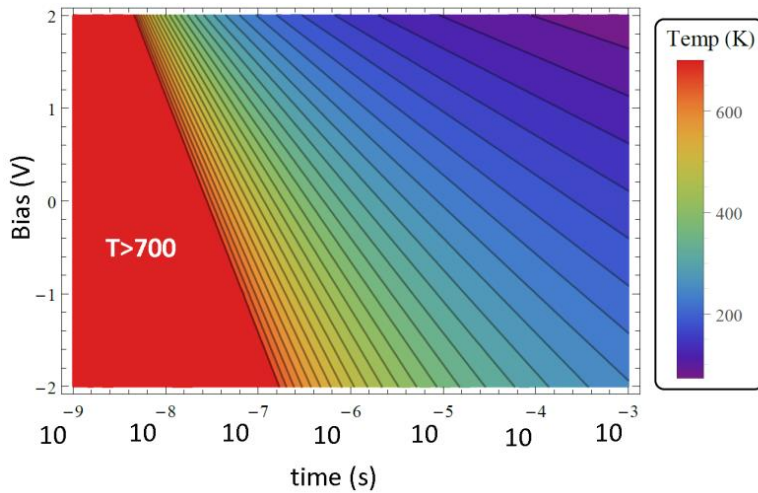


Figure 2.7 Contour plot of temperature of a pMTJ for depending on the lifetime and the applied voltage bias.

2.9 Notable developments so far

Recently, there have been multiple startling reports on advances in device designing and methodologies for fabrication and write operations in pMTJs which has led to further interest in research on these devices. An alternate stack design that is being explored is the use of double magnetic tunnel junctions to enhance the thermal stability of the recording layer. In recent work by Sato et al. in 2012 [31] which employs the MgO/CoFeB/Ta/CoFeB/MgO stack as the recording layer, the thermal stability factor of MTJ with the structure having a junction size of 70 nm was shown to increase by a factor of 1.9 from the highest value of perpendicular MTJs with single CoFeB-MgO interface having the same device structure. In a different work with single tunnel junction, but with thicker CoFeB recording layer than its diameter, it was shown that the pMTJs with high thermal stability >80 could be fabricated at device diameters < 10 nm [32]. The out of plane shape anisotropy at a smaller diameter and relatively large thicknesses of CoFeB was attributed to the perpendicular axis being the preferred easy axis. In 2016 Nowak et al. [33] from IBM demonstrated a record low write-error-rate (WER) for an 11 nm, to 7×10^{-10}

and demonstrated using a 10 ns write pulse with a write current of 7.5 μA , corresponding to a record low switching energy below 100 fJ. In another work improving on the fabrication process, it was shown that milling at angles perpendicular to the sidewalls could trim the device diameter at the functional layers below 20 nm sizes. Furthermore, with the discovery of spin-orbit torque effect of the heavy metals [34], the phenomenon has been widely studied in MTJ systems to switch the magnetization of the free layer by fabricating it adjacent to the heavy metal layer and using the spin currents. This eliminates the need of passing current through the high resistance tunnel barrier; however, the tunnel barriers are still needed to retain TMR for reading operations and for obtaining high thermal stability due to interfacial effects as discussed in section 2.3. In Chapter 8, I will discuss switching of a high thermal stability 20 nm pMTJ device using SOT of Ta. Challenges remain, however, in lowering the current density that is needed to produce spin currents sufficient to cause magnetization reversal, in fabricating three terminal devices to allow separate read and write channels and also in eliminating need of an external magnetic field to break the symmetry during magnetization reversal.

Chapter 3 Magnetization dynamics

In this chapter, I go through the phenomenology of magnetization dynamics based on the Landau-Lifshitz-Gilbert (LLG) equation. The LLG equation can be used to understand the effect of field, spin currents and damping forces that exert a torque on the magnetization of the magnetic material. The microscopic origin of magnetization is through the spin angular momentum of an electron inside an atom. Hence the dynamics of different forces that act upon the magnetization involves rotational mechanics which is what the LLG equations are theoretically based upon. The proportionality constants in the LLG equation capture both quantum mechanical as well as the relativistic effects. In this chapter, we focus on the phenomenology that would help understand the magnetization dynamics that are presented in the different Chapters of this Thesis.

3.1 LLG equation

In ferromagnetic materials, the magnetization dynamics in the presence of an effective magnetic field can be described by Landau-Lifshitz-Gilbert (LLG) equation:

$$\frac{\partial \mathbf{m}}{\partial t} = -\gamma \mathbf{m} \times \mathbf{H}_{eff} + \alpha \mathbf{m} \times \frac{\partial \mathbf{m}}{\partial t} \quad 3.1$$

where \mathbf{m} is a unit vector along the magnetization direction, $\gamma = g\mu_B/\hbar$ is the gyrometric ratio and α is the Gilbert damping parameter which causes the magnetization to dissipate momentum and relax to the equilibrium direction. Here, the effective field \mathbf{H}_{eff} can be a combination of external field, exchange field, and

anisotropy field. The first term on the right side of the equation causes magnetization to precess along \mathbf{H}_{eff} whereas the second term causes it to relax to this field direction due to damping. Note that the product of the gyromagnetic ratio γ and the effective magnetic field \mathbf{H}_{eff} has units of Hz. Therefore the inverse of this product gives a time scale for the magnetization dynamics induced by the effective field. This time scale is termed as the “intrinsic time” or “attempt time.” The typical magnitude of an effective field of a nanomagnet lies between milli-Tesla to a few Tesla, and thus the corresponding intrinsic time can vary between nanoseconds to tens of picoseconds.

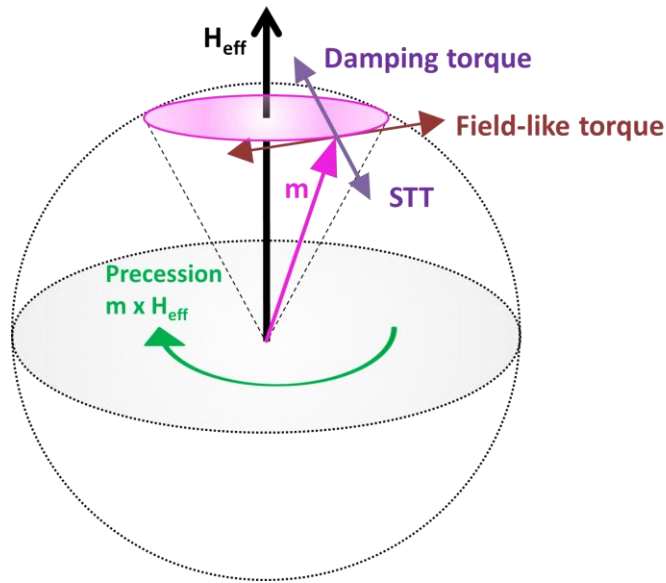


Figure 3.1 LLG dynamics (Equation 3.1). The magnetization (\mathbf{m}) precesses about the effective field direction (\mathbf{H}_{eff}). The purple arrow illustrates the direction of dissipative (damping) torque that directs \mathbf{m} towards the effective field direction. The spin-transfer torque acts opposite to the damping torque, and the red arrow shows the field-like torque for an electron with spin polarization parallel to the effective field.

3.2 Spin Transfer Torque switching

In 1996, Berger and Slonczewski independently proposed the use of spin-polarized current to manipulate magnetization in ferromagnets [35,36]. The phenomenon is basically based on conservation of angular momentum. If a spin-polarized current flows through a magnetization volume such that the magnetization is non-collinear with the spins, then the spins will try to align with the magnetization due to exchange interactions. Equal and opposite torques will then be exerted by the spins on the magnetization, due to conservation of angular momentum. If the torque due to the electron spins is sufficient, it will switch the magnetization direction. Such spin current-induced torque is called spin-transfer torque (STT). In FM-I-FM system one of the FM layers acts as a spin polarizer for current which then passes through the tunnel barrier and exerts a torque on the other FM layer. For such a system, an extra term can be added to equation 3.1 to account for STT:

$$\frac{\partial \mathbf{m}}{\partial t} = -\gamma \mathbf{m} \times \mathbf{H}_{eff} + \alpha \mathbf{m} \times \frac{\partial \mathbf{m}}{\partial t} - \overbrace{\gamma \frac{\hbar P}{2e} \frac{J_c}{M_s t} (\mathbf{m} \times (\mathbf{m} \times \mathbf{m}_{ref}))}^{\text{STT term}}, \quad 3.2$$

where J_c is the current density through the FM layer with thickness t , and \mathbf{m}_{ref} is a unit vector along the magnetization direction of the reference layer. The direction of STT is shown in Figure 3.1 with where \mathbf{m}_{ref} is taken collinear with \mathbf{H}_{eff} of the free layer. When magnetization is perfectly collinear with the \mathbf{m}_{ref} the STT term in equation 3.2 is zero due to the cross product in brackets. Thermal jitter usually initiates the magnetization reversal process. This is often termed as the incubation

delay in switching, which can be of the order of \sim ns. When electrons flow from the reference layer to the free layer, parallel alignment is favored. When electrons flow from the free layer to the reference layer, antiparallel alignment is favored. To achieve free layer magnetization reversal, the current density must exceed a certain critical value, which corresponds to the point where the Gilbert damping becomes balanced by the STT (also known as anti-damping torque). This critical current density J_c can be estimated using equation 3.2 for the condition where net effective damping is zero:

$$J_c = \frac{2\alpha e M_s t}{\hbar P} H_{eff} , \quad 3.3$$

This expression for the critical current density provides paths to reduce power consumption for spin-transfer-induced switching. In particular, the Gilbert damping factor α plays a important role and should be minimized, while the spin polarization should be maximized. The other parameters (t , M_s , H_{eff}) also influence the thermal stability of the magnetization, so a trade-off must often be found between minimizing the write current density and maintaining sufficient thermal stability to achieve the specified memory retention. Recall that the effective anisotropy field $H_{eff}=2K_{eff}/M_s$ and the thermal stability factor $\Delta=K_{eff}V/k_B T$, we can rewrite the expression for J_c from equation 3.3 as

$$J_c = \frac{4\alpha e}{\hbar P} \cdot \frac{k_b T}{A} \cdot \Delta . \quad 3.4$$

Since STT switching is determined by a current density threshold, this means that the current density required to perform a write operation in case of STT MRAM scales inversely to the area of the device. For very small device sizes, for which obtaining high thermal stability is a challenge, a reduction in area (A) must be

compensated by an increase in the anisotropy field to maintain a desired thermal stability value (to satisfy a particular requirement of data retention time). As a consequence, the current density has to scale inversely with the area, and hence higher current densities are needed for devices with smaller diameters while maintaining the same thermal stability values. This minimum current density value is usually of the order 10^6 A/cm² for commonly known materials, which currently allows for downsizing scalability of STT-MRAM to sub-20 nm sizes.

In the thermally assisted regime, where $I < I_c$, the switching probability is finite over a range of write current values. The switching probability is dependent on the energy barrier (equation 2.7) between the P and AP states and can be expressed by:

$$P_{sw} = 1 - \exp \left\{ -\frac{t_{pw}}{\tau_0} \exp \left[-\Delta_0 \left(1 - \frac{H}{H_k} \right)^2 \left(1 - \frac{I}{I_c} \right) \right] \right\}. \quad 3.5$$

Magnetic Back Hopping

When the free layer is acted upon by spin-polarized current through STT such that it attempts to switch the magnetization to the same state (for example from P to P state), the MTJ should not switch. However, there have been experimental observations [37] where the MTJ may switch back to the opposite state (AP in the example here). The back-hopping is observed in both current directions, corresponding to parallel-to-antiparallel and antiparallel-to-parallel switching. This phenomenon is frequently observed at current densities exceeding the threshold for STT switching and with samples with low magnetic anisotropy. The back-hopping process can be minimized by increasing the anisotropy (or the coercivity) of the MTJ.

Expanding the exponential term of equation 3.5, since the magnitude of its argument is $\ll 1$, the forward switching probability P_{sw-F} can be written as

$$P_{sw-F} \cong \frac{t_{pw}}{\tau_0} \exp \left[-\Delta_0 \left(1 - \frac{H}{H_k} \right)^2 \left(1 - \frac{I}{I_c} \right) \right] \quad 3.6$$

and the probability of back-hopping can then be expressed as

$$P_{sw-B} \cong \frac{t_{pw}}{\tau_0} \exp \left[-\Delta_0 \left(1 + \frac{H}{H_k} \right)^2 \left(1 + \frac{I}{I_c} \right) \right]. \quad 3.7$$

Since the forward and backward switching probabilities are very different, the switching rates and hence the lifetimes for P and AP states are asymmetric around I_c as will be shown in the experimental results presented in Chapter 6.

As depicted in Figure 3.2, back hopping is expected under conditions where excess spin torque can cause the MTJ to switch back to its original direction. This phenomenon of back hopping reduces the overall switching probability as a function of increasing current or bias and is undesirable for practical applications where a deterministic switch with low write error rate is desired. Sun et al. [38] showed that such behavior is due to a modified switching phase boundary in (\mathbf{V}, \mathbf{H}) space when there is a significant amount of reduction in the MTJ's anisotropy field H_k at elevated bias.

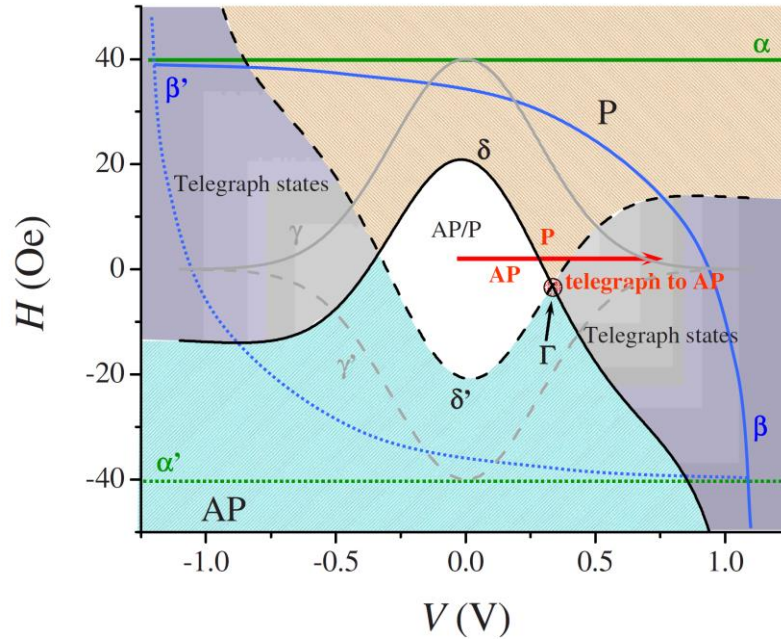


Figure 3.2 Different regions of telegraph noise based on external applied field H and applied voltage bias V (based on theoretical calculations). The solid and dotted lines designate AP-P and P-AP boundaries. Lines α and α' : a bias-independent zero-temperature H_k . Lines β and β' are the thermal-activation boundaries with spin-torque and finite temperature. Lines γ and γ' are the bias-dependent H_k . Lines δ and δ' are the thermal-activation boundaries with bias dependent H_k . The horizontal arrow shows a sweep of switching voltage from an AP-P switching to a crossing from P into the telegraph region, partially reverting to AP states, corresponding to the back hopping. Figure taken from Reference [38].

3.3 Spin-Orbit Torque switching

When unpolarized electrons flow through a heavy metal layer with high spin-orbit coupling, electrons with spins polarized in opposite directions separate across the thickness of the layer due to spin Hall effect in the heavy metal which arises from special theory of relativity. Consider an electron with velocity v moving relative to a heavy metal atom. In the electrons rest frame the E-field radiating from the nucleus

of the heavy atom becomes a B field (also radially varying), the magnetic field gradient causes deflection of the electron, with the direction dependent on the electron spin. Thus a transverse spin current is generated from a charge current. Absorption of this spin current by the ferromagnetic layer neighboring the heavy metal results in the transfer of spin torque to the ferromagnet. When a charge current flows through a heavy metal layer with large spin-orbit coupling such as Pt or Ta, a spin current J_s is generated:

$$J_s = \vartheta_{SHE}(J_c \times \sigma) \quad 3.8$$

where ϑ_{SHE} is the spin Hall angle, J_c is the charge current, and σ is the direction of the electron spin polarization. For a current flowing in-plane generating spin polarization σ that is also in-plane but orthogonal to the current direction, the spin current will flow perpendicular to the plane. If a FM layer is placed adjacent to this material that is generating spin current, the spin current will exert a torque on the magnetization. This effect of can be accounted for by modifying the LLG equation with an additional Spin Orbit Torque (SOT) term:

$$\frac{\partial \mathbf{m}}{\partial t} = -\gamma \mathbf{m} \times \mathbf{H}_{eff} + \alpha \mathbf{m} \times \frac{\partial \mathbf{m}}{\partial t} - \overbrace{\gamma \frac{\hbar}{2e} \frac{\vartheta_{SHE} J_c}{M_s t}}^{\text{SOT term}} (\mathbf{m} \times (\mathbf{m} \times \sigma)), \quad 3.9$$

It can be seen through the cross term on the very right of the equation that the SOT acts such that it tries to align the magnetization \mathbf{m} parallel to the spin direction σ . The origin of SOT is ascribed to spin accumulation at the heavy metal/FM interface which gets absorbed by the FM layer.

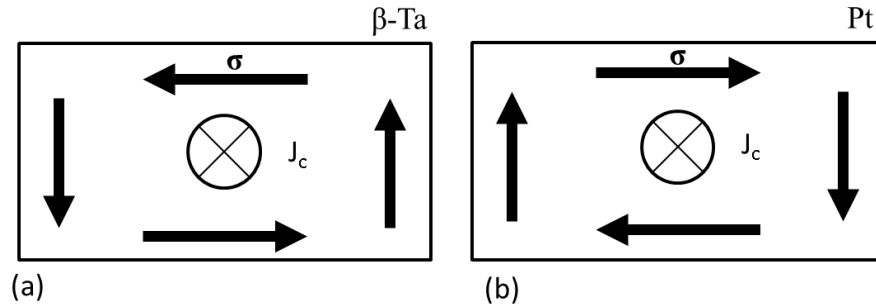


Figure 3.3 Direction of spin polarization of the accumulated spins at the surface in case of β -Ta and Pt (b) due to charge current J_c .

The spin Hall angle characterizes the efficiency by which the charge current J_c gets converted to spin current J_s . The spin Hall angle is a material property and is -0.15 for β -Ta and 0.07 for Pt. The sign of spin hall angle for Pt and Ta are opposite. This indicates that for the same charge current injection, the spin polarization accumulated at the boundaries is reversed. In the SOT term in Equation 3.9, the direction of the torque also depends on the direction of the in-plane current flow J_c . The direction of spin polarization of the accumulated spins on the surfaces of β -Ta and Pt is shown in Figure 3.3.

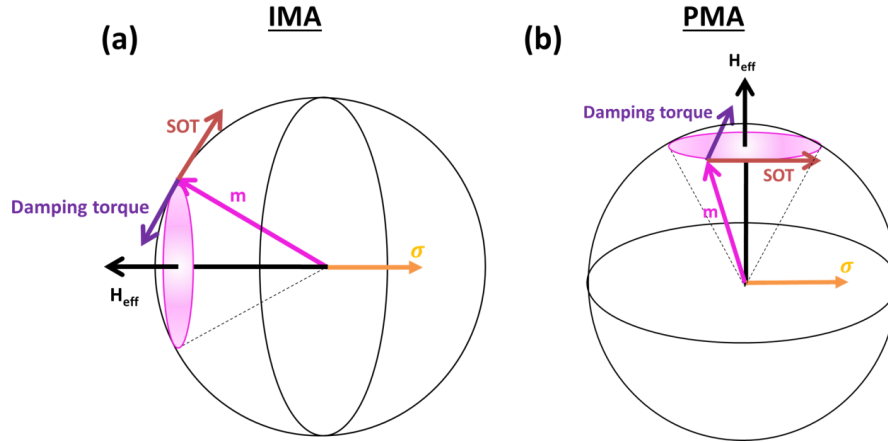


Figure 3.4 SOT in the case of (a) an in-plane easy axis with due to in-plane magnetic anisotropy (IMA) (b) an out-of-plane easy axis due to perpendicular magnetic anisotropy (PMA). In case of IMA the SOT competes directly with damping torque, whereas in the case of PMA, SOT may not compete directly with damping torque, depending on the azimuthal angle (in-plane).

For in-plane magnetized layers, the spin polarization and the easy axis are collinear and to switch the device with SOT, work has to be done against the damping torque, as can be seen in Figure 3.4(a). Hence, the SOT is in effect similar to spin transfer torque and renders no advantage in energy efficiency when switching materials with in-plane magnetic anisotropy (IMA). It may still be somewhat beneficial over STT because it would reduce the charge current flowing through the thin MgO barrier. However, for perpendicularly magnetized materials with perpendicular magnetic anisotropy (PMA), the SOT may not compete directly with the SOT term depending on the phase of the magnetization direction along the easy axis as shown in Figure 3.4 (b). The effect of the SOT is to cant the magnetization towards the spin polarization direction σ . When the magnetization points towards the spin polarization direction, which is along the hard axis or the in-plane axis of the free layer, an external field is needed to break symmetry for deterministic switching. Without an external field, the magnetization has equal probability to go to the up state or down state due to random thermal fluctuations. By

applying an in-plane external field along the direction of the charge current flow, symmetry is broken and switching from the up state to the down state or vice versa can be achieved. The stable configuration of the magnetization after the current pulse has canted the magnetization in-plane depends on the direction of J_c and the direction of H_{ext} . Bidirectional switching can thus be achieved by either of the following two ways (i) by keeping the direction of the external field fixed and changing the current direction, (ii) by keeping the direction of charge current fixed and changing the external field direction as shown in Figure 3.5.

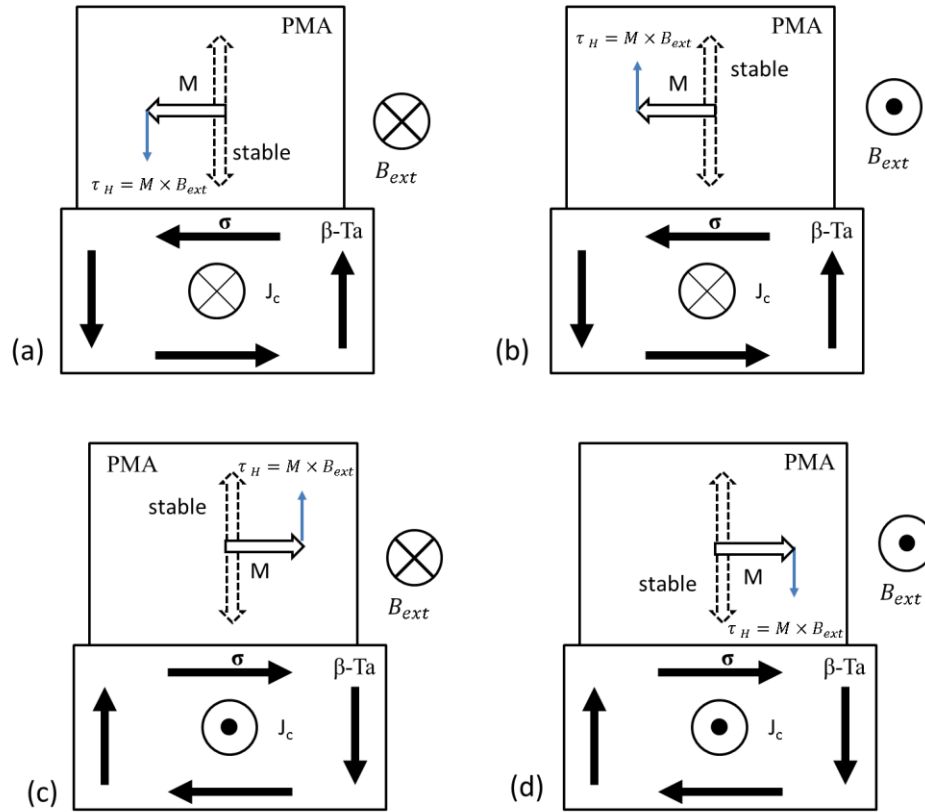


Figure 3.5 Stable magnetization switching direction due to SOT for of a PMA material depends on the direction of the charge current flow in β -Ta and on the direction of external field B_{ext} .

3.4 Combining SOT with STT for switching

For storage applications, MTJs with PMA are more scalable than MTJs with IMA, due to the higher thermal stability, as was discussed in Chapter 2. However, to switch a pMTJ by SOT, a magnetic field is needed to break the symmetry of the SOT, which adds complexity to stack structure. To avoid the need for an external applied magnetic field, Yu et al. in 2014 [39] used lateral symmetry-breaking to achieve current-induced switching of perpendicular magnetization by only an in-plane current. However, this requires an advanced fabrication process step for depositing a thin film with a uniform thickness gradient. Recently simulations have proposed an alternate write scheme where STT along with SOT can be used to obtain a deterministic switch in case of pMTJ. In Brink et al. [40] it was seen that while the spin current was by itself not sufficient to cause a switch by introducing some STT, causing current density to flow through the device, a switching probability as high as 0.99 can be achieved (see Figure 3.6(a)). Simulations showed the possibility of an eight-fold reduction in tunnel current density, corresponding to a fifty-fold reduction in write energy, and while maintaining a 1ns write-time was possible using this write scheme. A similar scheme was explored by Wang et al. in 2015 [41], where it was found that the switching speed of an STT-MTJ can be significantly reduced to less than 1 ns by using a sufficiently large spin-Hall write current density $\sim 25 \text{ MA/cm}^2$ with an appropriate duration $\sim 0.5 \text{ ns}$, as shown in Figure 3.6(b). It is interesting to note that in both the studies it was found that above a certain value of current density J_{SHE} the switching probability starts to decrease again for low values of J_{STT} . This is a manifestation of symmetrical switching nature of SOT which is inherently stochastic and which dominates the deterministic switching nature of STT for a small value of J_{STT} .

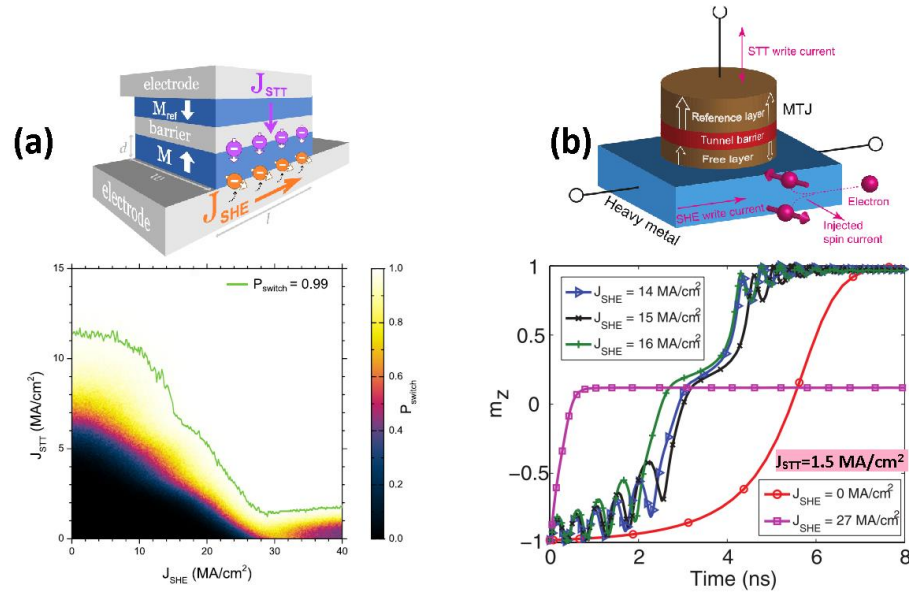


Figure 3.6 STT can be used along with SOT to switch a pMTJ. (a) A contour plot of the switching probability for different combinations of J_c and J_{STT} . Figure adapted from Brink et al. 2014 [40](b) The perpendicular magnetization evolves in the presence of a STT current density of 1.5 MA/cm² and different values of J_{SHE} . Figure adapted from Wang et al. 2015 [41].

Chapter 4 Magneto-static effects in patterned MTJs

To meet the demand for increasing storage densities, nanoscale magnetostatics at nanoscales has become an important topic of current research. In particular, dense arrays of sub-100 nm perpendicular magnetic tunnel junctions are of major technological interest for data storage. Lowering the device size can lead to distinct interactions between the different magnetic layers within a single device via their stray magnetic fields. This stray field coupling can be treated as additional anisotropy contributions, and can lead to stability or instability in switching. The magnetic field due to a uniformly magnetized element sets up according to the distribution of magnetic poles within the geometry. Hence, the shape of the individual magnetic layers can exert a strong influence on the stray field distribution and hence on the magneto-static interaction. In this Chapter, I present a systematic theoretical investigation using COMSOL simulations of the stray field distributions and their typical strength arising from PMA materials of varying diameters and fixed thickness values that are typically used in actual devices. The calculations made by COMSOL are based on the classical laws of magnetostatics, and the solutions are analytical. Results from COMSOL are used to interpret asymmetry in energy barriers for P to AP and AP to P transitions that I observe experimentally.

4.1 Introduction

Perpendicular magnetic tunnel junctions (MTJs) are under active investigation for potential use in magnetic random access memory (MRAM) [15,17,39,42]. Their

perpendicular magnetization reduces the current density required for spin transfer torque switching, and even lower densities have been reported for thin CoFeB/MgO/CoFeB junctions with voltage-assisted switching [16]. An important question for both types of MTJ is how the switching characteristics will scale as the device diameter is reduced. Our previous work [22] has shown that the tunnel magnetoresistance (TMR) minor hysteresis loop, where only the soft layer switches, is shifted due to the magnetostatic field of the hard layer below it (Figure 4.1 (a)). Here we demonstrate through experiments and simulations that this field also affects the switching mechanism so that the antiparallel (AP) to parallel (P) reversal is different from P to AP. We also show how the impact of the magnetostatic field becomes more pronounced for smaller MTJ diameters.

4.2 Sample Information

MTJ thin films were grown by sputter deposition onto thermally oxidized Si wafers. After annealing to develop perpendicular anisotropy, a combination of electron beam lithography and reactive ion etching was used to prepare arrays of nanopillars of different sizes. The final layer structure was Si/SiO₂ (1 μ m)/Ta (7 nm)/Ru (26 nm)/Ta (7 nm)/Co₄₀Fe₄₀B₂₀ (0.82 nm)/MgO (2.1 nm)/Co₄₀Fe₄₀B₂₀ (1.23 nm)/Ta (10 nm)/Ru (20 nm). Scanning electron microscopy was used to determine the pillar diameter after pattern transfer.

4.3 Measurement of telegraph signal using CAFM

Atomic force microscopy (AFM) showed that the average pillar height was 28 nm, so part of the Ru was etched. Conductive AFM (C-AFM) was used to make TMR measurements on individual nanopillars. Both full and minor hysteresis loops of TMR as a function of the applied field H_{appl} were measured using a ramp rate of 345 Oe/s, to

determine the switching fields of the hard and soft layers. For the voltage range used, the current densities were low, and spin transfer torque effects were negligible. Simultaneous topography and current maps were first recorded to identify locations of individual nanopillars. The probe was then moved on top of an individual nanopillar to perform transport measurements in constant force mode. Nanopillars between 50 and 100 nm diameter were found to have a constant RA product of $2.64 \text{ k}\Omega\text{m}^2$, consistent with an MgO thickness of 2.1 nm. Minor loop measurements were then made by sweeping the magnetic field at a constant magnetic sweep rate of 345 Oe per second through the desired range. The hard and soft layers were first initialized in a parallel configuration by applying large positive (800 Oe) out-of-plane magnetic field. The external magnetic field was then reversed to a low negative value (100 - 150 Oe) where the soft layer would telegraph. The external magnetic field and voltage values were held constant during the current vs. time trace measurements. Depending on the frequency of the switching events, a sampling rate in the range 100 kHz -100 MHz was used. At constant fields within the hysteretic region, the TMR was measured as a function of time, and the TMR value fluctuated between characteristic values corresponding to AP and P orientations of the soft and hard layer moments. Figure 4.1(b) shows how the average time spent in the high and low resistance levels varied over a small range of the applied field.

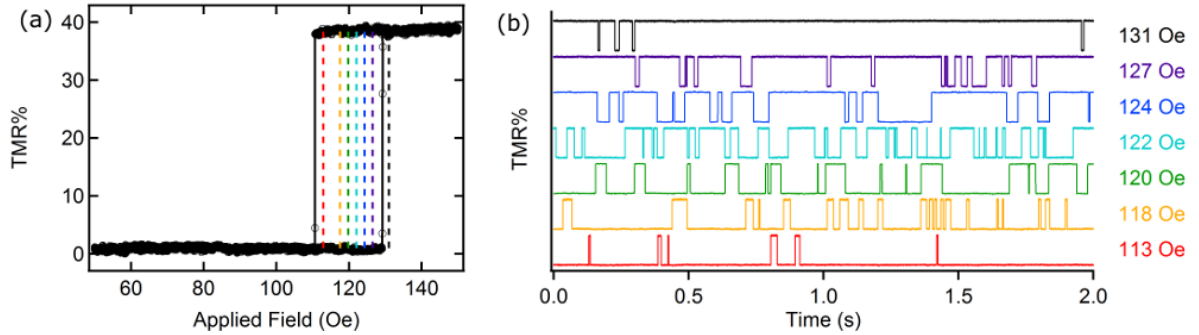


Figure 4.1 (a) TMR minor loop (solid line) for a 70 nm diameter MTJ, measured with a ramp rate of 345 Oe/s and bias of + 100 mV. At 140 Oe, the MTJ is stable in the AP state, and at 100 Oe it is stable in the P state. At fixed fields in between (dashed lines) it switches thermally as a function of time, as seen in (b). As the field is reduced, fluctuations to the P state appear at 131 Oe. By 113 Oe the MTJ is spending most of the time in the P state. Reprinted from [43].

4.4 Slope asymmetry

Telegraph noise can be analyzed in terms of an Arrhenius-Néel-Brown law to determine the lifetimes [44,45] of the high and low resistance states, τ_{AP} , and τ_P , respectively. Figure 4.2 shows plots of $\ln(\tau/\tau_0)$ as a function of the applied field, where τ_0^{-1} is the attempt frequency (~ 1 GHz) and $k_B T$ is the thermal energy. In Figure 4.2 (a) the slopes of the lines associated with τ_{AP} and τ_P are not equal. When the same nanopillar is initialized with the hard layer magnetized upward, the sign of the slopes reverses. τ_{AP} has a steeper slope regardless of which direction the hard layer is initialized. The effect is observed for all pillars where changes in telegraphing can be observed over a reasonable range of fields and measurement times. MTJs with diameters between 60 and 80 nm routinely showed telegraphing close to the switching field. 90 and 100 nm devices rarely telegraphed during the 20 s time window. Below 100 nm the minor loop coercivity showed a roughly linear decrease with size, so the larger devices were more stable with

respect to the thermal fluctuations. Similar characteristics have been reported elsewhere for smaller sizes where the devices used CoFeB alloys with higher anisotropy [46].

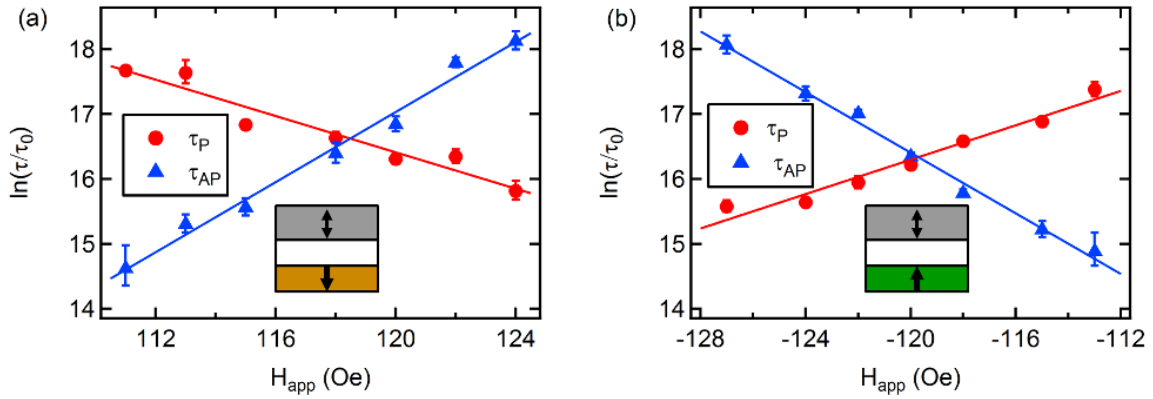


Figure 4.2 (a) $\ln(\tau/\tau_0)$ versus H_{app} , measured at 300 mV, showing data for the same 70 nm MTJ initialized with the hard layer magnetized downward (a) and upward (b). Reprinted from [43].

4.5 Calculation of H_{ms} using COMSOL

The effective field at the soft layer, H_{eff} , depends on both the applied field H_{appl} and the magnetostatic field H_{ms} due to the hard layer. COMSOL software was used to simulate the local field at different positions within the soft layer. The hard layer was modeled as a thin cylinder with thickness 0.82 nm and was assumed to be uniformly magnetized out of plane with $M_s = 1130$ emu/cc, a value obtained for $\text{Co}_{40}\text{Fe}_{40}\text{B}_{20}$ films prepared by the same method [18].

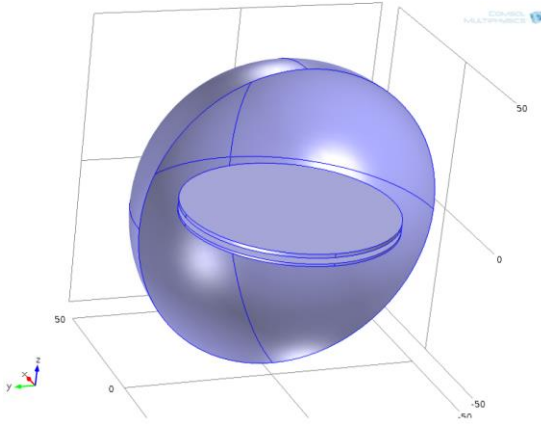


Figure 4.3 Snapshot of the geometry used in COMSOL simulation. The bottom disk acts as fixed PMA layer and stray field is calculated at the middle of disk on top which acts as a free layer. The disks are surrounded by air in the simulation marked by the spherical boundary as shown.

Maxwell's equations for current-free regions were used to determine the field patterns emanating from the uniformly magnetized hard layer. Simulations of the perpendicular field generated by uniaxial prisms show a strong dependence on the aspect ratio [47]. Figure 4.4 (a) plots the vertical component of the magnetostatic field $H_{ms,z}$ as a function of lateral position in the center of the soft layer. $H_{ms,z}$ varies spatially, while H_{appl} is uniform. When H_{appl} is large, it more than cancels $H_{ms,z}$ everywhere in the soft layer and the AP state is stable (Figure 4.4 (b)). If it is tiny, the effective field H_{eff} can be less than zero everywhere, and the P state becomes stable. In between the AP state is more stable in the center while the P state is more stable near the edges, and thermal fluctuations can cause telegraphing between completely P and AP configurations.

If the net field within the soft layer were spatially uniform, then the sign of H_{eff} would determine the likelihood that a thermal fluctuation leads to switching. In this case, the slopes of τ_{AP} and τ_P as a function of the field in Figure 4.2 would be equal and opposite. With a nonuniform H_{eff} , the local value determines how likely the nucleus is to grow. Suppose the soft layer is initially in the AP state, and H_{appl} is within the telegraphing range. A thermal fluctuation that reverses a small region in the center of the soft layer will tend to revert since AP alignment is more stable there. However, a small region

reversing near the edge will tend to expand quickly around the rim of the soft layer, where P alignment is favored by the local H_{eff} . Because the spins are exchange coupled to those in the center, the entire soft layer will switch its magnetization direction. In other words, AP to P reversal tends to nucleate at the edge.

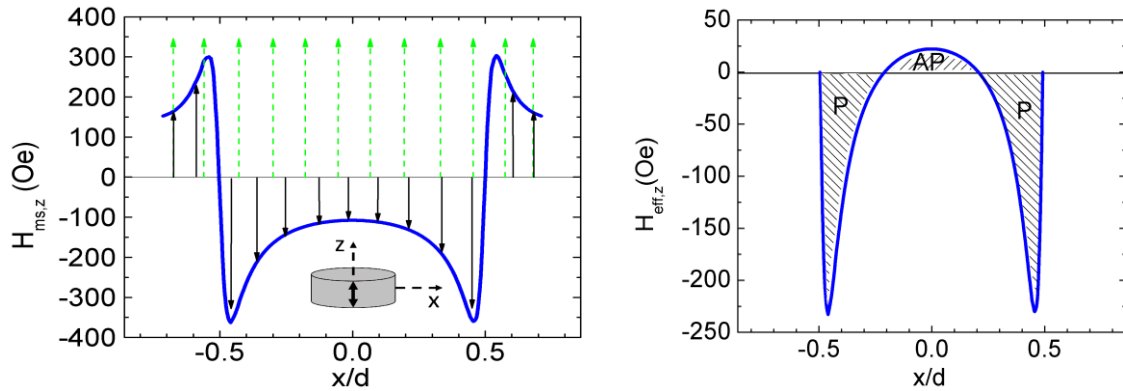


Figure 4.4 (a) Height-averaged $H_{\text{ms},z}$ at the soft layer, due to a hard layer magnetized downward, for an MTJ with diameter $d = 70$ nm. Solid arrows indicate the direction of $H_{\text{ms},z}$. The dashed arrows indicate the direction of H_{appl} , which is spatially uniform. (b) $H_{\text{eff},z}$ when $H_{\text{appl}} = 130$ Oe. For the range of H_{appl} where telegraphing occurs, $H_{\text{eff},z}$ is positive in the center of the soft layer but negative near the edges. Reprinted from [43].

When a nucleus forms at large H_{appl} , it is less likely to be in a region favoring P alignment, and therefore less likely to lead to reversal. At small H_{appl} it is more likely. Therefore the slope of τ_{AP} in Figure 4.2 is higher than it would be if $H_{\text{ms},z}$ were spatially homogeneous. In contrast, P to AP switching will occur when there is a thermal fluctuation reversing a small region of the interior, but not for fluctuations near the edge. The slope of τ_{P} should be smaller than for homogeneous $H_{\text{ms},z}$.

Previous studies of Co/Pd nanodots have also found the edge- and center-nucleated reversal and that patterning by ion milling leads to preferential edge nucleation [48]. In perpendicular spin-valve nanopillars, asymmetric telegraph noise has been observed

between the P state and a state containing a domain wall [49]. Unlike in the spin-valve nanopillars, our MTJs show no evidence of intermediate states with domain walls; the AP and P resistance values measured in the telegraph noise are consistent with the values found in the TMR major loops. Here the asymmetry in the telegraph noise arises from differences in the reversal mechanism starting from the AP and P states. The edge-initiated reversal has been reported for 50 nm x 300 nm perpendicular nanopillars containing notches and associated with magneto-static effects increasing the barrier for P to AP switching [50]. Here we see that this effect extends to circular nanopillars and small diameters.

When the lifetimes τ_{AP} and τ_P are equal, the average H_{eff} is assumed to be zero. From the data of Figure 4.2, this corresponds to an energy barrier E_b that is approximately 6.8×10^{-13} ergs. For coherent rotation, the corresponding effective anisotropy $K_{eff} = E_b/V$, would be 1.45×10^5 ergs/cm³, closer to that of bulk Co₄₀Fe₄₀B₂₀ and much lower than that predicted for thin films with perpendicular interface anisotropy. This supports nucleation of a small volume within the soft layer, followed by rapid domain wall motion. Once a nucleus is created by thermal fluctuations, it can either revert or grow to reverse the entire soft layer. The likelihood of reversal depends on the location where the nucleus is formed, and it is field-dependent because the proportion of areas favoring AP and P orientations change with H_{appl} . The slope of $k_B T \ln(\tau/\tau_0)$ as a function of H_{appl} is on the order of $M_s H V_{soft}$, where V_{soft} is the volume of the entire soft layer. In the reversal process, small nuclei are created by thermal fluctuations, but the likelihood of full reversal depends on their location.

4.6 Effect of size on x and z component of H_{ms}

Figure 4.5 shows how the vertical and radial components of \vec{H}_{ms} vary with the diameter

of the MTJ. Near the edges the angle of \vec{H}_{eff} will change with H_{appl} , but it will always be downward and inward over the telegraphing range. The vertical component increases at both the edges and the center as the diameter shrinks. The radial component near the edges is significant but weakly size-dependent. As the diameter is reduced, the ratio of the radial to vertical amplitude decreases. These values are shown in Table 4.1.

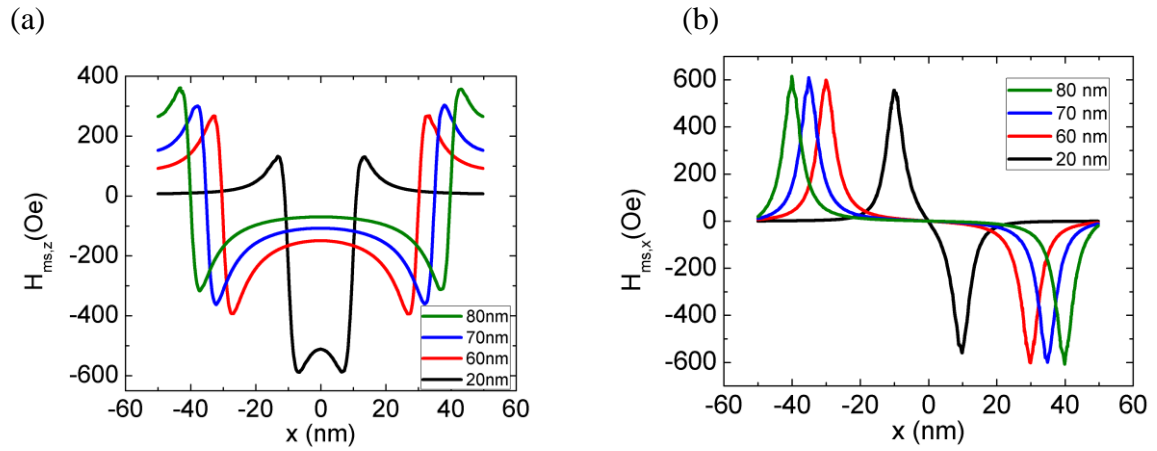


Figure 4.5 Vertical (a) and radial (b) components of \vec{H}_{ms} for MTJs of different diameters.

While MRAM would not be operated in or near the telegraphing regime, there are important consequences of our findings. AP to P switching starts at the edge while P to AP reversal begins in the interior, due to the spatially varying magnetostatic field of the hard layer. With different switching mechanisms, there could also be different switching times or more device-to-device variability for edge-initiated reversal due to differences in surface roughness. As the diameter of the MTJ is reduced, magnetostatic destabilization increases throughout the soft layer.

Table 4.1 Average in-plane and perpendicular magnetostatic fields at different locations of the soft layer

Diameter (nm)	Center ($H_x = 0$) H_z (Oe)	Edge H_z (Oe)	Edge H_x (Oe)	Edge H_z / H_x
20	501	589	561	1.05
60	149	394	602	0.65
70	107	363	600	0.61
80	70	317	608	0.52
250	30	348	640	0.54

4.7 Effect of Magnetic dead layer

The average in-plane and perpendicular magnetostatic fields at different locations of the soft layer, as a function of the MTJ diameter, are summarized in Figure 4.6. In all cases the hard layer thickness is 0.82 nm, the soft layer thickness is 1.23 nm, and the MgO spacer thickness is 2.1 nm. Following Ikeda, et al. [17], who reported a 0.5 nm magnetic dead layer for the top CoFeB electrode due to intermixing with Ta, the values are shown in the table reflect the fields in the middle of the *magnetic* portion of the top layer, due to the hard layer. The results with and without the dead layer are indistinguishable at the center and differ by less than 10% at the edge as can be seen in Figure 4.6.

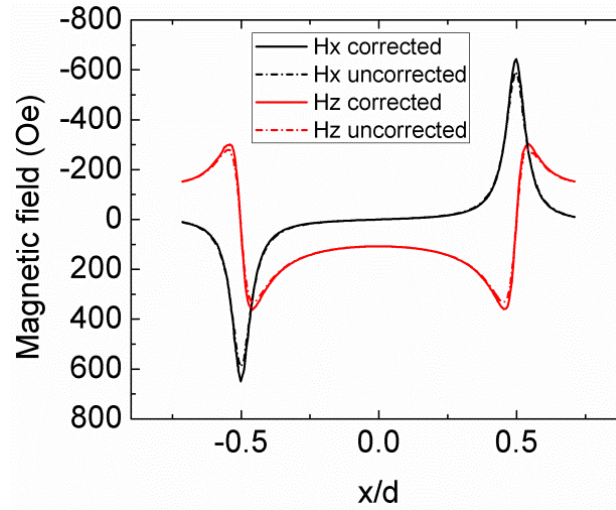


Figure 4.6 H_x and H_z components of the magnetic stray field with and without the 0.5 nm magnetic dead layer in.

4.8 Conclusion

There are two possible ways to mitigate the problem of magnetostatic fields in magnetic tunnel junctions. One route is to use a synthetic ferrimagnet to cancel \vec{H}_{ms} . Double tunnel junction MTJ structures of this sort have no magnetostatic loop shift [50]. An alternative approach would be to pattern the soft layer but not the hard layer, increasing the spatial uniformity of the magnetostatic field without the need for additional processing steps.

Chapter 5 Thermally robust sub 100 nm Mo/CoFeB/MgO tunnel junctions with perpendicular magnetic anisotropy

In this Chapter, I present fabrication and device testing of thermally robust sub-100 nm Mo/CoFeB/MgO tunnel junctions with perpendicular magnetic anisotropy. The samples were annealed at 400 °C before patterning to investigate if the magnetic properties are still maintained for integration with CMOS technology, wherein the back-end processes are usually run at such temperatures. I also investigate the voltage effect on magnetic anisotropy and field assisted switching in Mo-capped pMTJ structures with diameters ranging from 25 to 100 nm. Voltage control of the magnetic anisotropy (VCMA) is of immense interest because it allows for switching at very low current densities compared with those needed for spin transfer torque (STT) -based reversal. In Chapter 4, I demonstrated the effect of size and stray field on different switching behavior of antiparallel to parallel (AP-P) and parallel to antiparallel (P-AP) magnetization states. Here I investigate the effects of size and stray field on the switching current densities needed to get pure VCMA or field-assisted VCMA switching.

This work was done in collaboration with Hamid Almasi and Weigang Wang from the University of Arizona who deposited the Mo-capped pMTJ film stacks for the study. I performed the patterning and testing of the devices at CMU. Cross sectional

tunneling electron microscopy was done on the patterned devices by Congli Sun and Paul Voyles at University of Wisconsin-Madison.

5.1 Introduction

MTJs prepared with an annealing temperature above 250 °C cause the magnetization to reorient from an in-plane easy axis to an out-of-plane easy-axis due to the development of interfacial magnetic anisotropy post annealing. As deposited the layers are highly disordered. The crystallized bcc (001) structure of CoFeB epitaxial with a bcc(001) MgO tunnel layer is known for its exceptional properties such as high spin polarization, high TMR and high magnetic anisotropy. Hence, CoFeB-MgO based pMTJs have emerged as one of the most promising candidates for MRAM devices. Normally a Ta capping layer assists in the CoFeB layer crystallization into bcc (001) texture by absorbing the boron atoms during the annealing process [51]. In a recent work by Worledge, et al. [15], it was demonstrated that MTJs with Ta as a seed layer show a tunneling magnetoresistance ratio of 47% and a low switching voltage of 290 mV, giving a high switching speed of 1 ns. It has been shown through experimental investigations that the Ta/CoFeB interface can play a significant role in developing PMA, in addition to the CoFeB/MgO interface [52]. Recently, in work by Meng, et al. [53] it was shown that using a 5 nm Ta seed layer and a 10 nm Ta cap layer in CoFeB/MgO/CoFeB MTJ improved the interfacial anisotropy and enhanced the TMR ratio from 8% TMR pre-annealing to ~72% post annealing. Wang, et al. [54] reported similar enhancements using Ta as seed and capping layers. While a Ta layer remains the most widely used in MTJ stacks, recently other transition metals such as Hf [19], Mg [55], W [56] and Mo [54,57,58] have also been shown to improve PMA and thermal stability in CoFeB/MgO-based systems. Recent work by

Almasi, et al. [57] showed a large TMR with improved PMA and high thermal stability for CoFeB/MgO-based p-MTJs using Mo as both the seed and as a capping layer. It was hypothesized that the large formation energy of Fe-Mo was the physical reason for improved PMA even at elevated temperatures. The observations corroborate with observations reported by Fang, et al. [54] where they saw similar enhancements in the magnetic properties. In Almasi, et al. [20] it was shown that the excellent boron absorption property of Ta can be capitalized on by introducing an ultra-thin (<1 nm) Mo dusting layer that still promotes crystallization of CoFeB (001) compared to the Mo film layer, which favors a (110) oriented crystalline structure.

A comparative study in work by Almasi, et al. [57] found Mo superior to Ta in obtaining PMA, as well as high TMR of up to 162% even at an annealing temperature of 400 °C. For integration of MTJs with CMOS architecture, where the back end of the line (BEOL) temperature may reach 400 °C, the MTJs must retain high thermal stabilities and TMR after exposure to such elevated temperatures. Most reports of superior properties were for devices annealed at temperature of 350 °C or below. The properties often degrade at higher temperatures. Work by Kim, et al. [56] using a W spacer reported TMR above 100% for a CoFeB free layer sandwiched between two MgO layers, switching at almost half switching current $2 \times 10^6 \text{ A/cm}^2$, and a thermal stability factor twice as that for a MgO/CoFeB/Ta free layer. Thomas, et al. [59] successfully implemented a similar double barrier MTJ integrated with 90 nm CMOS based 8 Mb chips, in which the PMA was maintained even at 400 °C. They also found a thermal stability factor $\Delta > 100$ at room temperature and $\text{TMR} > 150\%$ for their sub-40 nm diameter MTJ devices. However, these studies are based on double magnetic tunnel junctions which are often challenging to grow due to complicated stack structures and annealing requirements, and also difficult to pattern to small sizes due to large aspect ratios which limit their usage.

In this work, we demonstrate high TMR and PMA in patterned single tunnel junction devices down to 25 nm in sizes with Mo used as a material for the seed and capping layers.

5.2 Experimental

The MTJ stacks used in this study have the following stack structure, from bottom to top: Mo(6)/Ru(10)/Mo(9)/Co₂₀Fe₆₀B₂₀(0.8)/MgO(~1.2)/Co₂₀Fe₆₀B₂₀(1.5)/Mo(7)/Ru(8), where the numbers in parenthesis are thicknesses in nanometers. The materials were deposited onto silicon wafers in a 12-source UHV sputtering system. During deposition, a residual gas analyzer was used to monitor the H₂O partial pressure. The base pressure was in the range of 10⁻⁹ Torr and the substrate was held at ambient temperature during deposition. The metallic layers were deposited by DC magnetron sputtering under an Ar pressure of 2 mTorr. The MgO layer was deposited by RF magnetron sputtering at 1.2 mTorr of Ar pressure. The sample was then annealed at 400 °C for 240 post deposition which causes the amorphous CoFeB to change to crystalline bcc due to solid state epitaxy. A 25 nm SiN_x layer was then deposited using DC sputtering to act as mask material for electron beam lithography (EBL). A 2% HSQ negative tone EBL resist was then spin coated at 3000 rpm for 45 secs. The sample was then treated at 190 °C for 2 mins on a hotplate to get rid of the volatile solvents. A Sirion 600 SEM was used for EBL with NPGS software to pattern features in the size range 20-100 nm. MF-CD 26 developer was used to develop the patterns post EBL. Reactive Ion Etching (RIE) with CHF₃/CF₄ was done to transfer the EBL patterns into the SiN_x hard mask. Ar Ion milling at a 22.5° angle of incidence was done to avoid tapering in the devices. The stack was milled down to the bottom Ru layer, and the endpoint was determined by secondary ion mass spectrometry.

Another short milling, equal to one complete rotation of the sample, was performed to clear any re-deposition. To etch away any residual mask materials from the top of the patterned nanopillars, RIE was done using CHF_3/CF_4 .

5.3 Imaging post patterning

Post patterning, imaging was done using SEM to check the true doameters of the devices, cross sectional TEM for a sideview of the layer structures, and conductive atomic microscopy images were taken to check the device height and conductivity through the devices. The imaging results are shown in Figure 5.1. The smallest size devices were 25 nm in diameter, as shown in Figure 5.1(a), (b). The true sizes of the different patterned devices used in this study were found using SEM imaging.

To study the effect of our patterning process on the sidewalls of the patterned features, cross sectional tunneling electron microscopy (XTEM) and elemental mapping (EDX) images were taken to study re-deposition and extent of device damage caused due to Ar ion milling. For this, 150 nm wide lines were written using EBL procedure similar to as described above and milling was done down to the MgO layer, leaving the bottom CoFeB layer unpatterned. Figure 5.1(c) shows a high magnification image of right edge of the device. An amorphous region can be seen at where the milling was stopped. Electron energy loss spectroscopy (EELS) mapping indicates that elements such Co, Fe, and Mo are all present in this amorphous region indicating the re-deposition during Ar ion milling. The redeposited materials do not entirely coat the sidewall of the device, and the Fe and Co are likely oxidized ($\sim 1\text{-}2$ nm) and so the possibility of a shorted circuit path is less likely. In fully patterned sub-100 nm devices we do not observe any shorts due to redeposition or otherwise. Furthermore, the XTEM revealed some non-uniformity in the MgO thicknesses,

which were found to be 1.5 ± 0.5 nm. The effect of roughness averages out for devices with diameters larger than 50 nm, but is expected to cause significant device to device variations for smaller structures, as we also observe in some of our smaller devices. A clear correlation in the columnar grain structure was seen in the Ru, Mo and CoFeB layers and the roughness in the CoFeB layer followed the grains in the Ru and Mo. This observation indicates the crucial role of the bottom Mo seed layer in determining the overall roughness of the various layers that form the MTJ structure.

Conductive atomic force microscopy confirmed a uniform height ~ 35 nm across different devices, as can be seen in the topography map Figure 5.1(e) and the line profile taken from the topography map of Figure 5.1(f). Devices of the same sizes were found to have similar conductivity as can be seen in conductivity maps in Figure 5.1(g), where all devices are in the parallel state (low resistance), and Figure 5.1(h), where all the devices are initialized in the AP state (high resistance) using an external magnetic field. There were no signs of electrical shorting due to redeposition on the sidewalls during milling.

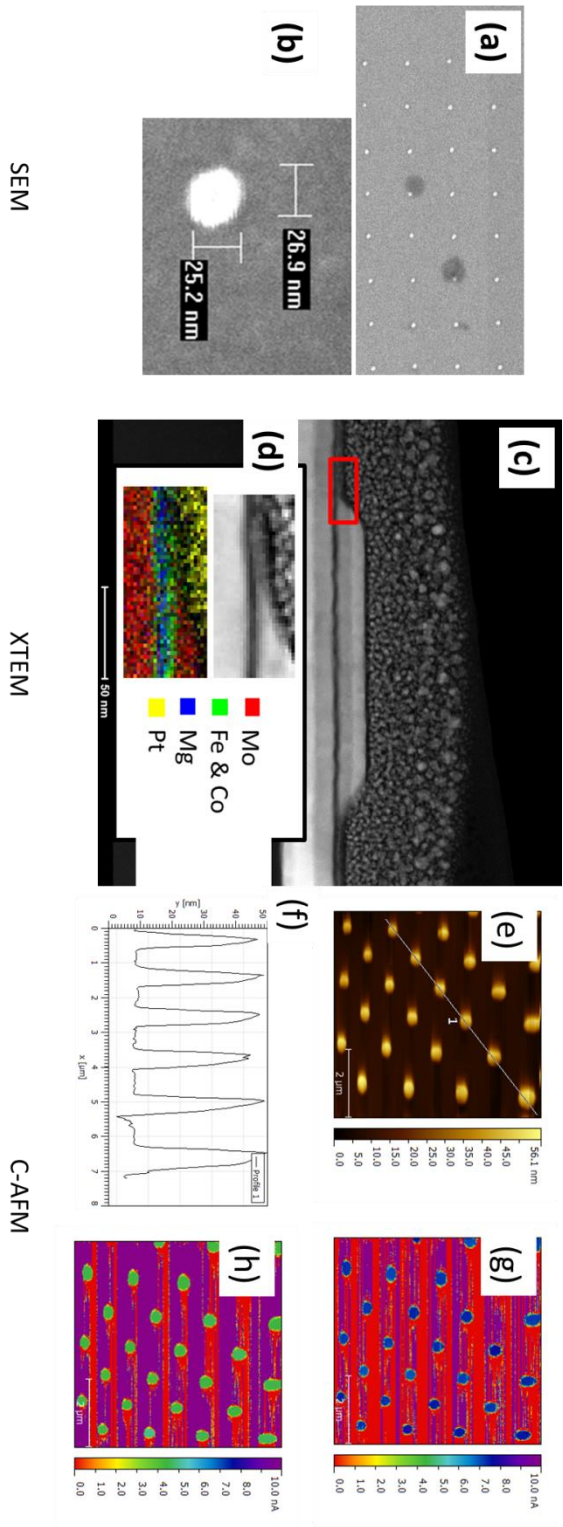


Figure 5.1 (a) SEM image of multiple 25 nm MTJs. (b) Magnified SEM image of a single 25 nm device. (c) XTEM cross section of a 150 nm diameter feature (d) EDX elemental mapping on the bottom of the patterned structure (red box in (c)) showing tapering but no re-deposition. (e) AFM topography of devices showing uniform height, as can be seen in the line profile (f). Color maps showing current through devices in the P (g) and AP states (h).

5.4 Variation in H_c , TMR and $H_{ms,z}$ with size

To characterize the magnetic properties such as coercivity, loop shift and TMR, transport measurement on individual pMTJs devices were done using C-AFM. A Ru layer on top of the devices acted as a conductive electrode and a C-AFM tips with a 200 nm Pt coating were used to ensure good electrical contact with the devices (resistance < 50 Ohms) with a typical contact force ranging from 25-30 nN. Minor resistance vs. magnetic field (RH) loops were recorded for the free layer using a field sweep rate of 250 Oe per second. Typically 100 (RH) loops were measured at a 100 mV voltage bias to find the statistical averages of the different parameters summarized in Figure 5.4(a-d). Half the loop width gives the coercivity H_c for the free layer. The coercivity remained roughly constant in the size range 35-100 nm and decreased sharply for 25 nm size devices as shown in Figure 5.2(a). Previously, in the case of $\text{Co}_{40}\text{Fe}_{40}\text{B}_{20}$ pMTJs with Ta capping [14], the coercivity dropped sharply below 80 nm, and the maximum coercivity was only about 80 Oe with thermal stability of around 18. Sato et al. [31] reported similar observations where the coercivity dropped sharply below 30 nm for double magnetic tunnel junctions with a $\text{MgO}/\text{CoFeB}/\text{Ta}/\text{CoFeB}/\text{MgO}$ structure for the free layer. In contrast we observe our MTJs to be fairly stable with a relatively simple single tunnel junction structure and with a single layer of Mo capping. In our patterned pMTJs, below 35 nm we expect single domain behavior during magnetization reversal, whereas above 35 nm we expect reversal via nucleation and domain wall motion.

We found $\text{TMR} > 120\%$ in all of the patterned devices across the different sizes as shown in Figure 5.2 (b). RA product was obtained by fitting a linear curve through resistance vs. the inverse of the device area plot as shown in Figure 5.2(c) which gave $\text{RA} = 18.14 \text{ k}\Omega\text{-}\mu\text{m}^2$ for devices measured at 100 mV in their low resistance states. The RH loops were shifted from zero field due to the stray field from the

patterned bottom layer. The effect of patterning on the strength of stray field has been discussed in detail in Chapter 4. The stray field increases with the decreasing sizes, as expected from our COMSOL simulation results. For this sample, the measured values of stray fields are shown in Figure 5.2(d). Below 35 nm a crossover between the coercivity and stray field values can be seen, indicating that the devices prefer to be in P state during standby (with no applied field and voltage).

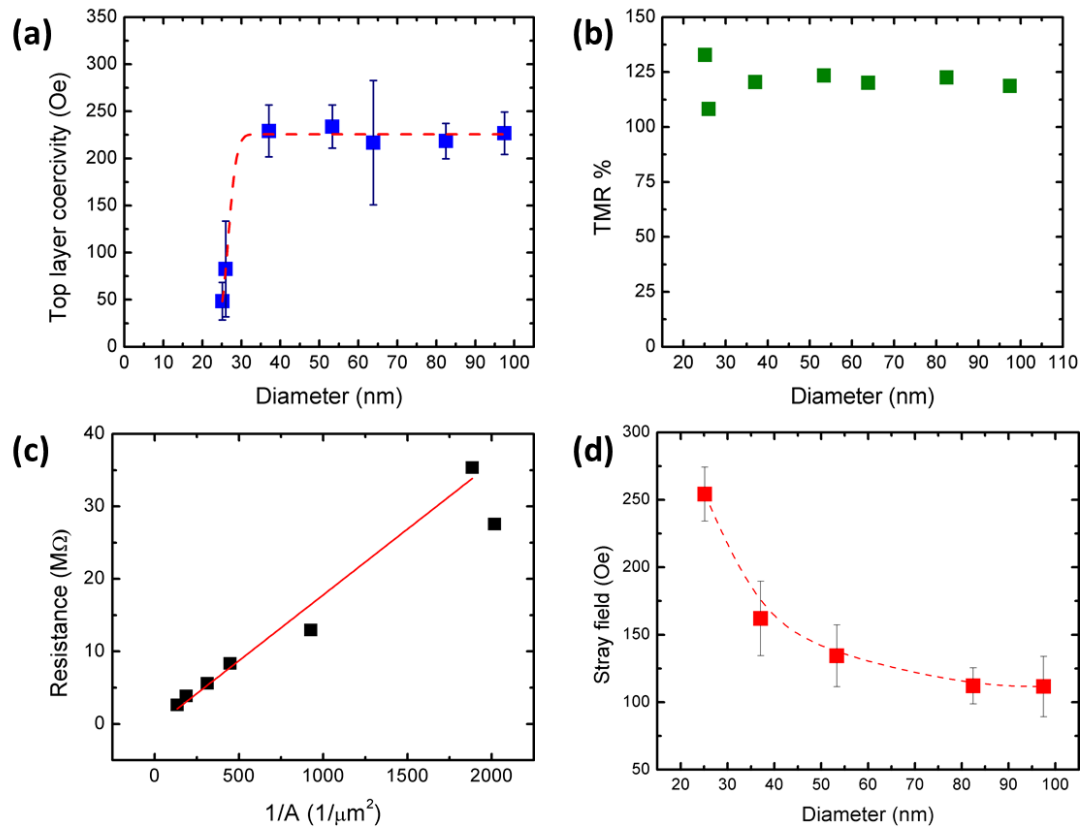


Figure 5.2 (a) top layer coercivity vs size (b) TMR vs. size (c) Resistance vs. inverse of area of the MTJs (d) perpendicular component $H_{ms,z}$ of the stray field.

5.5 Thermal stability analysis of a 55 nm device

Thermal stability analysis was done for a 55 nm device size by measuring RH loops at four different bias values at ± 0.5 V and ± 1 V. About 100 RH loops were measured as described above to obtain switching field distribution corresponding to AP-P and P-AP switches. The switching field distributions were then fitted with Kurkijärvi-Fulton-Dunkelberger equation as described in our previous work [14]

$$\sigma = \left\{ \frac{1}{\tau_0 v} \exp \left[-K_{eff} V \left(1 - \frac{H M_s}{2K_{eff}} \right)^2 \right] \right\} \quad 5.1$$

$$\times \exp \left\{ - \int_0^H \frac{1}{\tau_0 v} \exp \left[\frac{-K_{eff} V}{k_B T} \left(1 - \frac{h M_s}{2K_{eff}} \right)^2 \right] dh \right\}.$$

Here $\tau_0=10^{-9}$ s is the attempt time, $v \sim 250$ Oe/s is the ramp rate of H_{ext} , $M_s \sim 1150$ emu/cm³ [57] is the saturation magnetization of the Co₂₀Fe₆₀B₂₀ free layer, k_B is the Boltzmann constant and $T=300$ K is the temperature. The K_{eff} values as obtained from the fit are shown in Figure 5.3(c). The VCMA coefficient ξ can then be obtained by fitting the K_{eff} vs bias values using equation 2.5. We found $\xi=19$ fJ/Vm for the 55 nm device. The thermal stability value varies linearly with the bias voltage, as shown in Figure 5.3(d). A thermal stability at zero applied bias of about 32.5 obtained by interpolation.

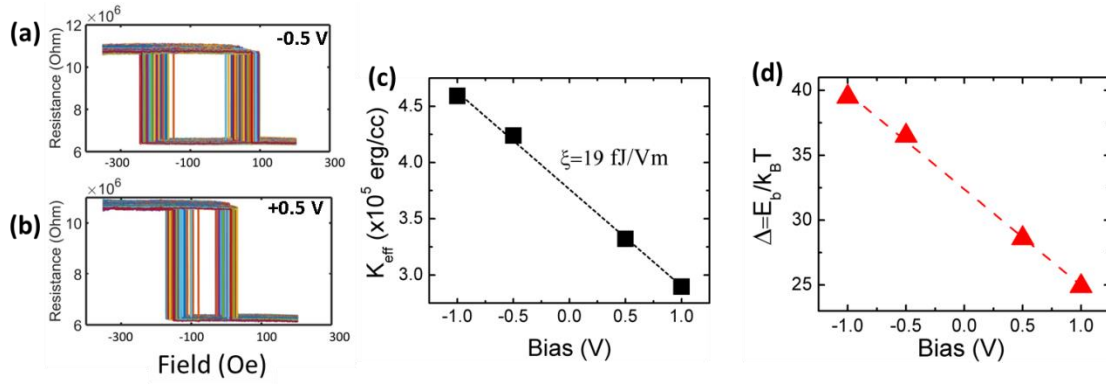


Figure 5.3 RH loops for a 55 nm size device measured 100 times at bias voltage values of (a) -0.5 V and (b) +0.5 V. The VCMA effect causes H_c to change with bias, as can be seen from change in average loop widths between (a) and (b). (c) K_{eff} vs Bias, where a linear fit gives the value of the VCMA coefficient $\xi = 19$ fJ/Vm. (d) Thermal stability factor variation with bias value. The dotted red line is a guide to the eye.

5.6 Field assisted unipolar switching

We attempted unipolar switching with field where the same polarity of current is used to switch the device. Similar unipolar switching schemes have been explored by other research as well with pMTJs [16,60]. To demonstrate this switching, a 55 nm diameter Mo capped pMTJ was initialized using a large external field to set the device in P state. Next an external field opposite in the direction to the magnetization of the top layer was applied such that $H_{\text{sw}}^{P \rightarrow AP} > H_{\text{ext}} > H_{\text{stray}}$. When a positive bias is swept the minor loop coercivity drops, and due to an external field together with thermal activation the MTJ can switch from AP to P. The bias is next set back to zero and the external field turned off. The bias is then swept again to a high positive bias value and a switch from AP to P is again obtained, due to VCMA re-

lowering the energy barrier to allow for field and thermal effects to cause switching. In the AP to P switch, where H_{ext} is zero, the switch is assisted by the stray field from the bottom layer. Note that in both the cases the presence of a magnetic field results in the deterministic nature of switching since VCMA effect by itself is symmetric; VCMA for $V > 0$ lowers the energy barrier for AP to P and P to AP switching equally and it is the field that energetically favors one state over another. In our device we measure field-assisted unipolar switching for a 55 nm device with $H_{\text{ext}} = 100$ Oe and found $J_c^{P \rightarrow AP} = 1.8 \text{ kA/cm}^2$ and $J_c^{AP \rightarrow P} = 85 \text{ kA/cm}^2$ as shown in Figure 5.4(b). There are certain advantages and disadvantages to using this switching scheme. The advantages include (i) switching can be achieved at lower current densities than for STT switching ($\sim 10^6 \text{ A/cm}^2$, also see the discussion on STT switching in Chapter 7), causing minimal damage to barrier during the write process hence increasing endurance, and (ii) there is no change in the current flow direction needed to toggle between P and AP states. The unipolar nature is desired from an integration perspective where circuits may involve diodes for cross channel architectures as access devices. For devices that rely on STT for switching such architectural designs cannot be implemented because they only allow for a single polarity of current to flow. The disadvantages include the need for an external applied magnetic field.

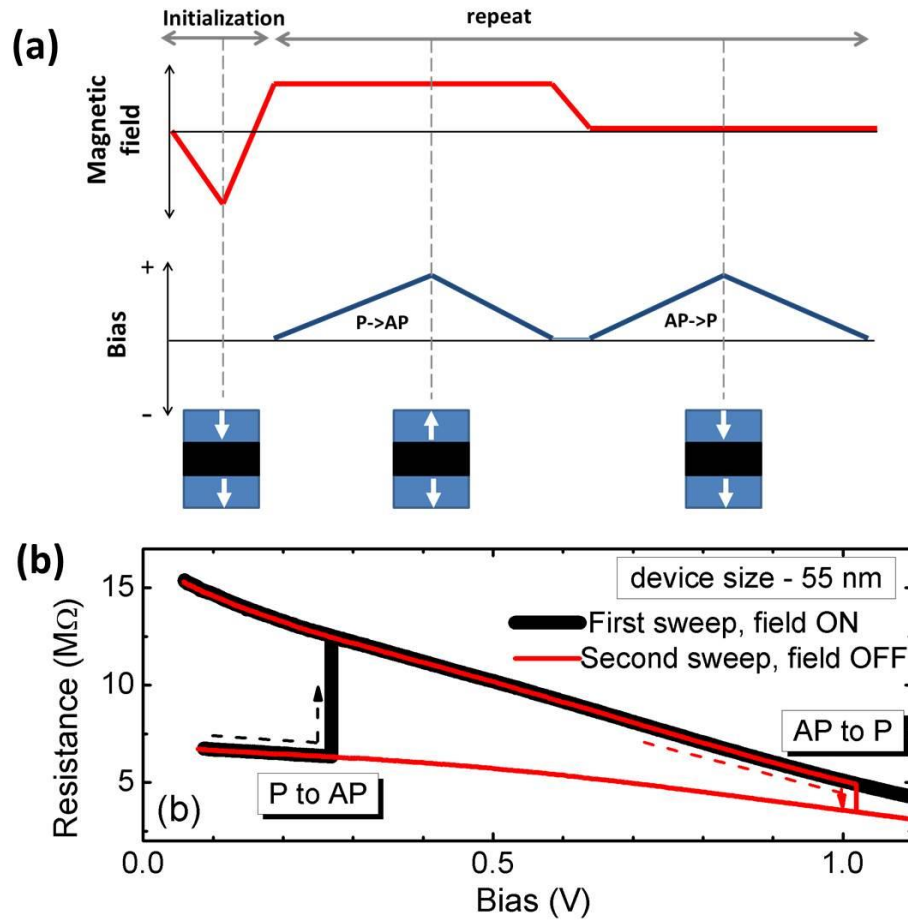


Figure 5.4 Unipolar switching achieved using magnetic field and VCMA effect in a 55 nm pMTJ device.

5.7 Scaling to 25 nm device size

A RH loop for a 25 nm device measured at 100 mV bias voltage is shown in Figure 5.5(a). The device coercivity was found to be 67 Oe and the TMR of the device was ~128%. A shift of 245 Oe was observed in minor RH loops. From the switching field distributions the effective anisotropy was determined to be $K_{\text{eff}} = 1.15 \times 10^6$ ergs/cc

and the thermal stability factor $\Delta=19.8$. The RV loop showing typical switching behavior for a 25 nm device is shown in Figure 5.5 (b). RV loop(s) were obtained with zero applied field by sweeping the bias at a sweep rate of 1.5 V/sec, (i) starting at zero bias in low resistance state, (ii) sweeping to positive bias, and (iii) back to a negative bias, and (iv) returning to zero bias). A switch for P to AP transition was observed at $V_{sw}^{P-AP} = 1.6\text{ V}$ and current density $J_{sw}^{P-AP} = 7.5 \times 10^4\text{ A/cm}^2$, and AP to P at $V_{sw}^{AP-P} = -1\text{ V}$ and $J_{sw}^{AP-P} = 1.73 \times 10^4\text{ A/cm}^2$. Distribution in the switching values was observed in multiple RV loop attempts. We observe both the switches at much lower current densities than for STT. The switch on the positive bias side appears to be a VCMA-assisted STT switch since we observe it consistently for positive bias, and with a relatively narrower switching bias distribution than the switch on the negative bias side. The switch from P to AP on the negative side is likely due to thermal activation since the VCMA would only lead to increases in the coercivity. In some instances of RV loops the AP to P switch was observed at positive bias values, due to wide thermal distribution of the switching bias value which suggests that thermal effects are significant at this size. From the RH loop we do not expect the device to be thermally stable in the AP configuration at zero applied field. Even at this small size and after 400 °C annealing, the device was not superparamagnetic, as would be expected in case of tunnel junctions with Ta capping [57], [61]. With further improvements in stack design and materials growth, higher thermal stabilities should be achievable. The effect of stray field can be mitigated by patterning devices upto the MgO layer to obtain stable bipolar switches with the VCMA effect and/or STT.

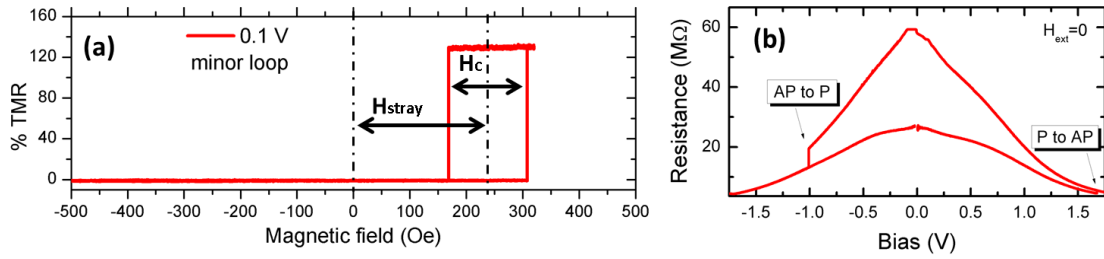


Figure 5.5 (a) minor RH loop for a 25 nm pMTJ device showing 138% TMR. The loop is shifted from the center due to stray field from the bottom reference layer. (b) RV loop showing switches on the positive and negative sides without stray field compensation.

5.8 Summary

In summary we studied the effect of patterning in pMTJ devices with Mo as seed and capping layers. XTEM imaging revealed strong correlation in form of columnar grain structures across the Mo, CoFeB and MgO layers. Although the columnar grains are typically confined to less than 5 nm laterally, these features could have important consequences on the magnetic properties of the patterned devices and can cause device to device variability as the device size decreases. The MTJs were annealed at 400 °C, which makes the study of the magnetic properties particularly relevant from application viewpoint for integration with the present CMOS architecture. The sample with Mo caps showed superior properties such as high TMR, thermal stability as compared to devices with a single tunnel junction but with Ta instead of Mo. The VCMA effect was observed in the pMTJ devices and the effect was used to study the performance under a unipolar switching scheme where an external field much lower than the coercivity of the free layer and a current density much lower than the switching current density for STT are used together to switch the device

between P and AP states. Our results indicate possibility of unipolar switching in these devices with low effective field ($H_{\text{eff}} < 100$ Oe) and low current densities ($J_c \sim 10^3$ A/cm²).

Chapter 6 Low thermal stability pMTJs for stochastic computing

Magnetic tunnel junctions (MTJs) that switch randomly between parallel and antiparallel magnetization have been suggested for use in probabilistic computing; In this chapter, I discuss the design, fabrication, and testing of low thermal stability perpendicular MTJs. MTJs designed for memory applications have thermal stability factors Δ of 60-80, but for probabilistic computing Δ must be small and tunable with a bias voltage. MTJs with Δ that can be varied between 8 and 14 with a voltage will be discussed. The processing speed depends on the fluctuation rate since the output signal must be averaged over many fluctuations. Voltage changes the switching rate indirectly by reducing the perpendicular magnetic anisotropy.

This work also showcases testing of hardwired devices enabling measurement of faster dynamics. The fabrication process flow was adapted from Matt Moneck and was improved upon by Samuel Oberdick for the pMTJ samples. I contributed to CAD designing, e-beam writing, ion milling and rest of the fabrication involving photolithography and reactive ion etching steps were done by Brad Parks, who also worked along with me on the testing and analysis of these devices. Part of this work is published in Parks et al. 2018 [28].

6.1 Introduction

The concept of stochastic computing was developed in the 1960s as an unconventional computing paradigm [62]. Its biggest difference from traditional binary computing is that it operates on stochastic bit streams that encode real values through the probability of occurrences of 1's (or 0's) in the streams, and so the basic principle of stochastic computing is to simply represent analog quantities by the probability that an event will occur. For example, the bit stream "01001" represents the quantity $2/5$ (as the probability of occurrence of 1's). The stochasticity of the bits should be such that the next bit in a sequence cannot be predicted except by some finite probability. As an example for a stream of bits that would not be considered random, if "01001" keeps repeating itself "0100101001..."; then the probability of occurrence of 1's by simplistic definition would still be $2/5$. However this is not random since next bits in sequence can be predicted. Bit streams with such predictable features would render itself unsuitable for most of the stochastic computing applications which requiring non-predictability. NIST has developed a statistical test suite which checks the bit streams against such predictabilities and verifies whether a given test stream can be treated as coming from an apparently *true* random number generator.

The probabilistic way of encoding data allows very simple digital circuits to realize complex arithmetic operations. Two notable examples are (1) the multiplication operation which can be realized by connecting the inputs of an AND gate to telegraphing MTJs and (2) Random Number Generation using a single MTJ (both these examples are also shown in Chapter 2 using STT in in-plane MTJs). Here we analyze the two-level telegraph noise from low thermal stability pMTJs and analyze their performance in such applications. We also analyze how VCMA can be used to tune the thermal stability and consequently the speed of the bit-generation.

The current technology for hardware RNGs is the free running oscillator ring, where phase jitters arising from the changing temperature of the silicon in a series of NOT gates as a source of electronic noise that is thereby used to generate random bits [63]. The rate of bit generation by the ring oscillator is limited by the capacitive lag as the gates of the MOSFETs charge or discharge in series. The output is read at a rate set by an external clock with its inherent uncertainty. The variability of the frequencies in the ring oscillator and clock give rise to a random walk in their relative phase, with the frequency of each component being dependent on the temperature. These circuits are typically hundreds of square microns, consume milliwatts of power, and generate tens to hundreds of megabits per second [64]. Recent experiments in CMOS based RNGs have increased the speed to a few gigabits per second and reduced area by a factor of ten but without significant reduction in power consumption [65].

6.2 Background: Effect of bias on lifetime

The equation governing the thermal stability factor of a pMTJ when acted upon by an electric field was discussed in Section 2.7, I reproduce this here for ease, and relate the lifetime τ to the thermal stability factor due to VCMA effect:

$$\ln\left(\frac{\tau}{\tau_0}\right) = \Delta = \Delta_{V_{bias}=0} - \frac{\xi A}{t_{MgO} k_B T} V_{bias} , \quad 6.1$$

where ξ is the VCMA coefficient, A is the area, V_{bias} is the voltage bias across the MgO based pMTJ, t_{MgO} is the thickness of MgO, k_B is the Boltzmann constant, T is temperature and τ_0 is the attempt time. Here, the lifetime of the MTJ during standby mode when no electric field acts on the device is obtained by setting $V = 0$. Note that

$\Delta(V_{bias} = 0)$ can still be affected by factors such as stray field from the reference layer or due to an external field during standby, the effect of which can be accounted by using equation 2.7 and setting $I=0$. The effect of voltage on the switching time can be seen in Figure 6.1 for a 25 nm pMTJ device operated at two different voltage values.

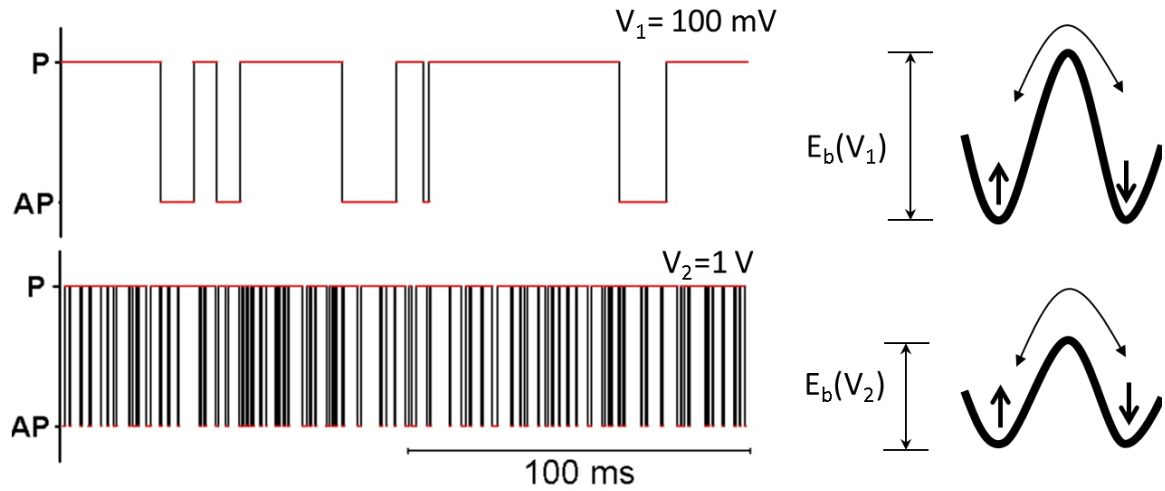


Figure 6.1 VCMA effect causes the switching frequency to change upon application of a voltage by changing the energy barrier between P and AP states.

6.3 Sample preparation and experimental setup

Two different samples are analyzed here in this chapter. The 40:40:20 composition of the CoFeB alloy has a lower anisotropy and consequentially lower thermal stability as compared to the 20:60:20 compositions and the latter is usually preferred for non-volatile memory applications where higher data retention time is needed [66] [67]. The property of interest that differs in the two samples is the thermal stability factor which determines the switching rate in the telegraphing

signal that the MTJs generate. The two samples studied here were both grown by Weigang Wang's group at the University of Arizona:

Sample 1 (CFB262): Here, the bottom reference/tunnel barrier/top free layer has the composition $\text{Co}_{20}\text{Fe}_{60}\text{B}_{20}(0.82\text{nm})/\text{MgO} (\sim 1.2 \text{ nm})/\text{Co}_{20}\text{Fe}_{60}\text{B}_{20}(1.5 \text{ nm})$. Post-deposition the stack was annealed at 400°C for four mins. 25 nm features were defined by e-beam lithography and Ar ion-milling. Conductive atomic force microscopy was used to perform transport measurements on individual devices. Current traces as a function of time were collected with sampling rates between 10 kHz to 1 MHz, to accurately collect the fastest switching events while also recording a statistically significant number of events.

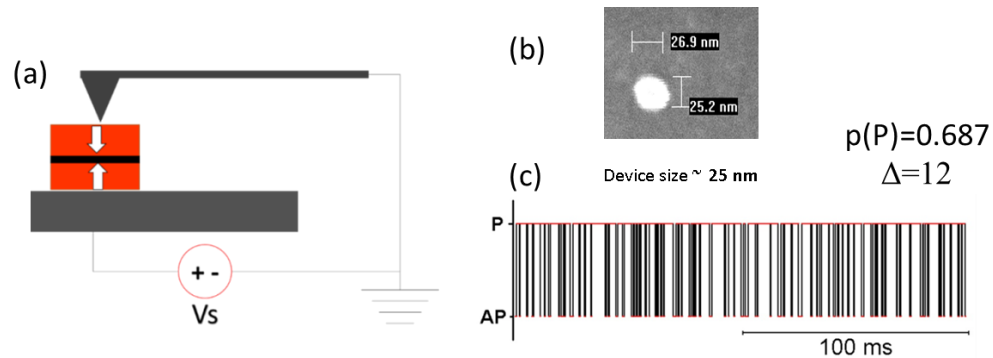
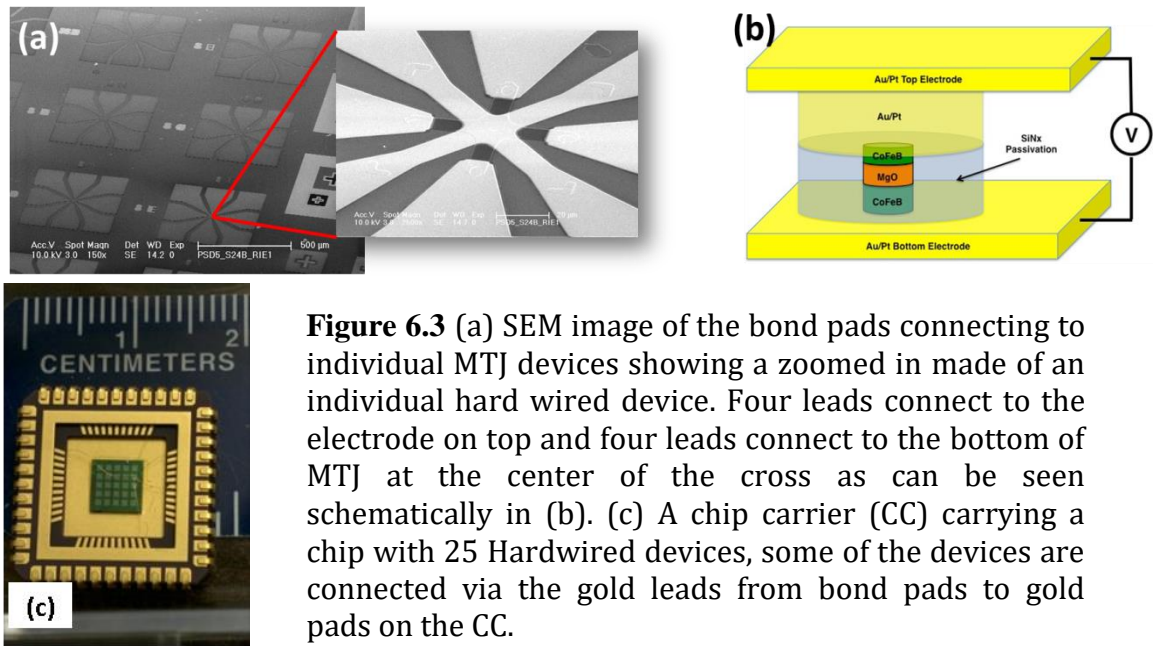


Figure 6.2 (a)CAFM setup (b)SEM of 25 nm device (c) Digitized telegraph noise from 25 nm device showing two states.

Sample 2 (CFB442): Here the bottom reference/tunnel barrier/top free layers had the composition $\text{Co}_{20}\text{Fe}_{60}\text{B}_{20} (0.85 \text{ nm})/\text{MgO} (\sim 1.5 \text{ nm})/\text{Co}_{40}\text{Fe}_{40}\text{B}_{20} (1.5 \text{ nm})$. Post-deposition the stack was annealed at 300°C for ten mins. 60 nm diameter MTJ pillars were defined by electron beam lithography and Ar ion milling and leads, and bond pads were defined by photolithography. The sample was then placed in a chip carrier, and wire

bonded to connect individual devices to a voltage source and ammeter. Bias was applied to the bottom lead while the top was grounded. Thus, for negative bias, electrons flow upward from the fixed reference layer toward the low thermal stability free layer. Current traces as a function of time were collected with sampling rates between 10 kHz to 100 MHz, to accurately collect the fastest switching events while also recording a statistically significant number of events. The measurements were performed using R9 electronics from RHK.



CFB262 was used in initial device testing using CAFM to obtain characteristic RH and RV loops to analyze the effect of VCMA on low thermal stability pMTJ structures. CFB442 was then engineered with the desired alloy composition and fabricated to obtain better performance matrices to showcase the performance of a low thermal stability pMTJs as a true Random Number Generator.

The effect of thermal stability can be seen while sweeping a field to measure RH loops. When a minor RH loop is measured at a sweep rate much smaller than the switching rate $1/\tau$, we usually obtain two switches corresponding to the field induced switching between P and AP configuration of the free layer, whereas if the sweep rate is comparable or greater than the switching rate, then we can expect to see multiple switches in the minor RH loop due to the thermal fluctuations. We measured RH loops with a sweep rate of 250 Oe/s. For CFB442 telegraphing was observed at a 60 nm device size in the RH loops (Figure 6.4 (a)) whereas for the same device size CFB262 was found to be stable with relatively high coercivity ~ 312 Oe (Figure 6.4 (b)). For CFB262 telegraphing was seen at a reduced device size of 25 nm (Figure 6.4 (c)) due to reduction in thermal stability with size. The loops are shifted from $H=0$ depending on the strength of the stray field with size and alloy as discussed in Chapter 4. The probability p of a device being in the P or AP state can be tuned between zero and one by changing the magnetic field around this stray field value and is shown as a red curve in (a) and (c).

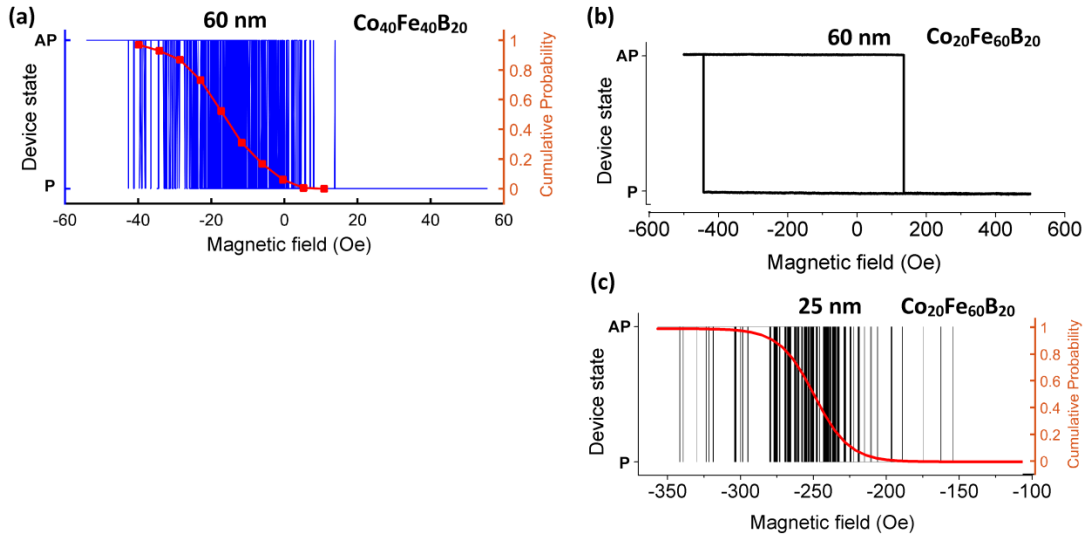


Figure 6.4 Minor RH loops (digitized): (a) A 60 nm CFB442 showing telegraphing, (b) 60 nm showing stable switches, (c) a 25 nm CFB262 showing telegraphing. The

red curve in (a) and (c) is a sigmoidal fit to show tunability between P and AP with the field. Loops are shifted due to the stray field from the reference layer. Sweep rate ranged from 250-1500 mV/sec.

Time traces were collected to study the effect of bias on the switching rate. All traces exhibit two well-defined current levels corresponding to parallel (P) and antiparallel (AP) states. For a random telegraph signal, the transitions are assumed to be uncorrelated, and from each trace, the time durations in the upper (τ_P) and lower states (τ_{AP}) before switching were extracted. Switching in a random telegraph signal is a Poisson process; hence the distribution of lifetimes was observed to be exponential. Fitting the distribution thus yields the characteristic lifetimes of the two states of the Arrhenius-Neél-Brown model. Furthermore, the autocorrelation functions of the telegraph noise traces were investigated to verify that the distribution is exponential.

The low bias TMR at 100 mV for 25 nm CFB262 devices was 110%, and the current density was 600 A/cm². With such low current density, we can ignore the effects due to STT. For 60 nm CFB 35% TMR was observed at -0.4 V; below this bias value the signal to noise ratio was too high for the electronics to differentiate between the high and the low levels.

An external field roughly equal to the stray field but opposite in magnitude was applied to remove the bias of the device in P or AP state (such that the probability $p(P) \sim 0.5$). As shown in Figure 6.1 the energy barrier and hence the characteristic lifetime can be controlled using bias voltage, due to the VCMA effect.

In case of the 25 nm CFB262 MTJ, the thermal stability factor could be varied from 8 to 14 using bias voltage within the positive and negative bounds of voltage set by

the breakdown value of 2.3 V. Whereas, for the 60 nm CFB 442 MTJ the thermal stability is tunable between 14.7 to 9.5 for bias from -1.3 V to -0.8 V. The lifetime of the high and low current states as a function of bias is shown in Figure 6.5. The time the device spends in each state was found to be a nonlinear function of bias. Similar reports on nonlinear anisotropy change with bias voltage have been made by Xiang et al. 2017 [68], where the effect was attributed to the inherent electronic structure in the Fe/MgO interface at the Fe/MgO interface. The trend is linear and steep for large negative bias, but relatively unchanging for bias values more positive than about -800 mV for CFB442 and -400 mV for CFB262. For negative bias, if a linear variation is assumed the slope gives the values of the VCMA coefficient of 12.2 fJ/Vm and 21 fJ/Vm for the CFB442 and CFB262 respectively. The CFB442 device telegraphs faster than the 25 nm CFB262 MTJs and in the maximum efficiency case of -0.4 V for the former, the device operates at a power of 27 nW and an average speed of 45 kHz, and thus the device produces random bits at an energy cost of 600 fJ per bit.

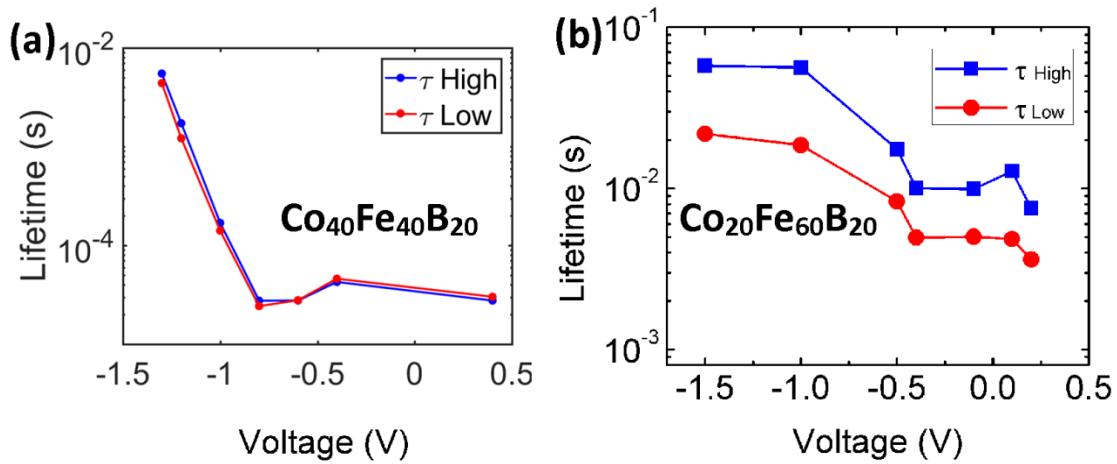


Figure 6.5 Lifetime of the high and low current states shows a non-linear trend for (a) 60 nm CFB442 and (b) 25 nm CFB 262.

6.4 MTJ Performance under multiplication operation using AND gate

Multiplication of two analog numbers is both computationally intensive and architecturally involved, whereas in stochastic computing an AND gate can be used to simply multiply two numbers, where the numbers are encoded as a probability of input and output signals being in a particular state. If the probability of input A being in P state is x and input B being in P state is also x , then the output $A \cap B = C$ being in P state is x^2 . As a proof of principle, we build an artificial AND gate with experimentally measured telegraph noise from a 25 nm CFB262 device used as an input as schematically shown in Figure 6.6(a). To demonstrate the probabilistic nature of the telegraphing signal, we begin by thresholding the current vs. time traces to convert the experimentally measured current levels corresponding to P and AP to 0's and 1's, respectively. The digitized signals were then fed into the two terminals of an AND gate, and the output signal was analyzed. The error in output was observed to be small and could be minimized by increasing the time duration of the two input signals in Figure 6.6(b). pMTJs with lower energy barriers $< 8kT$ could further reduce the error and input time required for faster and accurate computations. The true random nature of telegraph signals from pMTJs with tunable energy barriers opens up new avenues for stochastic computing.

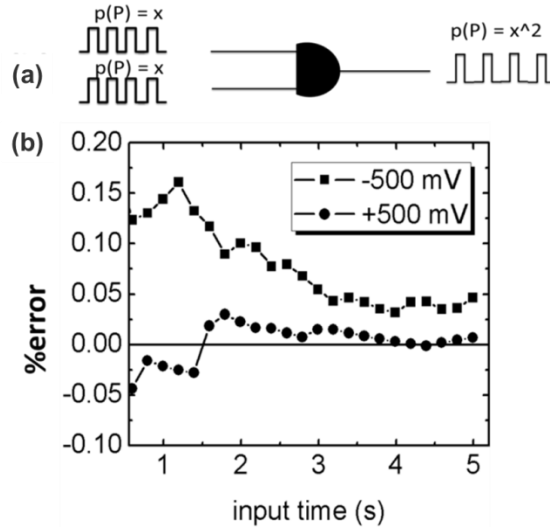


Figure 6.6 (a) Schematic of an AND gate which multiplies the probabilities of two Random Telegraph Noise input signals being in P state with probability= x . (b) percentage error which is small and decreases with increase in the input signal duration.

6.5 MTJs as RNG – NIST STS Analysis

To demonstrate the true random nature of telegraph signal originating from a low thermal stability pMTJ, we performed tests for randomness provided by the NIST Statistical Test Suite [69]. The NIST STS suite tests the randomness of an input data stream consisting of 0's and 1's for factors tabulated in the left column of Table 1 and computes a p-value corresponding to each test. If a p-value > 0.01 (significance level) is found for a particular test, then the input bit stream is characterized as random as far as that test is concerned, otherwise it is not considered random. For a RNG to qualify as a true RNG, a bit stream produced by it should pass through all the NIST STS tests. To convert our data to an acceptable input format for the NIST STS

analysis, we first digitize the telegraph signal data; high resistance state was digitized as '1' and low resistance state as '0'. The hopping process between P and AP state follows Poisson statistics and hence the distribution of time duration between switching events is exponential. From the fit of the exponential distribution average lifetimes τ_P and τ_{AP} corresponding to average lifetime in parallel and antiparallel states is obtained (see supplementary info). The data was acquired at a high acquisition frequency of 100 MHz for 500 ms duration to get a statistically significant number of switches. However, for the NIST STS analysis, the sampling was performed on the acquired dataset at intervals of $\tau = (\tau_P^{-1} + \tau_{AP}^{-1})^{-1}$. A number of data bits that we obtain after this type of sampling is shown in Table 6.1 for different bias values. XOR whitening process was then applied to get rid of any bias for the device being in state 0 (P) or 1 (AP) state. This bias in the probability of the device being in P or AP state originates from the fact that the stray field from the bottom layer can favor P state over AP state. This bias can be large if the bottom layer is patterned [43]. However, here the effect is small since the reference layer was not patterned through. In an actual device, this effect can be mitigated all together, for example, by having a SAF structure with the reference layer to cancel the stray field. The effect of different XOR whitening process is shown in Table 6.1, for our data set XOR2 whitening suffices to remove the bias and XOR4, and XOR8 whitening gives an only a slight improvement over XOR2 whitening.

Table 6.1 The NIST STS tests for randomness were applied to the time-resolved resistance measurements with different degrees of whitening. Bold-faced p-values indicate a passed test.

	Test	Frequency	Block Frequency	Cumulative Sums Forward	Cumulative Sums Reverse	Runs	Longest Run	Approximate Entropy	Serial	FFT
Bias	Failure Criteria	Total number of 0's and 1's mismatch	Number of 0's and 1's mismatch within a subset	Running sum deviates too far from half the length	Same as previous, but in reverse direction	Too many sequences of consecutive bits of one type.	Too many consecutive bits of one type	Bit sequence too unlikely	Multiple low entropy sequences in a row	Periodicity in bit stream
-800 mV	<i>XOR2</i>	0.597	0.03	0.877	0.419	0	0	0	0	0.544
	<i>XOR4</i>	0.984	0.328	0.95	0.939	0.889	0.846	0.801	0.573	0.745
-400 mV	<i>XOR2</i>	0.656	0	0.705	0.345	0	0	0	0	0
	<i>XOR4</i>	0.242	0.861	0.379	0.194	0	0.01	0	0	0.876
	<i>XOR8</i>	0.649	0.344	0.798	0.862	0.982	0.773	0.8	0.653	0.032

6.6 Conclusion

CoFeB-MgO based perpendicular magnetic tunnel junctions have switching time <10 ns and a tunable energy barrier where the retention time can be tuned to be as low as 100 ns, making them particularly interesting candidates for stochastic computing applications. The figures of merits for low thermal stability pMTJ as RNGs are the generation speed (high), energy consumption (low), and ease of integration with CMOS technology.

Chapter 7 Electrical control of magnetization via STT

Previously (In Chapter 6) on low thermal stability pMTJs the control over the switching speed was achieved through VCMA. Here, we focus the attention on low thermal stability in-plane MTJs with STT. In this chapter I first analyze the control over time averaged magnetization using a magnetic field and then show that it can also be controlled with a bias voltage using STT. With bias voltage alone it is possible to tune through a full sigmoidal curve in for time-averaged magnetization $\langle m \rangle_t$. The usefulness of such telegraph signals is shown by two examples. In the first, the device is operated at critical current values for STT, and the NIST Statistical Test Suite (STS) analysis was performed [69] on the telegraph signal generated by the MTJ. Second, using probabilistic computing logic, I demonstrate an algebraic operation of multiplication using an *AND* logic gate with telegraph signals measured at two different voltage values.

7.1 Introduction

A low thermal stability magnetic tunnel junction (MTJ) fluctuates between parallel and anti-parallel orientations of the free magnetic layer with respect to the fixed layer due to the exchange of thermal energy with the surroundings [70,71]. For memory applications a data retention time > 10 years is desired, which corresponds to a thermal stability factor $\Delta = E_b/k_bT > 45$, where E_b is the energy barrier and k_bT is the thermal energy. $\Delta \sim 1$ -10 corresponds to data retention time of nanoseconds to

microseconds. Low thermal stability MTJs are of growing interest for a wide range of applications such as temperature sensors [72], probabilistic computing [25], random number generators (RNGs) [73] and neuromorphic computing [30]. While a low thermal stability MTJ has potential to provide fast oscillations between the P and AP states, tunability of the time-averaged magnetization $\langle m \rangle_t$ is needed for stochastic computing applications. Here a scaled $\langle m \rangle_t$ varying between +1 and -1 is read as a probability term varying between 0 and 1 (or vice versa) for computations. Recently, simulations have shown that such low thermal stability devices where the magnetization can be tuned continually can be used for probabilistic computing applications or for constructing a restricted Boltzmann machine for pattern recognition [23,25]. Such control over $\langle m \rangle_t$ can be achieved with an external field, as has been shown in our previous work with perpendicular MTJs [14], [22], but for application purposes voltage or current control is preferable [74]. Stochastic precessional switching of magnetization has been proposed where a voltage can be used for random number generation (RNG) [24,26]; however, no experimental demonstration has yet been reported. For applications where coherence in magnetic fluctuations is needed instead of stochasticity, it has been shown that a small alternating current with an amplitude less than the critical current density for STT switching can be used in low thermal stability MTJs [75]. *High* thermal stability MTJs have also been shown to be useful for RNG based on stochastic switching of a device when operated at precisely the critical current density for a spin transfer torque (STT) effect [73], [76]. However such processes are slow because they rely on a single bit generation per voltage sweep. Moreover, a reset pulse is required after each bit generation limiting performance in terms of speed and energy. Here we control the time-averaged magnetization achieved using *low* thermal stability MTJs by STT.

7.2 Patterning and experimental setup

As shown in Figure 1, the magnetic tunnel junction film stack is composed of a Ta(50 nm)/ PtMn(20 nm)/CoFe(2 nm)/Ru(0.8 nm)/CoFe(3 nm)/MgO(1 nm)/CoFeB(2.5 nm)/Ta(10 nm)/Pt(5 nm). The stack was supplied by Nick Rizzo from Everspin Technologies. It was field annealed to set the axis of the antiferromagnetic PtMn layer used to pin the synthetic antiferromagnetic reference layer. We patterned this sample using e-beam lithography and Ar ion milling, using a secondary ion mass spectrometry detector we stop at the MgO layer.

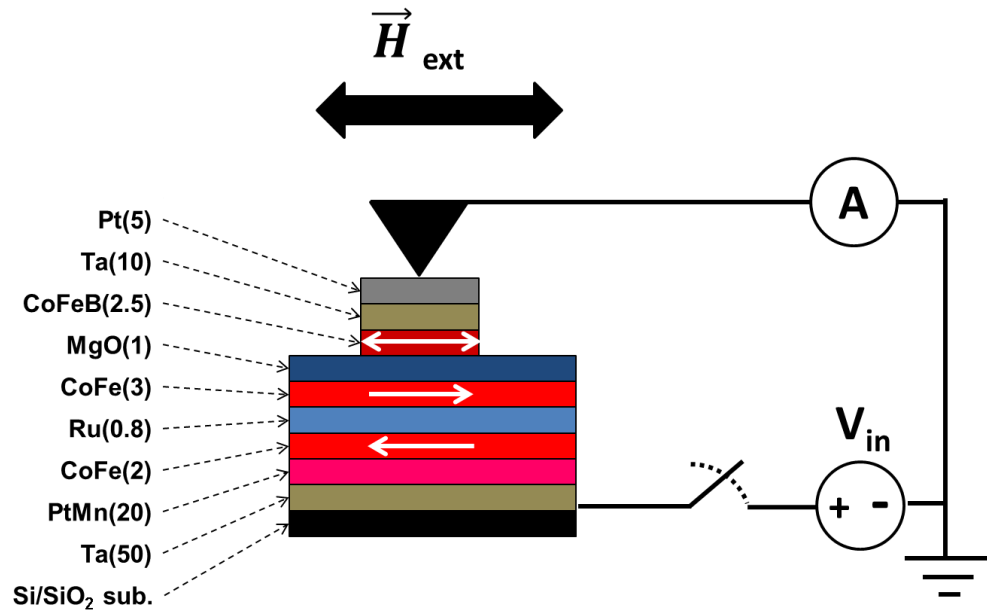


Figure 7.1 Schematic of C-AFM setup used for electrical measurements of MTJs. The devices are patterned till the MgO, and the reference layer CoFe is coupled to CoFe/Ru/PtMn underneath in a synthetic antiferromagnetic arrangement. The numbers in brackets are thickness values in nm. Figure taken from [77].

All transport measurements were done using a conductive atomic force microscope (C-AFM), as shown schematically in Figure 7.1. Further details about the

instrument and measurement procedure can be found elsewhere [78]. A sharp AFM tip with 20 nm of conductive Pt coating was used to make electrical contact directly with the top of individual devices. In all measurements, the tip remains grounded, and the bias is applied at the bottom of the sample. The sample was initialized with an external in-plane field of 4000 Oe using a permanent magnet to set the orientation of the fixed layer. An in-plane magnetic field H_{ext} of up to 500 Oe was applied using a pair of electromagnets aligned along the easy axis of the ellipses. A sweep rate of 150 Oe/sec was used to measure the resistance versus magnetic field loops $R(H)$. A sweep rate of 500 mV/sec was used to measure the resistance versus bias voltage loops $R(V)$. For resistance versus time traces $R(t)$, an acquisition rate of 1 MHz was used.

7.3 Imaging and RH measurements of ellipses

Post patterning, SEM imaging was performed to check the integrity of the patterned devices. The devices in the form of ellipses were oriented at four different angles; 0° , 45° , 90° and 135° (up to down in Figure 7.2 (a)) between the major axis and the magnetization of the fixed layer. The Néel dipolar orange-peel effect [79] between the top CoFeB layer and the CoFe layer directly below MgO causes the midpoint of the loop to shift to the positive field due to ferromagnetic coupling between the two layers [80,81]. The elliptical patterns with 0° orientation angle correspond to easy axes of the free layer being directed along the magnetization direction of the fixed layer. In Figure 7.2 (a) the size of the ellipses increases left to right. C-AFM was used to check the topography of all the ellipses as shown in Figure 7.2 (b) and conductivity as shown Figure 7.2 (c) measured at 100 mV. RH loops were measured for the different ellipses as shown in the matrix of Figure 7.2 (d). In each loop, the inset shows the relative orientations of the ellipses similar to Figure 7.2 (a). Sharp

switching was seen when the ellipses were oriented along the magnetization of the fixed layer because the easy axis is directed along the coupling direction. At 90° the shape anisotropy competes with the coupling field and results in fluctuation seen in the RH loops. For 45° and 135° orientations the shape anisotropy causes a gradual change in magnetization with the applied magnetic field when the external field cancels the dipolar field we see a sharp switch in the RH loop.

In the next sections, we will focus solely on the magnetization dynamics for 20×60 nm ellipses.

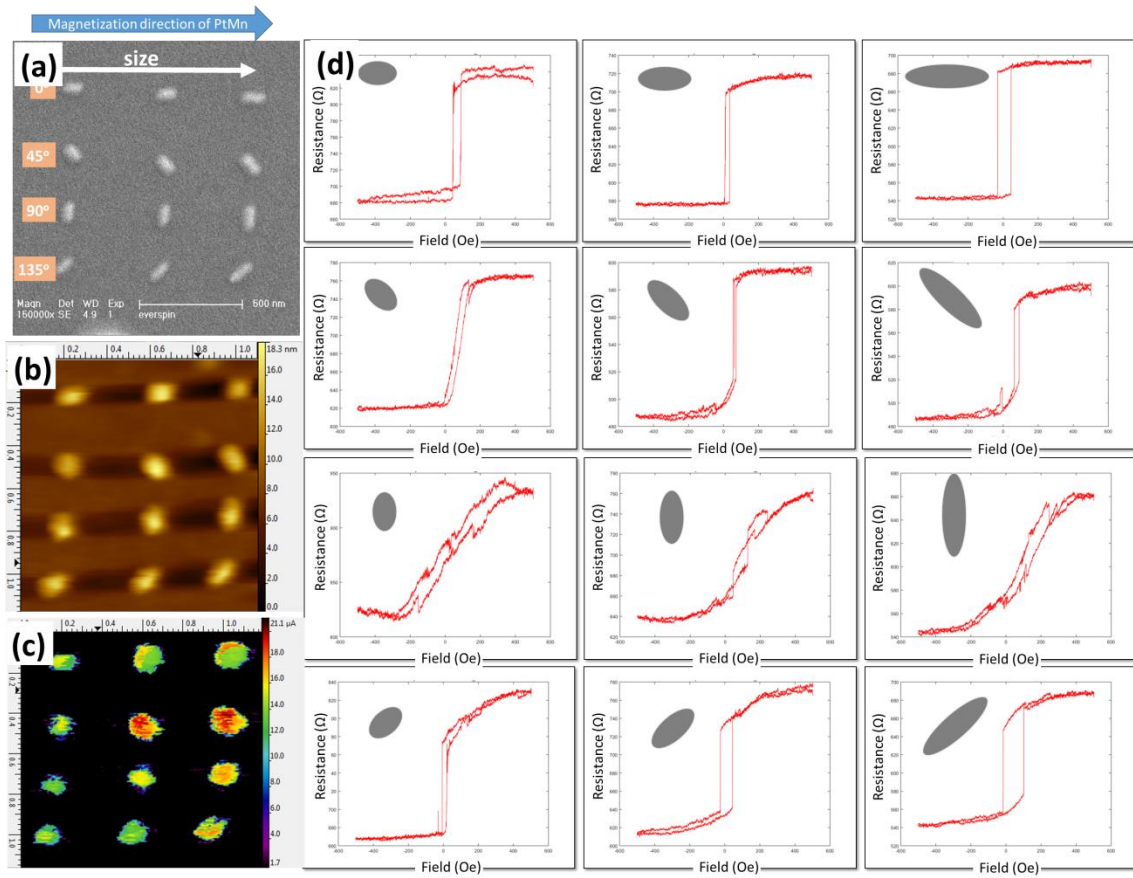


Figure 7.2 (a) SEM images of patterned ellipses (b) AFM topography (c) current map at 100 mV bias voltage and (d) RH loops for ellipses with different orientation across rows

and different sizes across columns (relative size and orientation shown in inset similar to (a)).

Figure 7.3(a) shows the tunnel magnetoresistance (TMR) on a 20×60 nm ellipse with the major axis along the magnetization direction of the pinned SAF reference layer. We observed that at $H_{\text{ext}} = 0$ the MTJ is stable in the P configuration due to this coupling, and between ~ 10 -20 Oe it fluctuates between the P and AP configurations as the external field is swept. When the field is held constant within this range, the TMR fluctuates as a function of time and displays telegraphing behavior (Figure 7.3 (b)).

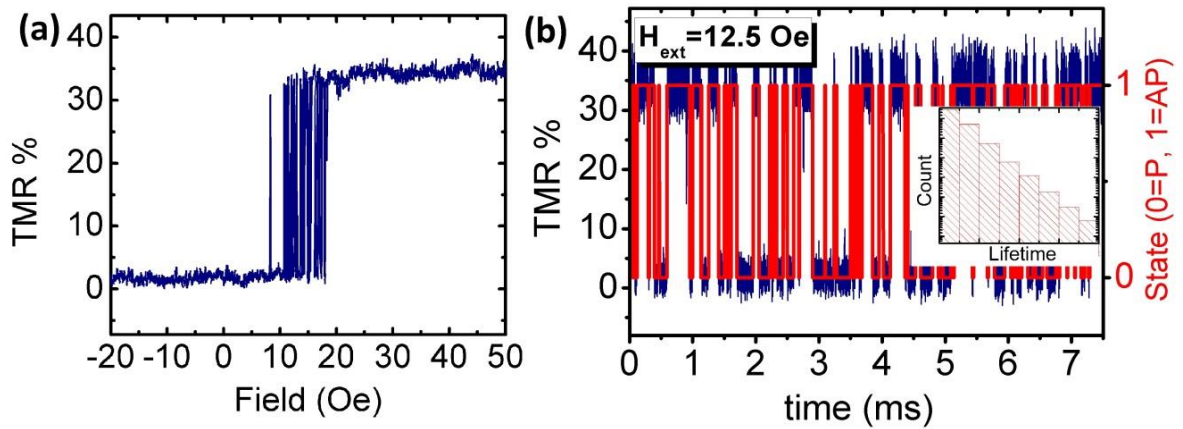


Figure 7.3 (a) The resistance vs. magnetic field loop taken at 10 mV bias voltage shows telegraphing between two states, which can also be observed as a function of time in (b). At $H_{\text{ext}} = 12.5$ Oe the external field cancels the dipolar field and the device telegraphs between the P and AP states (solid red curve) with equal lifetimes and the inset shows the number of counts vs. lifetimes in a semilog plot for the same trace. Figure taken from [77].

7.4 Control over time averaged magnetization using STT

The hopping process between P and AP states follows Poisson statistics, and hence the distribution of time duration between switching events is exponential

(see inset of Figure 7.3(b). From fits of the exponential distributions, the characteristic lifetimes in the parallel (τ_P) and antiparallel (τ_{AP}) states are obtained. At $H_{\text{ext}}=12.5$ Oe the two lifetimes are equal (Figure 7.3 (b)) because H_{ext} compensates the dipolar coupling field H_{dc} and hence the net field $H=H_{\text{dc}}+H_{\text{ext}}$ is zero. This yields characteristic lifetimes $\tau_P = \tau_{AP} = 0.156$ ms. Using a generalized Néel-Brown model [82] for this condition:

$$\tau_P = \tau_0 \exp\left(\Delta_{\text{in-plane}}(1 - I/I_c)\right). \quad 7.1$$

Here the attempt time $\tau_0 = 1$ ns, I is the current through the MTJ and I_c is the critical switching current for STT, for small current through the MTJ such that $I/I_c \ll 1$, we obtain the in-plane thermal stability factor $\Delta_{\text{in-plane}} = 11.9$.

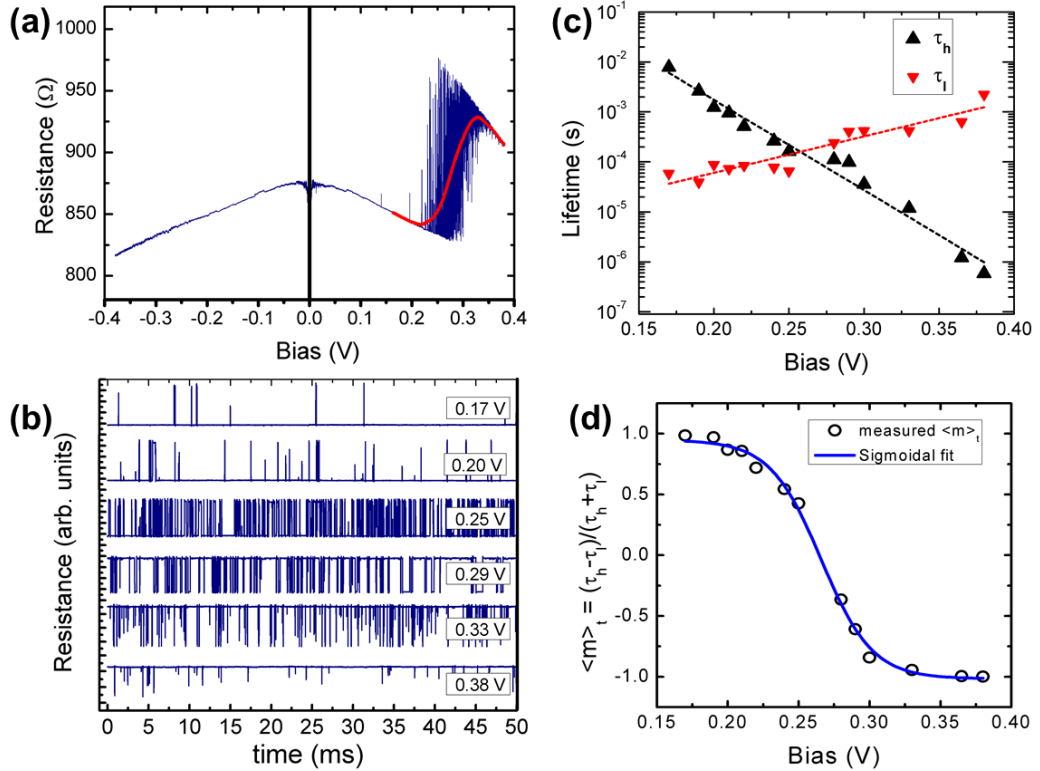


Figure 7.4 (a) R(V) loop for a 20 nm x 60 nm ellipse measured at $H_{\text{ext}} = 0$ showing telegraphing signal at positive bias. The red curve is guide to the eye for the telegraphing region. (b) Resistance vs. time traces measured at different bias values (c) average lifetimes in P and AP states and (d) time-averaged magnetization (circles) with the sigmoidal fit (blue curve) versus bias. Figure taken from [77].

The corresponding R(V) loop for the same device is shown in Figure 7.4(a). Several switching events between P and AP state can be seen near the critical switching current. Here, we observe a competition between the fixed strength of the Néel dipolar orange-peel coupling field favoring the P state and the variable STT effect favoring the AP state. Note that the negative side of the R(V) loop corresponds to a stable region where both these effects stabilize the P state of the device, hence no switching or telegraph noise is seen on the negative side of the loop.

We analyze the effect of STT current on the time-averaged magnetization of the recording layer, which we define as:

$$\langle m \rangle_t = \frac{\tau_P - \tau_{AP}}{\tau_P + \tau_{AP}}. \quad 7.2$$

With this definition when the device dwells mostly in the P state, so that $\tau_P \gg \tau_{AP}$, $\langle m \rangle_t$ approaches +1, when the device dwells mostly in AP state, $\tau_P \ll \tau_{AP}$, it approaches -1, and when $\tau_P = \tau_{AP}$ $\langle m \rangle_t = 0$. We analyze the effect of voltage bias to tune $\langle m \rangle_t$. Using the lifetimes from Figure 7.4(c), we calculate time-averaged magnetization $\langle m \rangle_t$ and show that it is completely tunable with either a current or voltage bias. The results are shown in the sigmoidal curve of Figure 7.4(d). The observed effect of change in lifetimes at high current densities is evidence that this is due to STT and not voltage controlled magnetic anisotropy (VCMA). Our previous work with low thermal stability pMTJs [28] has shown that the VCMA effect does not change the relative ratio of the lifetimes corresponding to the P and AP states.

For in-plane MTJs, $\Delta_{\text{in-plane}}$ and the effective anisotropy field $H_k^{\text{in-plane}}$ terms are related by the following expression:

$$\Delta_{in-plane} = \frac{M_s H_k^{in-plane} V}{2k_b T}, \quad 7.3$$

where the saturation magnetization $M_s = 800 \text{ emu/cc}$, V is the volume of the free layer $V = 300\pi \text{ nm}^2$, k_b is the Boltzmann constant and temperature $T = 300 \text{ K}$. This gives $\mu_0 H_k^{in-plane} = 261 \text{ Oe}$. To switch a device with this anisotropy field using STT, the critical switching current can be estimated using:

$$I_{c0}^{in-plane} = \frac{2\alpha e \mu_0}{P \hbar} M_s V (H + H_k^{in-plane} + 2\pi M_s), \quad 7.4$$

where the spin polarization factor $P = 0.35$, the damping constant $\alpha = 0.01$, \hbar is the reduced Planck's constant and $H = H_{ext} + H_{dc}$ is the magnetic field on the top layer. In this experiment we keep $H_{ext} = 0$ and $H_{dc} = 12.5 \text{ Oe}$, as obtained above, which gives $I_{c0}^{in-plane} = 1.03 \text{ mA}$. For the telegraphing signal, we can take the measurement time to be $\sim 10 \mu\text{s}$ which we typically observe in our measurements as the average lifetime $\tau_{av} = (\tau_P^{-1} + \tau_{AP}^{-1})^{-1}$, for a telegraphing device. We then evaluate the expected critical current using Equation 7.4 to be 0.18 mA , which agrees with the experimentally observed current value for our device under test in bistable state at an applied voltage of 0.26 V . The resultant current density through the device is thus $1.9 \times 10^7 \text{ A/cm}^2$ for the P to AP transition, which is typical of STT. In our experiments the bistable state was, achieved using a constant bias source. Since the lifetimes in P and AP states are dependent on the current density this effect could also, be achieved using a constant current source. The slope asymmetry in Figure 7.4(c) can be explained by the changing effective energy barrier due to the spin current in presence of a fixed field, $H = H_{dc}$ in our case. For a finite H Equation 7.1 becomes [71], [21]:

$$\ln\left(\frac{\tau_{P,AP}}{\tau_0}\right) = \frac{E_0}{k_b T} \left(1 \pm \frac{H}{H_k^{in-plane}}\right)^2 \left(1 \mp \frac{I}{I_c}\right), \quad 7.5$$

where E_0 is the energy barrier at $H = 0$. It can be seen through Equation 7.5 that the energy barrier is non-degenerate for P to AP and AP to P transition in the presence of a field and current which explains the slope asymmetry that we observe in Figure 7.4(d). Longer time traces were recorded to analyze the efficiency of this in-plane MTJ as a true random number generator, where the telegraph noise was generated by varying the voltage. In our experiments, we see that at $V=260$ mV the device spends approximately equal time in the P and AP states. The signal collected at this bias was tested for randomness using NIST STS suite [69].

7.5 Performance as a *true* Random number generator

To prepare the data, we first digitized the high resistance state as “1” and low resistance state as “0”. We then resampled the data at the frequency $1/\tau_{av}$ and perform the XOR operations on the measured signal to increase the Shannon entropy [83]. XOR operations are critical because otherwise a very precise control over the voltage would be needed to tune the MTJ to the narrow range where 50:50 distribution of 0’s and 1’s is expected due to STT. 30 kilobits of data generated by the MTJ in 0.5 sec were tested and the significance p values are shown in Error! eference source not found.. After XOR4 and XOR8 operations the data set passes all the tests shown in the right two column of Table 7.1. We see that MTJ device generating the telegraph noise around the critical voltage value for an STT effect acts as a *true* random number generator.

Table 7.1 P-values for randomness for different NIST STS tests vs XOR operations performed on a telegraph signal generated by MTJ operating near the critical current I_c . Non-zero values (in green) show passed tests.

	Frequency	Block Frequency	Cumulative Sums FWD	Cumulative Sums REV	Runs	Longest Run	Approx Entropy	Serial	Serial	FFT
XOR2	0.33264	0.015168	0.283732	0.23629	0	0	0	0	0.15443	0
XOR4	0.45241	0.02494	0.614117	0.499825	0.018344	0.711165	0.323351	0.89605	0.78815	0.163239
XOR8	0.54212	0.334559	0.433366	0.945763	0.794912	0.627293	0.104374	0.7483	0.85831	0.583247

7.6 Performance in Logical AND Gate

We applied the voltage tunability of the telegraph noise to a stochastic computation process; multiplication of two numbers using a single logical AND gate. For this, we input two telegraph signals A and B generated by two different MTJs at two different bias values. According to equation 7.5, this leads to different lifetime corresponding to P and AP states. Signals A and B were generated at $V_A = 240$ mV and $V_B = 280$ mV, respectively. This resulted in $\{\tau_P, \tau_{AP}\}$ values of $\{330 \mu\text{s}, 87 \mu\text{s}\}$ and $\{106 \mu\text{s}, 187 \mu\text{s}\}$ for each signal, respectively. This translates to the probability of signal being in state $m=+1$, given bias $V=V_x$ across the MTJ, as $P_x(m=1|V_x) = \tau_{AP} / (\tau_P + \tau_{AP})$, where $X=\{A,B\}$. We see that the output of the logical AND gate being in state “1” is then, theoretically, just the multiplication of the two numbers that is P_AP_B . We compare this theoretical value with the actual output signal and see that the error sharply drops to below 0.5% in less than 200 ms as shown in Figure 7.5. Such a computation can be made faster with low thermal stability values and more

accurate with faster acquisition rates to resolve intermediate fluctuations between P and AP states. Interestingly, the fluctuations are uncorrelated because the thermal fluctuations leading to telegraphing are themselves uncorrelated and hence parallel MTJ processes can be implemented for both simple and complex operations utilizing this inherent and uncorrelated stochasticity of individual devices.

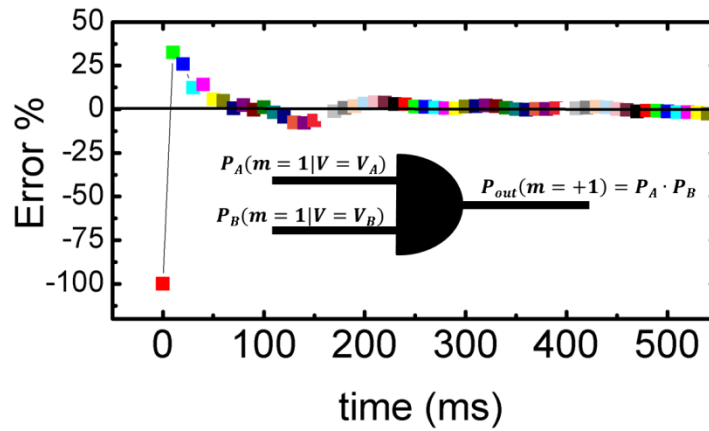


Figure 7.5 Error minimization with time for multiplication of two number encoded as the probability of signal being in state $m=1$. Here two inputs come from two different MTJs operating at two different bias voltages, V_A and V_B . Figure taken from [77].

7.7 Tuning telegraphing STT region with an external field

The value of voltage or current density around which the device telegraphs can be completely tuned by application of an external field. The critical current density of switching and hence the telegraphing region can be changed with an external field according to equation 7.4. This effect can be used to obtain telegraph signal from a device at low bias or current density values. In Figure 7.6 we can see that for a positive net field device telegraphs for positive bias and a net negative

field the device telegraphs at a negative voltage bias. One can also tune the field to obtain the telegraph noise around zero voltage bias (not shown here) to obtain a signal at low current densities. However, note that this comes at the cost of having an external applied magnetic field. This direction of research can be further pursued to obtain telegraph noise at desired current density values for stochastic computing applications where the operation of the device at certain desired voltage bias and current value is desired.

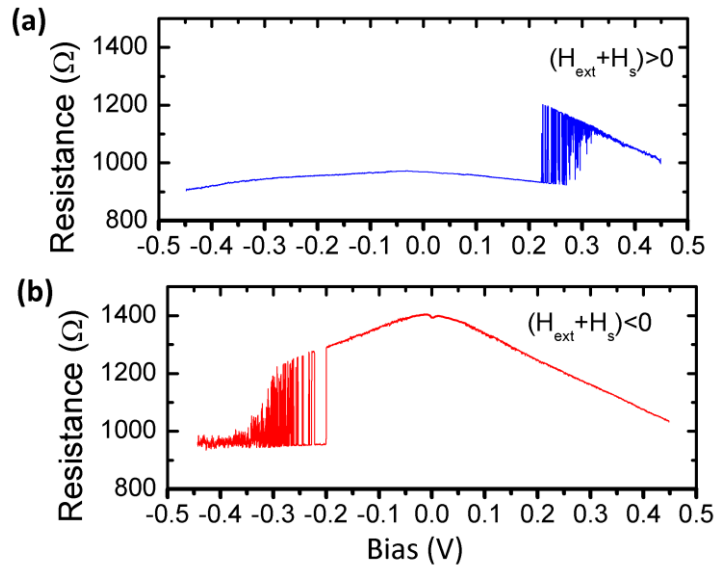


Figure 7.6 (a) Telegraph noise observed around 0.25 V when the external field H_{ext} and stray field H_s add up to a positive value and (b) at -0.25 when they add up to a negative value.

7.8 Summary and Future

These prototype demonstrations show that low thermal stability MTJs have the necessary characteristics for future computing applications that require

stochasticity and true randomness, including tunability, speed, and room temperature voltage-controlled operation. The STT control of $\langle m \rangle_t$ scheme shown in this paper is also advantageous because the sign of the bias need not be changed and thus the voltage or current control of $\langle m \rangle_t$ is unipolar in nature, requiring only the built-in coupling field and *no* external field. Such a device can be integrated into a two- or three-terminal setup and control over $\langle m \rangle_t$ can be achieved using a spin current generated by SOT instead of STT. Stochastic computing with such a scheme has been proposed by computer architectures [24,25,30]. The concept presented in this paper is equally applicable for magnetic tunnel junction with perpendicular anisotropies where the resistance-area (RA) product is low and where lower critical current densities can be attained exploiting the voltage control of magnetic anisotropy.

Chapter 8 Electrical control over magnetization via spin-orbit interaction

Results presented in this chapter represent the first demonstration of spin-orbit torque (SOT) switching in a small 20 nm perpendicular magnetic tunnel junction (MTJ). The layer switched by SOT has extremely high thermal stability. Magnetic recording media and MRAM target a thermal stability parameter $\Delta = E_{\text{switch}}/k_B T$ of 60-80, and the devices studied here have $\Delta = 85$, more than double that of comparable diameter MTJs switched by spin transfer torque (STT). Here I demonstrate SOT is switching in devices with the characteristics needed for magnetic random access memory (MRAM). Many earlier approaches focused on in-plane magnetized materials where the SOT switching mechanism is similar to STT, and hence rendered no advantage with regards to energy consumption, relative to current technology. I will show that switching using SOT along with a small STT current requires a current density only 15% of that required for pure STT switch. This is expected to dramatically reduce the energy consumption per switch in the memory cell from $\sim \text{pJ}$ to $\sim \text{fJ}$.

8.1 Background

Magnetic memory, sensors, and microwave devices controlled with pure spin current or spin-orbit torque have the potential for lower power dissipation and longer lifetime than those based on spin transfer torque (STT) [84], [85]. Spin-polarized charge currents can switch a metallic nanomagnet [86] or cause it precession at microwave frequencies [87], but high current densities are needed, and over time this can damage

the thin tunnel barrier. Alternatively, when a charge current passes through a heavy metal conductor, the spin Hall effect (SHE) [88], [34] leads to a pure spin current perpendicular to the charge current [89], [90]. If the spin current j_s is large enough it can switch the magnetization direction [91], [92] or generate spin waves [93], [94] in a magnetic layer above the heavy metal. The vast majority of the studies on SHE switching focus on in-plane magnetized MTJ where a charge current produces an anti-damping torque to switch the free layer magnetization, which is similar to the case of conventional STT and hence does not provide much improvement in switching energy or current density. In comparison to in-plane MTJ, pMTJ is easy to scale to smaller sizes and densities. Particularly, in CoFeB-MgO based pMTJs the interfacial effects lead to high magnetic anisotropy and thus results in high thermal stability even for smaller sizes. All such attributes are much desired for memory applications.

For a pMTJ SHE generates a spin current the anti-damping like torque component of which pulls the magnetization in-plane, thermal fluctuations can then lead to stochastic switching whereas a small external field or STT can result in deterministic switching. The other torque that the spin current generates is the field-like torque which is usually weak. Recent simulation work within a macrospin approximation, and with modified LLG equation have suggested that a pMTJ can be switched deterministically using SHE with an assist from an anti-damping like torque provided by a small STT current in a three-terminal setup [95] [96]. This STT assisted SHE switching can provide an improvement in switching time and current densities. Switching due to the SHE has been detected through the Hall voltage or resistance [93], [97], by spin torque ferromagnetic resonance (ST-FMR) [91,98,99], by the magneto-optical Kerr effect (MOKE) [96,100], and by second harmonic generation [101]. While proposed applications of the SHE involve sub-100 nm magnets, the vast majority of the experiments have been performed on larger structures because the signals are small. For example, even when the magnetic material is several microns in diameter, the transverse spin Hall voltage is on the order of

microvolts, and reducing the diameter reduces the magnitude of the signal. Many of the detection schemes require lock-in techniques, long averaging times, or angle-dependent measurements to distinguish the SHE contribution from other mechanisms [102]. Here we demonstrate an alternative detection approach where the nanomagnet is part of a tunnel junction, and the magnetoresistance is measured by conductive atomic force microscopy (C-AFM). This enables measurement of spin current switching in small devices where size and surface-dependent effects are anticipated. For example, smaller magnetic fields are needed to reverse patterned films via nucleation plus domain wall motion than by coherent rotation. Similar differences would be expected for spin current reversal, but only the larger structures have been measured. To date, no experimental demonstration of SHE switching 20 nm or smaller pMTJ with high thermal stability has been reported.

8.2 Sample information and nanofabrication of devices on Hall cross

The magnetic tunnel junctions (MTJs) were patterned from a thin film stack grown by sputtering on a silicon substrate. The stack consisted of Ta(3)/Ru(5)/Ta(4)/Co₂₀Fe₆₀B₂₀(0.8)/MgO(1.5)/Co₂₀Fe₆₀B₂₀(1.5)/Ta(5)/Ru(9), where the numbers in parentheses are the film thickness in nanometers. The process flow for fabrication of devices and Hall cross is schematically shown in Figure 8.1.

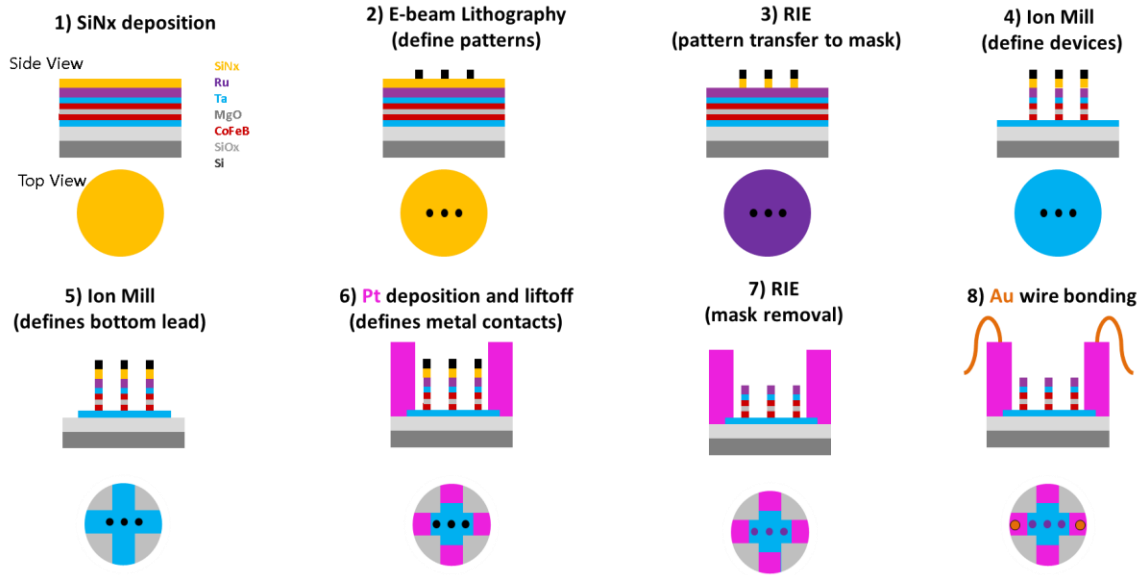


Figure 8.1 Side view and top view of the stack structure through the process flow for device and hall cross fabrication. Not to scale.

Alignment marks were defined by photolithography using NR-9 negative tone photo resist. 100 nm of Ta was sputtered to act as the alignment mark material and lifted off by sonicating in acetone. 25 nm of SiN_x was deposited as a hard mask before coating with HSQ resist for electron beam lithography. The patterns were written using a Sirion 600 SEM equipped with Nabity Nanometer Pattern Generation Software (NPGS). This pattern was transferred into the silicon nitride by CF₄/CHF₃ reactive ion etch (RIE), and then into the MTJ stack by Ar ion milling with endpoint detection, stopping in the Ta layer directly beneath the bottom CoFeB. Next, the Ta Hall cross was defined by photolithography and transferred into the bottom metallic layers by ion milling all the way to the substrate. Finally, we defined leads and bond pads by another photolithography step and deposited a 10 nm W adhesion layer and 100 nm of Au. In this way, samples were fabricated with arrays of 20-200 nm MTJs at the intersections of Hall crosses with 8.7 μm wide channels. Images of the sample at different magnifications are shown in Figure 8.2.

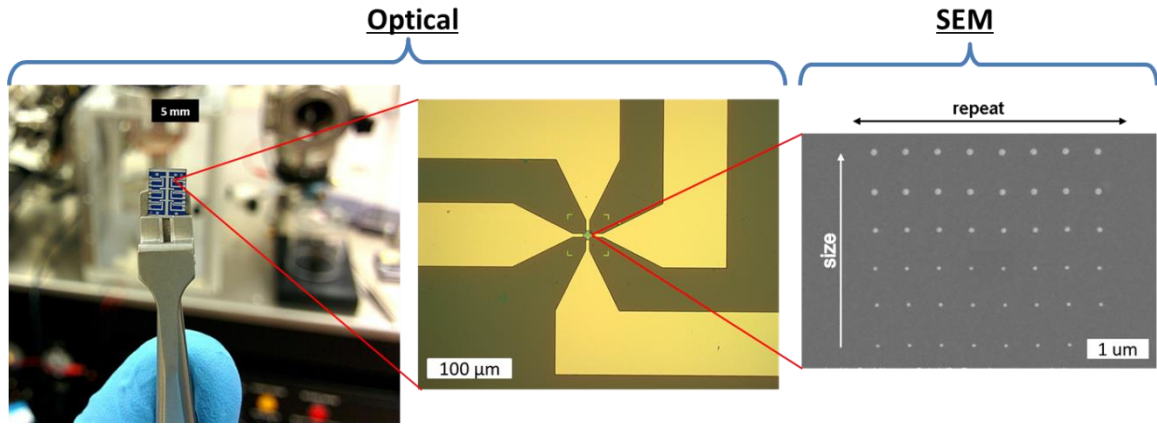


Figure 8.2 Optical and SEM images of the patterned Hall cross sample.

8.3 C-AFM setup for SHE measurements

A conductive atomic force microscope (C-AFM) was then used to measure the resistance through the MTJ nanopillars as shown in Figure 8.3. The instrument was an RHK UHV350 with R9 controller operating in contact mode, in the air at 300 K. Si-doped AFM probe tips (Arrow-FM nanoworld) were made conducting by sputtering 200 nm (nominal thickness) of Pt on a Ta adhesion layer. The details of these point contact measurements have been reported previously [78], [43], [14]. All C-AFM measurements were made in air and at room temperature. In all resistance measurements through the MTJ, the tip was connected to ground, and the voltage refers to the voltage at the base of the MTJ, where contact was made via one of the leads to the Hall cross. The TMR as a function of magnetic field or bias was measured for individual MTJs using C-AFM. A variable out-of-plane magnetic field H_{ext} up to 1300 Oe was applied by an electromagnet directly below the sample stage.

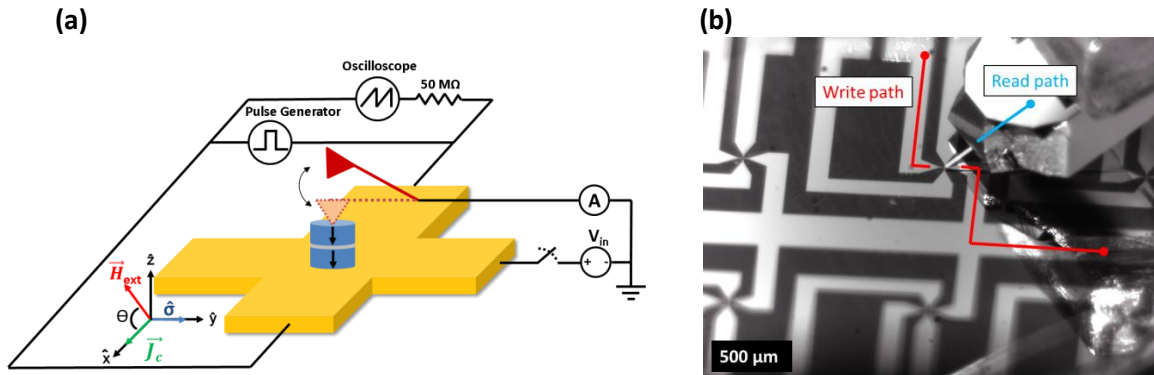


Figure 8.3 (a) Schematic of the experimental setup. A charge current pulse for SOT switching and detection of the MTJ resistance state using C-AFM. A sharp conductive tip with a ~ 20 nm radius of curvature provides a point contact on top of the MTJ. Tunnel magnetoresistance (TMR) is measured to detect the state of the device, parallel (P) or antiparallel (AP). The tip is retracted (along \hat{z}) while a charge current pulse J_c (positive along \hat{x}) passes underneath the MTJ. The spin current \hat{s} provides torque along \hat{y} . A net external field $H_{\text{ext}}=100.7$ Oe, at an angle $\theta=87.5^\circ$ is kept constant during the current pulse. The tip is brought in contact after the pulse to re-measure the TMR. (b) Optical image of C-AFM tip over the hall cross, markings show the electronic read and the write path.

Symmetry breaking is required for SOT reversal of a perpendicularly magnetized layer [91], [103], and so the sample was placed in the center of two permanent magnets to obtain a fixed in-plane magnetic field of 12.5 Oe along the charge current direction (\hat{x}). In the SOT switching experiments, the C-AFM was used to record the tunnel magnetoresistance (TMR) as a function of the field before and after current pulses through the Hall cross. In between, the tip was retracted by 100 nm in the z direction and the sample was isolated from the C-AFM voltage source. This charge current was produced using a Global Specialties 4001 Ultravariaible pulse generator, used in voltage-controlled and single shot mode. The voltage was fixed at 8 V and the pulse width 200 μs , with rise and fall times less than 15 ns. An external

oscilloscope (Tektronix model TDS 3032) with a 50 M Ω terminator was connected in parallel to the Hall cross to monitor the voltage drop. This, together with the resistance measured by a multimeter ($\sim 200\ \Omega$), was used to determine the charge current. After establishing the minimum charge current and pulse duration needed to observe SOT switching in the smallest devices, these parameters were kept constant for the remaining experiments. We then varied the current direction and the magnitude and direction ($\pm\hat{z}$) of the out-of-plane magnetic field. The perpendicular magnetic field was necessary both to initialize the MTJ in an AP state, and also to help in the deterministic switching of the high anisotropy bottom CoFeB layer using SOT.

8.4 Size vs. H_c and TMR

We observe a decrease in coercivity below 50 nm and hence predict that thermal effects and perhaps reversal as a single domain for a 20 nm device allows for switching at much lower current densities than expected. In many cases with larger nanostructures, SOT magnetization reversal occurs through domain wall motion. We observe that the current density that was sufficient to switch the 20 nm pMTJ with a switching probability $P_{sw}=1$ yields $P_{sw}<1$ (based on 50 attempts) for bigger sizes. This characteristic is noticeable in Hall resistance measurements as a function of the current amplitude, which shows curvature in the single-valued regions [98]. A slightly thicker bottom layer with reduced perpendicular anisotropy would reduce the magnetic switching field, and the required charge current density through the Hall cross, while retaining stability in the absence of a write pulse.

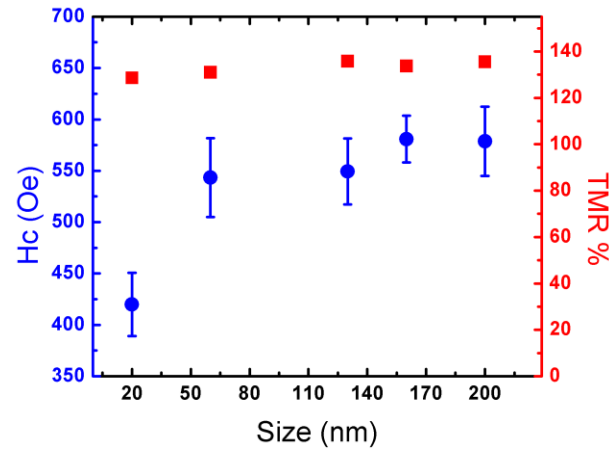


Figure 8.4 Variation in the minor loop coercivity H_c and TMR for the *top* CoFeB layer for different size devices. H_c decreases below 50 nm but is still sizeable at 20 nm. The bottom layer H_c exceeded the maximum field of the in situ electromagnet (1300 Oe) for all sizes.

8.5 SOT switching a 20 nm pMTJ

The applied field of the in situ electromagnet was not large enough to obtain major loops with reversal of both the top and bottom layers; therefore, an indirect method was used to determine the magnetization direction of the bottom CoFeB layer. This was achieved by measuring a minor loop for the top layer, where the loop shift (positive or negative) gives the direction of the stray field (down or up) due to the bottom layer. If the top layer direction is unchanged, but SOT switches the bottom layer, the magnetostatic loop shift direction reverses.

Figure 8.6 illustrates how the current maps and minor loops change following SOT switching. Figure 8.6 (a) shows an SEM image of the 20 nm device, and Figure 8.6 (b) and (c) shows the current maps for the MTJ before and after the current pulse through the Ta underlayer. Minor loops of the resistance as a function of the applied

magnetic field are also shown for the same 20 nm pMTJ, for two different directions of the bottom layer magnetization. A loop shift of 161 Oe was observed for this device size, similar observations were predicted in our previous work on magnetostatic effects in small pMTJs [43]. In between the measurements shown in Figure 8.6 (d) and (e), a perpendicular field of +100 Oe was maintained, and a charge current pulse (200 μ s, 40 mA) was passed through the heavy metal layers beneath the MTJ, switching the bottom layer. We did not observe any switching without the external out-of-plane field, suggesting the torque due to the SOT alone was not sufficient to cause magnetization reversal at 40 mA. The role of external out-of-plane field here is to reduce the required current density for SOT switching [104]. Once a switch was observed, checks were made to be sure it was not due to thermal activation as shown in Figure 8.5.

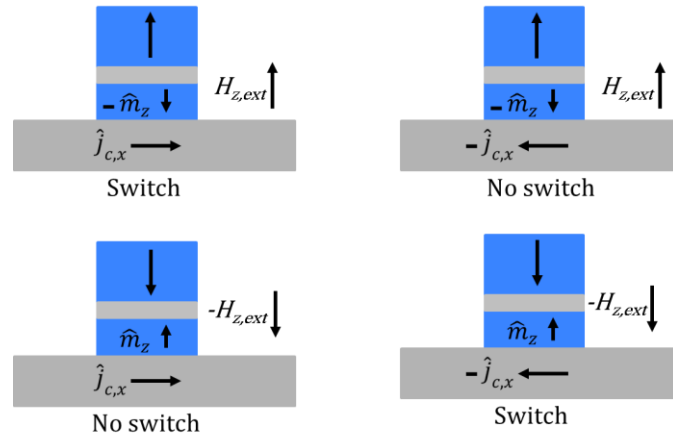


Figure 8.5 Four different combinations between the magnetization of the bottom layer and the charge current direction. Only two such combinations a SOT switch can be obtained. An external field assist was used to obtain a deterministic switch.

No switch was seen when initialized in the same AP state with the opposite current direction. However, switches were observed when both the bottom layer

magnetization and the current direction were reversed. This is consistent with expectations for SOT switching, but not for thermally assisted switching, which would be random, or for an Oersted field from the current pulse, where switching would be independent of the current direction. These data illustrate two advantages of using a MTJ in SOT switching experiments. The tunnel magnetoresistance (TMR) is 135%, and resistance changes between 20 and 50 k Ω for the two states, unlike with Hall resistance measurements, where the typical differences range from m Ω to Ω , requiring lock-in techniques and angle-dependent measurements to differentiate SOT switching from other phenomena.

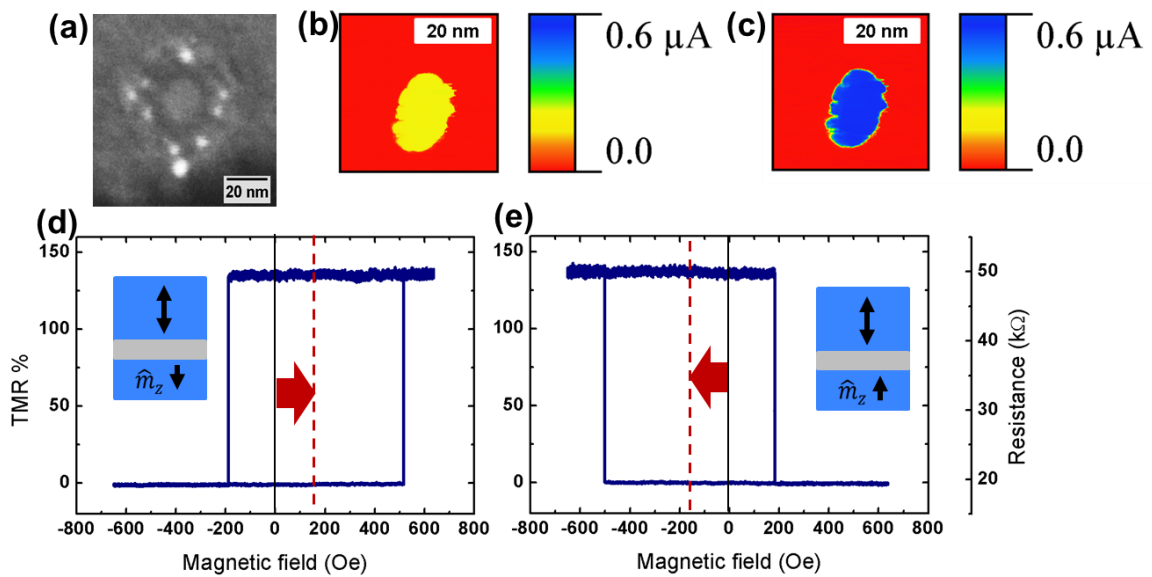


Figure 8.6 SEM image of a 20 nm device. Current maps measured using C-AFM of the device initially in the AP state (b), and after SOT switching to the P state (c). Minor loop resistance for the 20 nm MTJ at 10 mV bias, showing different loop shift directions before (d) and after (e) the current pulse. The top layer coercivity is 353 Oe, and the loop shift is 161 Oe.

High current densities required to observe SOT switching is potentially troublesome for low power applications of the SOT. In our switching experiments, the current amplitude is large because of the Ru layer below the Ta in the Hall cross base. The electrical resistivity of Ru $\sim 7.6 \text{ } \Omega\text{cm}$ [105], [106] is however much smaller than for β -Ta $\sim 190 \text{ } \Omega\text{cm}$ [92], so the vast majority of the current flows through the Ru and contributes minimally to the SOT. Since Ru is a 4d metal and the strength of spin-orbit coupling scales as Z^4 , Ru is expected to be far less efficient at transforming charge current to spin current than Ta. Moreover, the spin diffusion length in Ru is less than 4 nm [107], and so Ru would act as a sink for spin current generated in the bottom Ta layer. Assuming uniform electrical contact through the bonding pad, and ignoring oxidation, COMSOL simulations indicate a current density of $3.35 \times 10^6 \text{ A/cm}^2$ in the top Ta layer, and an additional 38% reduction in current density at the center of the cross, where the MTJs are located (see APPENDIX E). Similar reductions have been reported elsewhere [96]. The effective charge current density generating the spin current for switching is estimated to be $J_c^{SOT} = 2.39 \times 10^6 \text{ A/cm}^2$, which is comparable to values typical of STT reversal, but without having to pass a large current through the MTJ.

A second factor that impacts the SOT charge current amplitude is the high anisotropy of the adjacent CoFeB layer. Because major loops could not be measured, the effective anisotropy $K_{eff, bottom}$ was estimated indirectly. $K_{eff, top}$ was found from switching field distributions of minor loops measured multiple times [see Supplementary Information], and related to the interface anisotropy K_i , using a method that has been described previously [14]. The interface anisotropy K_i was determined from $K_i/t = K_{eff} + |K_b| + |K_s|$, where t is the thickness, the bulk anisotropy $K_b = 8.02 \times 10^6 \text{ ergs/cc}$, and the shape anisotropy $K_s = 7.1 \times 10^6 \text{ erg/cc}$. With a top layer thickness of 1.5 nm, $K_i = 2.4 \text{ erg/cm}^2$, and assuming the same K_i for the bottom layer, with thickness $t = 0.8 \text{ nm}$ leads to $K_{eff, bottom} = 1.3 \times 10^7 \text{ erg/cc}$. The PMA at the Fe/MgO

interface is largely determined by the hybridization of Fe 3d orbitals and O 2p orbitals. In our MTJ stack with large TMR, careful control of the oxidation level results in the high K_{eff} value that we observe here [20] [108]. If the bottom layer were considered as an isolated particle, its thermal stability factor $\Delta_{\text{bottom}}=85$ and the anisotropy field is $H_{\text{eff}}=24.2$ kOe. Note that the values of Δ ranging from 60 to 80 are sought after for magnetic storage media, and correspond to a data retention time > 10 years. Our results show that the SOT is strong enough to be used even with high anisotropy perpendicular magnetization materials.

8.6 Estimation of field-free critical current densities and write energies

The experiments reported here were done in a magnetic field, both to reduce the current requirements and to have deterministic switching, but by correcting for field effects, it is possible to compare SOT and STT switching. The vast majority of the demonstrations of SOT switching have been performed on MTJs with in-plane magnetization or a partial in-plane component. With pMTJs, a symmetry-breaking element is required for deterministic switching [41,96]. The SOT causes the out-of-plane magnetization to be pulled in-plane. Once the magnetization is in-plane switching can then be achieved either stochastically by external perturbations such as thermal effects, or deterministically by simultaneous application of an in-plane field. Deterministic switching can also be achieved through the STT effect [96], [101]. STT-assisted SOT switching is predicted to reduce the switching time and critical current density [41,96,109].

In our experiments an out-of-plane external field $H_{\text{z,ext}}=100$ Oe, far less than the anisotropy field $H_{\text{a, bottom}} = H_{\text{eff}} = 24.2$ kOe, was used to demonstrate deterministic switching, but we can estimate the STT current that would be needed for field-free

reversal. In a three-terminal device, the torque coming from STT would correspond to an additional current density $J_{add}^{STT} = \frac{2e}{\hbar} \cdot \frac{\alpha}{P} \cdot \frac{t_f M_s}{P} \cdot H_{z,ext} = 6.64 \times 10^4 A/cm^2$ through the device. Here e is the electron charge, \hbar is Planck's constant, the damping parameter $\alpha = 0.015$ [66], the film thickness $t_f = 0.8 nm$, $M_s = 1130$ emu/cc and the spin polarization factor $P = 0.62$, calculated using Julliere formula $TMR = 2P^2/(1-P^2)$ with $TMR = 128\%$. In contrast, for a device with thermal stability $\Delta = 85$, the critical switching current density for pure STT switching is expected to be $J_{c0}^{STT} = \frac{2e}{\hbar} \cdot \frac{\alpha}{\eta} \cdot \frac{t_f M_s}{P} \cdot H_{eff} = 1.6 \times 10^7 A/cm^2$. In our case $(J_{add}^{STT} + J_c^{SOT})/J_{c0}^{STT} \approx 0.15$, suggesting a reduction in the required current density is feasible using a STT-assisted SOT scheme.

We can also estimate the write energy per bit. From an application viewpoint, we assume an array of 20 nm devices, with 50 nm device-to-device distances on a 4 nm thick, 50 nm wide β -Ta channels. For SOT with deterministic switching, the switching time is estimated to be < 10 ns [41,96]. As discussed above, switching can be achieved with $J_c^{SOT} = 2.39 \times 10^6 A/cm^2$ through β -Ta with 190 Ωcm resistivity and $J_{add}^{STT} = 6.64 \times 10^4 A/cm^2$ through a pMTJ with $R = 20$ k Ω . This yields energy consumption per switch in a cell $E_{sw}^{SOT+STT} = \sum I^2 R t \approx 0.1$ fJ. Here the contribution due to the power dissipation from the STT current through the pMTJ is less than 10%. In contrast, the required energy per switch for the same cell using *only* STT current is estimated to be $E_{sw}^{STT} \approx 0.5$ pJ. Moreover, with STT switching the charge current passes through the high resistance MTJ, while with SOT switching it flows only through the heavy metal. When a charge current pulse travels through the Hall cross, all of the MTJs are exposed to the same spin current density. Hence multiple devices can be switched with the same voltage and current density, whereas such a scheme is impractical using STT due to high series resistance that the tunnel barriers would add. SOT could provide a dramatic reduction in energy consumption;

however, challenges remain in fabricating such devices at such small sizes and with proper interconnect to allow a three terminal read and write.

8.7 Summary

In summary, this work represents the smallest known, and highest thermal stability perpendicular magnetic device switched using SOT, more than 600 times smaller area than in the pioneering demonstration of Miron [91], and more than double the thermal stability factor of comparable diameter pMTJs switched by STT [110]. Our CAFM technique of switching detection based on TMR readout and magnetostatic loop shift is a simple way to detect switching in small devices with a large signal-to-noise ratio. The effective SOT charge current density through the Ta underlayer was less compared to that typical for STT reversal. Moreover, with field or STT assisted scheme such devices can be switched at much lower energy per write as compared to the conventional STT scheme.

Chapter 9 Electric-field Controlled Bidirectional Magnetization Switching in FePd/Ta/CoFeB SAF

Switching of perpendicular magnetic tunnel junctions (p-MTJs) with only an electric-field (E-field) has been a topic of much interest and research for realizing energy efficient and architecturally easy to integrate memory and computing devices. In perpendicular magnetic tunnel junction with perpendicular magnetic anisotropy, voltage effect can be used to manipulate the thermal stability as was shown in Chapter 5. To switch a pMTJ deterministically, however, an external driving force such as a magnetic field or a spin current is needed. This renders the VCMA effect by itself not of much advantage for achieving energy efficient (lower power than conventional STT) bidirectional switching. In this chapter, I showcase how an electric field effect in $L1_0$ FePd based FePd/Ru/FePd synthetic antiferromagnetic structure can be used to change the coupling of SAF to the free layer between Ferromagnetic and Antiferromagnetic. This E-field effect along with the VCMA effect can be used to toggle the magnetization of the free layer between parallel and anti-parallel configurations without an external magnetic field or a large current density. This simple and efficient switching mechanism may eliminate the main obstacle to the development energy efficient nonvolatile memory and can provide an attractive pathway for future MRAM technology.

This work was done in collaboration with Jianping Wang's group at University of Minnesota (UMN). The samples were grown at UMN by Delin Zhang, and the

patterning and testing of the devices was performed by me at CMU. Part of this chapter has already been submitted as an article for publication.

9.1 Introduction

The contemporary switching mechanisms to switch the magnetization of MTJs utilizes spin current through spin-transfer torque (STT) or spin-orbit torque (SOT), both of which require a current flow [52,84,85,111]. In these switching schemes a relatively large switching current densities, $J_{c,STT} \sim 10^{6-7}$ A/cm² and $J_{c,SOT} \sim 10^{7-8}$ A/cm², is needed for switching high thermal stability devices (thermal stability > 45 is sought for non-volatile memory applications). An electric field effect has been observed in bulk perpendicular magnetic materials such as FePd [112,113] and FePt [114]. However the effect is still related to the interfacial magnetic anisotropy and conceptually similar to what is observed in Ta/CoFeB/MgO based structures [52,115]. For these cases, an external magnetic field or a spin current is required to break the time-reversal symmetry of the FM layer [116]. Up until now, electric field-induced *and* the magnetic field-free *bi-directional* magnetization switching between parallel (P) and antiparallel (AP) states in p-MTJs have not been reported.

9.2 VCMA and E-field control of FM-AFM coupling in SAF

The effect of an E-field on the interfacial perpendicular magnetic anisotropy was discussed in section 2.6. For NM/FM/MgO stacks (NM and FM denote non-magnetic and ferromagnetic layer respectively) a positive (negative) V_{bias} can enhance (decrease) the i-PMA due to the depletion (accumulation) of electrons in the FM/MgO interface with V_{bias} . Here the modification of the MA from E-field originates mainly from the change of *d*-orbital hybridization of the minority spin.

Theoretical calculations also predict that the E-field can tune the interlayer exchange coupling (IEC) of the synthetic antiferromagnetic (SAF) structure [117] [118]. Specifically, both the strength and sign of IEC can be tuned either by using a ferroelectric (FE) layer to charge the interface of the FM/FE structure [90] or by inserting an insulating layer between the FM layer and spacer to change the reflectivity of the majority and minority spins [118]. A SAF structure consists of two FM layers separated by a NM spacer. The strength and sign of the IEC strongly depend on the electronic properties of the FM and spacer layers [118]. Based on the theory in Ref. [118], the strength (J) of IEC can be interpreted as the energy difference of quantum well states between FM and antiferromagnetic (AFM) coupling configurations of the two FM layers, which can be defined at $T = 0$ K as follows:

$$\frac{J}{A} = E_{FM} - E_{AFM} \cong -\frac{1}{\pi^3} \text{Im} \int d^2 k_{\parallel} \int_{-\infty}^{E_F} \Delta r_1 \Delta r_2 e^{2ik_{\perp}T} dE \quad 9.1$$

Here $\Delta r_1 = 1/2 (r_{\uparrow} - r_{\downarrow})$, where r_{\uparrow} and r_{\downarrow} are the complex reflectivity of majority spin (\uparrow) and minority spin (\downarrow) electrons at the interface, and A is the area of the interface. Positive J corresponds to FM coupling and negative J denotes AFM coupling. From equation 9.1, the E-field mainly influences the contribution of the minority spins, so the reflectivity of minority spins will also be modified. Combining equations (1) and (2), if a SAF stack includes an i-PMA structure, an E-field could lead to the transition between the AFM and FM couplings and thus cause 180° magnetization switching; The positive V_{bias} increases the MA of the Ta/CFB/MgO stack, which enhances the AFM coupling between the CFB and FePd layers, thus increasing H_c of the bottom dual SAF free layer. In contrast, a negative V_{bias}

decreases the MA of the CFB layer, which leads to the FM coupling between the CFB and FePd layers and decreases the H_c of the bottom dual SAF free layer.

In this p-MTJs stack, the perpendicular SAF (p-SAF) structure with a stack of $FM_1/NM/FM_2/MgO$ is designed as a bottom free layer based on an i-PMA $NM/FM_2/MgO$ structure. When a positive E-field (negative V_{bias}) is applied, the electrons accumulate at the FM_2/MgO interface which will decrease the MA of FM_2 layer. In this case, shifting of the Fermi energy (E_F) increases the minority spin density (d -orbitals), which enhances the reflectivity of the minority spins in the NM/FM_2 interface and leads to the FM coupling ($J_1 > 0$) following the equation 9.1. In contrast, the electrons are depleted at the FM_2/MgO interface with the negative E-field (positive V_{bias}), and the MA of FM_2 layer will be increased. In this case, the E_F shifting will decrease the minority spin density (d -orbitals), which leads to the reduction of the reflectivity of the minority spins in the NM/FM_2 interface and thus induces AFM coupling ($J_1 < 0$).

9.3 Stack preparation: p-MTJ with FePd SAF

The FePd SAF p-MTJ structures studied in this work were prepared on single crystal (001) MgO substrates by magnetron sputtering under high vacuum (base pressure $< 5.0 \times 10^{-8}$ Torr). The metal layers were deposited by DC sputtering, and the MgO tunnel barrier was deposited by RF sputtering. The FePd (3.0 nm)/Ru (1.1 nm)/FePd (3.0 nm) perpendicular synthetic antiferromagnetic stack was prepared with Cr (15.0 nm)/Pt (4.0 nm) seed layer by keeping the substrate temperature at 350 °C. The rest layers of FePd SAF p-MTJ structures with the stack of Ta(0.8)/CoFeB(1.3)/MgO(2.0)/CoFeB(1.3)/Ta(0.7)/[Pd(0.7)/Co(0.3)]₅/Pd(5.0)/ca

pping layer, where the numbers in parenthesis are thicknesses in nanometers. The capping layers are Ta (5.0 nm) and Pt (15.0 nm) (deposited for C-AFM testing) and were grown after the substrate cooled to room temperature. In this pMTJ stack the $\text{Co}_{20}\text{Fe}_{60}\text{B}_{20}(\text{CFB})/\text{Ta}/[\text{Co}/\text{Pd}]_n$ (denoted as FM_3 in the text here) acts as reference layer on the top and a bottom dual SAF free layer, $\text{FePd}/\text{Ru}/\text{FePd}$ (denoted as FM_1 in the text here) couple with CoFeB (denoted as FM_2 in the text here) below the MgO and act as a free layer. In the bottom dual SAF free layer, two L1_0 - FePd layers are antiferromagnetically coupled through a Ru spacer (FePd p-SAF).

9.4 Nanofabrication and device testing setup

The 350 °C-annealed FePd SAF p-TMJ stacks were patterned into sub-100 nm diameter MTJ pillars by using an e-beam lithography and Ar ion etching. The spin transport properties were tested by a four-probe technique for 150-nm and 500-nm diameter FePd SAF p-MTJs using a Dynacool PPMS at the different temperatures and was performed at UNM. We did patterning and testing on 35-100 nm diameters FePd SAF p-MTJs using the C-AFM setup at room temperature. A sharp AFM tip with a 20 nm conductive Pt was used to make electrical contact directly with the top of FePd SAF p-MTJ pillars. In all the measurements here the tip is grounded, and the bias voltage (positive or negative) is applied at the bottom electrode. Thus for a positive bias voltage (V_{bias}), the current flows from the bottom to the top, and for a negative V_{bias} , the current flows from the top to the bottom of FePd SAF p-MTJs for the C-AFM measurements. During the testing, a sweep rate of 150 Oe/sec was used to measure the resistance versus magnetic field (R-H) loops. A sweep rate of 500 mV/sec was used to measure the resistance versus bias voltage (R-V) loops. For resistance versus time (R-t) traces, an acquisition rate of 1 MHz was used. A variable

out-of-plane magnetic field H_{ext} up to 1300 Oe was applied by an electromagnet directly below the sample stage.

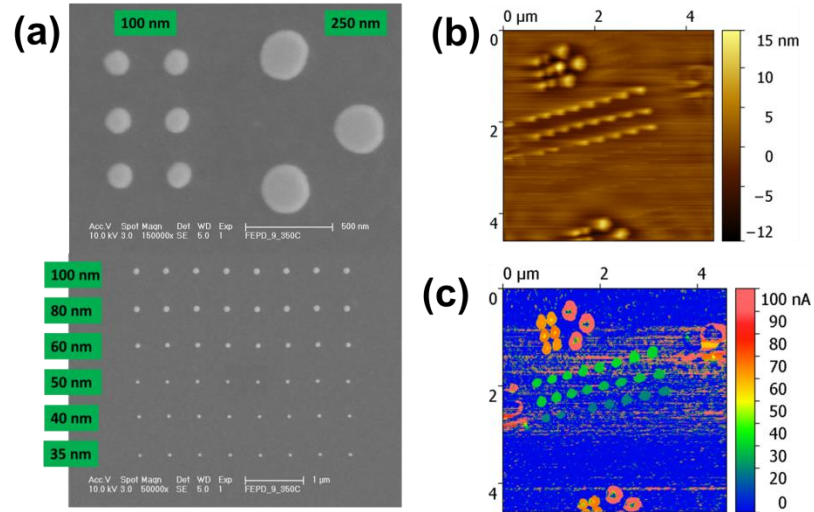


Figure 9.1 (a) SEM image of the patterned devices of different sizes. Using CAFM (b) topography map and (c) current map measured at 100 mV was obtained. Very few devices below 60 nm survived the patterning process post Ion milling due to high aspect ratio during the step as can be seen through the topography and current maps.

9.5 Variations with voltage bias and size

To quantitatively evaluate the E-field effect for the dual p-SAF free layer of FePd SAF p-MTJs, the mean H_{swf} , effective magnetic anisotropy ($K_{\text{u,eff}}$), and coefficient (ξ) of the voltage-controlled magnetic anisotropy (VCMA) of the dual p-SAF free layer were obtained by measuring minor M-H loops and fitting the switching field distribution (SFD) [14]. The minor MR-H loops of the sub-100 nm FePd SAF p-MTJ devices were measured using a conductive atomic force microscope (C-AFM) by sweeping a perpendicular H_{ext} . In all the measurements here the AFM tip is

grounded, and the V_{bias} is applied at the bottom electrode. Thus the positive (negative) V_{bias} corresponds to the negative (positive) E-field. Figure 9.3(a) shows the minor MR-H loops of 100-nm diameter FePd SAF p-MTJs at different V_{bias} ($V_{\text{bias}} = +0.75$ V, -0.1 V and -0.75 V). The positive V_{bias} enhances the H_{swf} and the negative V_{bias} reduces H_{swf} , indicating that the E-field significantly affects the MA of the bottom dual SAF free layer. Due to the stray field (dipole coupling) from the top reference layer, the shift of the minor MR-H loop was observed [14]. To obtain the SFD, multiple MR-H loops were measured at a given V_{bias} . The mean coercivity (H_c) value was obtained by fitting SFD using the Kurkijärvi-Fulton-Dunkelberger equation [14]:

$$\sigma = \left\{ \frac{1}{\tau_0 v} \exp \left[-K_{\text{eff}} V \left(1 - \frac{H M_s}{2K_{\text{eff}}} \right)^2 \right] \right\} \times \exp \left\{ - \int_0^H \frac{1}{\tau_0 v} \exp \left[\frac{-K_{\text{eff}} V}{k_b T} \left(1 - \frac{h M_s}{2K_{\text{eff}}} \right)^2 \right] dh \right\}. \quad 9.2$$

Here $\tau_0 \sim 10^{-9}$ second is the attempt time, $v \sim 350$ Oe/s is the ramping rate of H_{ext} , $M_s \sim 970$ emu/cm³ is the saturation magnetization of the bottom dual SAF free layer, k_B is the Boltzmann constant and $T = 300$ K is the testing temperature. The mean H_c as a function of V_{bias} of the bottom dual SAF free layer is summarized and depicted in Figure 9.3. H_c vs. V_{bias} exhibits a typical linear behavior corresponding to the VCMA effect, as discussed in section 2.6. The H_c value dramatically increases from ~ 145 Oe to ~ 900 Oe when the V_{bias} sweeps from -0.75 V to $+0.75$ V. This increasing H_c value is more than one order magnitude larger than that of p-MTJs with a single CFB layer as shown in Figure 9.2. For FePd SAF p-MTJs, the H_c shows a dramatic increase from 145 Oe to 900 Oe. However, the H_c only increases from 205 Oe to 290 Oe [14] and from 20 Oe to 85 Oe [16] for the CoFeB/MgO based p-MTJs.

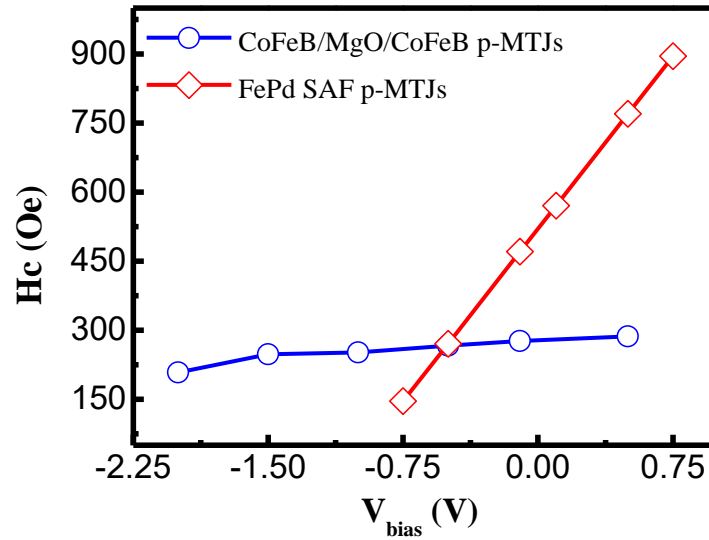


Figure 9.2 Comparison of the coercivity change with the different applied bias voltages. The bias voltage (V_{bias}) can modify the magnetic anisotropy of interfacial perpendicular magnetic materials. Here we compare the coercivity (H_c) change between FePd SAF p-MTJs and CoFeB p-MTJs with the different applied V_{bias} . For FePd SAF p-MTJs, the H_c shows a steeper change with bias than for CoFeB/MgO/CoFeB pMTJs.

The enhancement of H_c for the dual SAF free layer is attributed to the increase of the MA of CoFeB layer by the E-field, further increasing the strength of the coupling between the FePd and CFB layers. The positive V_{bias} increases the MA of the Ta/CFB/MgO stack, which enhances the AFM coupling between the CFB and FePd layers, thus increasing H_c of the bottom dual SAF free layer. In contrast, a negative V_{bias} decreases the MA of the CFB layer, which leads to the FM coupling between the CFB and FePd layers and decreases the H_c of the bottom dual SAF free layer. We also calculated $K_{u,\text{eff}}$ and evaluated ξ of the bottom dual SAF free layer at different V_{bias} values by fitting SFD using the equation 9.2. The $K_{u,\text{eff}}$ vs. V_{bias} curve is plotted in Figure 9.3(c). When V_{bias} changes from -0.75 V to +0.75 V, $K_{u,\text{eff}}$ linearly increases

from 0.15 Merg/cm³ to 0.53 Merg/cm³. The ξ value is calculated by following the equation:

$$K_{eff}(V_{bias}) = K_{eff}(0) + \xi \frac{V_{bias}}{t_{MgO}^2}, \quad 9.3$$

where $K_{eff}(0) \sim 0.395$ Merg/cm³ is the MA of the bottom dual SAF free layer with $V_{bias}=0$, t_{MgO} is the MgO thickness. By fitting the $K_{u,eff}$ curve, ξ of the bottom dual SAF free layer is evaluated to be ~ 117 fJ/Vm, which is higher than that of recent work ($\xi \sim 100$ fJ/Vm) [93,119].

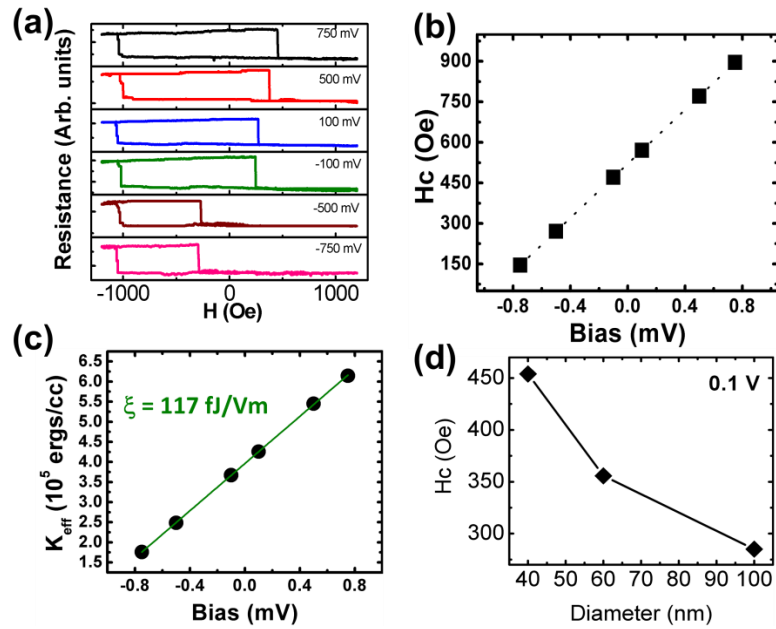


Figure 9.3 (a) The minor M-H loops of 100-nm diameter FePd SAF p-MTJ devices with the different V_{bias} swapping H_{ext} from -1200 Oe to +1200 Oe. (b) The H_c vs. V_{bias} curve and (d) the $K_{u,eff}$ vs. V_{bias} for a 100-nm diameter FePd SAF p-MTJ device. Here the H_c (coercivity) and $K_{u,eff}$ (effective magnetic anisotropy) values are obtained by fitting the switching field distribution (SFD) with the Kurkijärvi-Fulton-Dunkelberger equation. The coefficient (ξ) of the voltage-controlled magnetic anisotropy (VCMA) for 100-nm diameter FePd p-SAF p-MTJ devices was obtained

from the linear fit. (d) Effect of size on coercivity which is found to be increasing with decreasing size.

9.6 Bi-directional switching with voltage

We now investigate and demonstrate the feasibility of the E-field switching of p-MTJ devices. The current vs. V_{bias} (I-V) curve of the sub-100 nm diameter FePd SAF p-MTJ devices was measured at RT by using the same C-AFM setup without applying H_{ext} . The I-V curves were obtained by sweeping V_{bias} from -0.6 V to +0.6 V for 100-nm diameter FePd SAF p-MTJ devices annealed at 350 °C, as plotted in Figure 9.4(a). We observe a sharp magnetization switching (see zoom in figures in Figure 9.4(a)) from P to AP at a negative $V_{\text{bias}} \sim -0.46$ V ($I = -8.92$ μA), and from AP to P at positive $V_{\text{bias}} \sim +0.48$ V ($I = +8.73$ μA). The MR ratios were found to be $\sim 6.9\%$ and $\sim 3.7\%$, and the switching current densities (J_c) to be $\sim 1.13 \times 10^5$ A/cm² and $\sim 1.11 \times 10^5$ A/cm² for the P-AP state and AP-P transitions, respectively.

To further confirm the *bi-directional* magnetization switching using only E-field in FePd SAF p-MTJs, the current vs. time traces were measured while applying the voltage pulses on the same 100-nm diameter FePd SAF p-MTJ, as presented in Figure 9.4(b). During the measurements, negative and positive 0.85 V amplitude pulses were applied for *write*, and a relatively small *read* voltage of negative 0.1 V was used to monitor the changes in current values in-between the write pulses. As shown in Figure 9.4(b), we find that the p-MTJ has a high I value at the initial state (P state), after passing a negative writing pulse of -0.85 V, the device switches to an AP state and a low I was observed at the *read* voltage. Then, when a negative writing pulse with an amplitude of +0.85 V voltage was passed, the device switches back to P state and a high current was observed at the *read* voltage. These switching results

match the above-discussed mechanism of E-field switching of p-MTJs. Also, because of the large RA product ($\sim 30 \text{ k}\Omega \cdot \mu\text{m}^2$) and low switching current density $\sim 1.1 \times 10^5 \text{ A/cm}^2$, the effect of STT effect should be negligible [120].

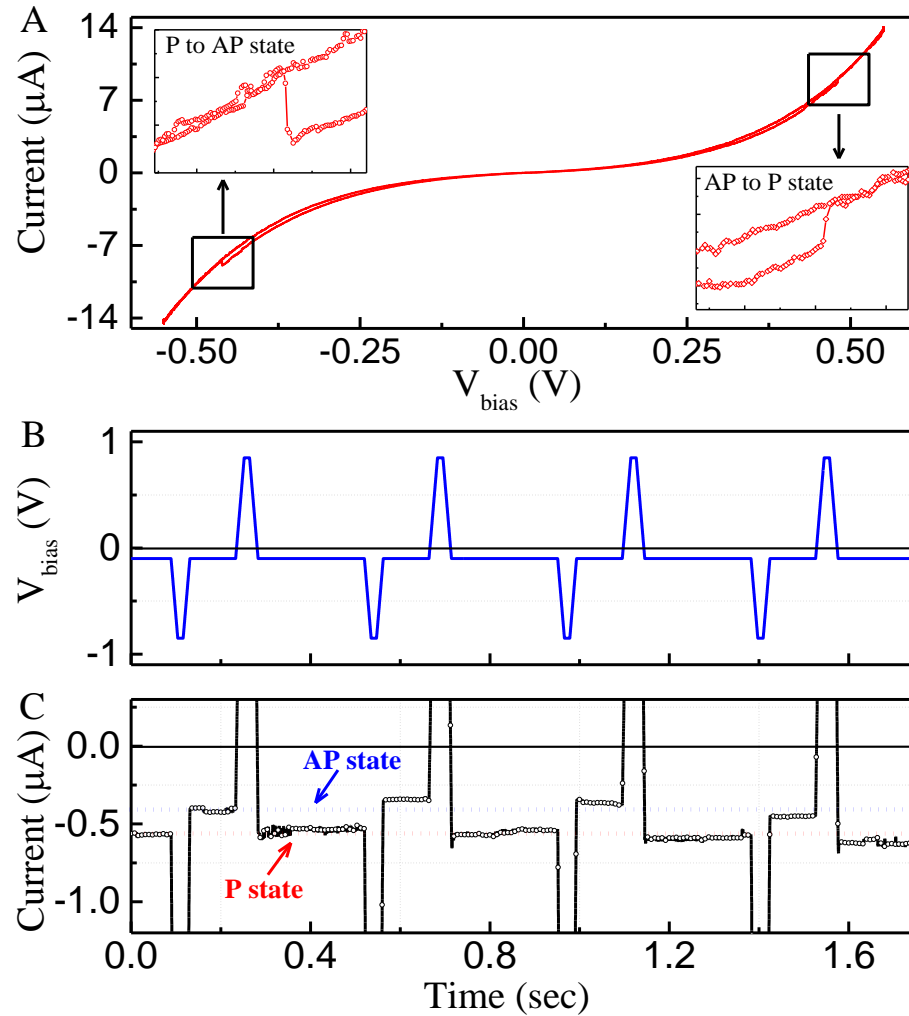


Figure 9.4 E-field switching of p-MTJs. (A) The current vs. voltage (I-V) curve for a 100-nm diameter FePd SAF p-MTJ device measured by C-AFM without applying H_{ext} . The sharp magnetization switching was observed by applying a negative $V_{\text{bias}} \sim -0.46 \text{ V}$ ($I = -8.92 \mu\text{A}$) and a positive $V_{\text{bias}} \sim +0.48 \text{ V}$ ($I = +8.73 \mu\text{A}$), respectively, indicating the AP-P and P-AP states. (B) The current vs. time trace measured for the same device.

The negative and positive 0.85 V voltage pulse was applied for a *write* operation, and a positive 0.1 V was used to *read* the current levels to check the device state (P or AP state).

E-field switching of the magnetization is also observed in 35-nm diameter FePd SAF p-MTJs annealed at 400 °C. The thermal stability of this device satisfies the requirement of the integrated temperature (the BEOL process) for the existing CMOS technologies. The magnetization switches from P-AP state and AP-P state at $V_{\text{bias}} \sim -2.06$ V ($I = -8.8$ μA) and $V_{\text{bias}} \sim +1.8$ V ($I = +5.7$ μA), respectively. The corresponding current density was $J_c \sim 1.4 \times 10^5$ A/cm² for AP-P switch and $J_c \sim 2.2 \times 10^5$ A/cm² for P-AP switch.

9.7 Conclusion

The use of electric fields allows for much lower power dissipation since in principle no charge current is required for E-field controlled devices to operate, this effect can then reduce or even eliminate Ohmic losses and Joule heating. In fact, E-field control of magnetization has the potential to replace STT and SHE in perhaps similar way how BJTs (current controlled technology) were radically replaced by CMOS (electric-field-controlled technology) mainly because of concerns about power dissipation with increasing computing needs. In conclusion, we designed and demonstrated a reversible *bi-directional* magnetization switching mechanism using only an E-field in the p-MTJs with the bottom dual SAF free layer. These experimental results present a crucial step towards E-field controlled spin memory and logic devices with the ultra-low energy and the potential for easy integration with the current CMOS technologies.

APPENDIX A

Building in-plane and out-of-plane electromagnets

I built a pair of electromagnets that were integrated with the C-AFM setup to introduce the capability of measurement of devices with in-plane magnetization and for experiments where an in-plane field is needed. The electromagnets can produce up to 500 Oe field with the Kepco power supply with 4 A current (for the max field) flowing through wires. Care should be taken as not to let the current flow for long duration (>1 mins) in continuation to avoid melting of the enamel of the wires. The gauge lengths of the wires used in the electromagnet are 125 AWG and especially have a high-temperature tolerance (from Belden). High tolerance to heat is required because often during measurements multiple field sweeps need to be made which leads to a buildup of heat and an increase of temperature in the electromagnet. To hold the electromagnets in place and avoid any vibration to the CAFM setup itself a 3D printed assembly was made to hold the assembly inside the CAFM box. Ahmed Abdelgawad helped me with the CAD designing of the assembly, and 3D printing was done using NVBots printer at IDeATe department located in the basement of Hunt Library at CMU.

I also made improvements to the design of out-of-plane electromagnets by optimizing the length and number of turns in the winding that could fit inside the limited cylindrical space inside the stage for the sample holder. The original design

of the electromagnet and pole piece was made by former student Stephan Piotrowski, and more details can be found in his Ph.D. thesis. A lathe was used to do the winding by placing the core of electromagnet between two cylindrical teflon pieces. This method helps to tightly wrap a long length of wire around pole piece with ease. The new electromagnet design can produce up to 1300 Oe field in comparison to the original design which went up to 800 Oe. The field measurements were done using both hall probes and hand held gauss meter.

If building electromagnets in future for the C-AFM extreme care must be taken to ensure both electrical and vibration isolation. Any short between the winding and the CAFM stage could potentially damage the sample and the CAFM electronics!

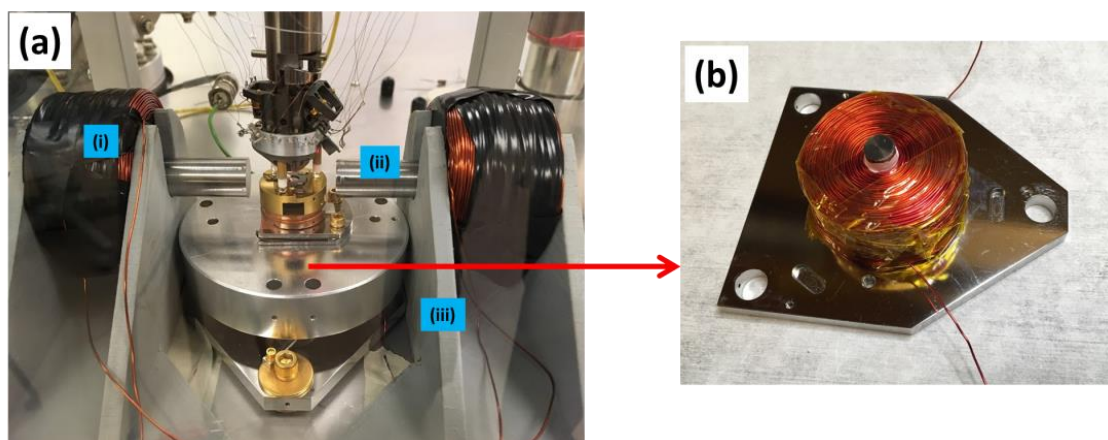


Figure A.1 (a) In-plane electromagnet setup around the CAFM scan head can produce up to 600 Oe field. A pair of electromagnets (i) with pole pieces (ii) directs an in-plane field through the sample placed at the center. The holder for the electromagnets (iii) was made using 3D printing to hold the pair of electromagnets snugly inside the CAFM box without any direct contact with the assembly itself to minimize vibrations. (b) An out-of-plane field of up to 1300 Oe field is produced by the electromagnet below the sample holder.

APPENDIX B

Improvements in Ion milling procedure

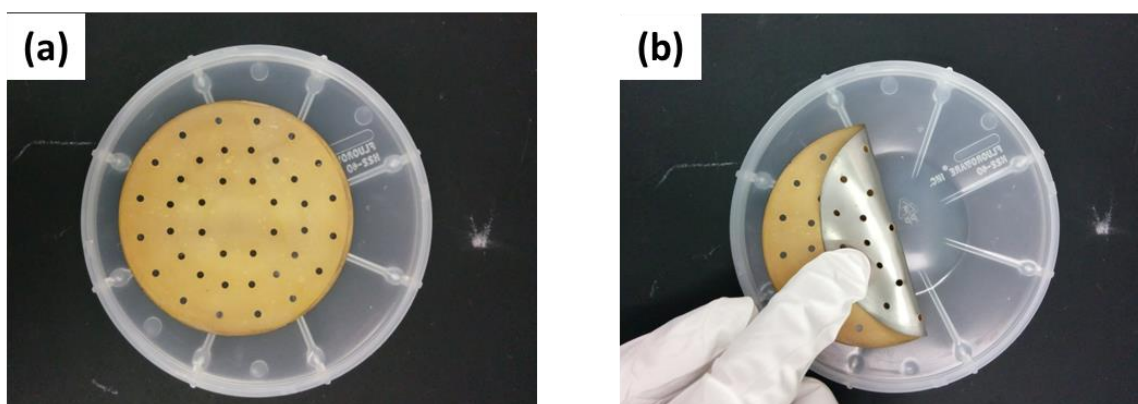


Figure B.1 Dry chuck used a heat sink before and after excessive heating causing the diffused silver colloidal particles to surface; this lowers the thermal conduction property and can cause damages to the sample during ion milling.

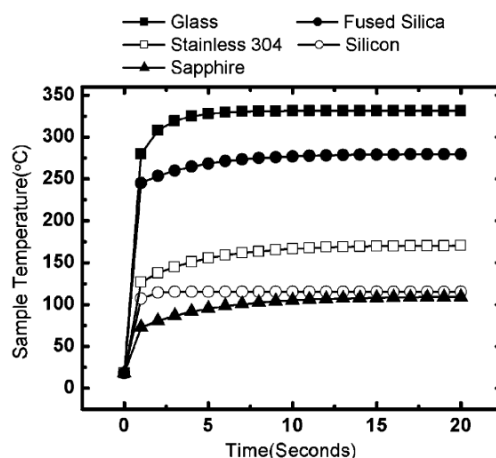


Figure B.2 Effect of sample temperature upon exposure to ion beam during ion milling step for different materials deposited on a Si wafer. This figure is taken from Park et al.

2007 [121]. To avoid damage due to excessive heating, the sample shutter should be opened and closed with some intervals to allow the sample and the dry chuck to cool down to tolerable temperature limits.

APPENDIX C Shape anisotropy

When an external field is applied the magnetization in a bulk or thin film ferromagnet tends to align itself with the externally applied field, this causes magnetic poles to be formed along the field direction. These magnetic poles generate a demagnetizing field H_{demag} , the direction of which is opposite to M and H_{ext} . The effective magnetic field (H_{eff}) that exists inside the ferromagnet can, therefore, be described as $H_{\text{eff}} = H_{\text{ext}} - H_{\text{demag}}$. The demagnetization field depends directly on the geometry of the magnetic volume under consideration. The following discussion is for simpler geometries such as spheres and ellipsoids.

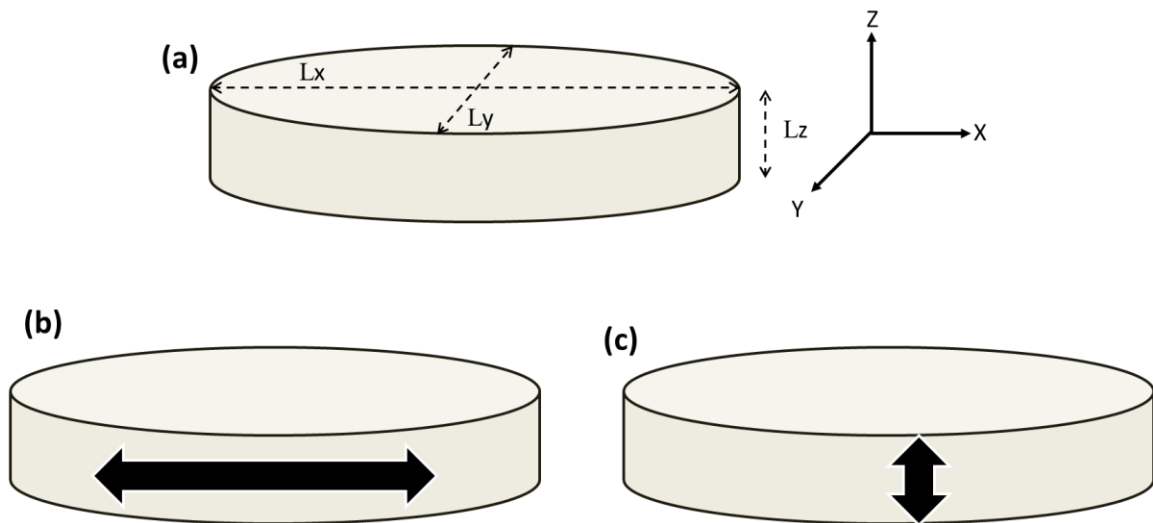


Figure C.1 (a) Elliptical shaped magnetic free layer cell with lengths L_x , L_y , and L_z along the different directions. Here z-axis corresponds to the out of plane axis (hard axis), and x-axis is the in-plane axis (easy axis). (b) Magnetization in-plane (c) Magnetization out of the plane.

Here we take a rectangular thin film and approximate it as an ellipsoid with a minimal thickness along the z-axis. A rigorous discussion of demagnetizing fields in case of cylinders may be found in the theoretical work by Chen et al. [122]. When the magnetization is aligned along the x-axis, the demagnetizing field $H_{\text{demag}} = N_x M$. Here, N_x is the demagnetizing factor along the x-axis. Similarly, for the cases where M is parallel to the y-axis and M parallel to the z-axis, $H_d = N_y M$, and $H_d = N_z M$, respectively. Here, $0 < N_\delta < 1$ ($\delta = x, y, z$) and $N_x + N_y + N_z = 1$ in the ellipsoidal approximation. If the shape of ferromagnet is a sphere, $N_x = N_y = N_z = 1/3$. If the ferromagnet is a thin film extending in x-y plane, such that the lateral sizes are much larger than the film thickness, we have $N_x = 0$ and $N_z = 1$.

For device geometries in MRAM, the free layer consists of a thin ferromagnetic film with a typical thickness of a few nanometers. Usually, the free layer is fabricated into an elliptical or circular shape with a typical lateral size ranging from micrometers down to a few tens of nanometers. If the long axis of an ellipse is considered along the x-axis, the typical dimensions $l_x > l_y \gg l_z$ results in the relation $0 < N_x < N_y \ll N_z < 1$. The shape anisotropy energy K_{shape} due to demagnetizing fields in the direction δ ($\delta = x, y, z$) can be expressed as:

$$K_{\text{shape}} = - \sum_{\delta} \mu_0 \cdot M_s \cdot \frac{H_{d\delta}}{2} = \sum_{\delta} \mu_0 \cdot N_{\delta} \cdot \frac{M_s^2}{2} \quad \text{D.1}$$

Since the magnetostatic energy is proportional to the demagnetization factor N_δ , the energy of the free layer is the lowest when M is aligned along the film plane and is parallel to the long axis of the ellipse, whereas the energy is highest when M is perpendicular to the film plane. If the single domain state is retained at $H_{\text{ext}} = 0$, the magnetization is aligned along the longer axis (x-axis in this case) of the ellipse due to the lowest demagnetizing energy. This axis is termed “easy axis.” On the other

hand, it is usually hard to direct the magnetization perpendicular to the plane because of the large demagnetizing energy. The perpendicular axis, in this case, is called “hard axis.” The shape of ferromagnet thus yields magnetic anisotropy energy termed as the “shape anisotropy” and is expressed as

$$K_{Shape} = \mu_0 \cdot (N_y - N_x) \cdot \frac{M_s^2}{2} \quad \mathbf{D.2}$$

Unfortunately, there are no simple expressions for the demagnetizing coefficients N_x and N_y for an elliptical cylinder as a function of its dimensions (width w , thickness t , length $AR \cdot w$, where AR is the in-plane aspect ratio). These coefficients are complex functions of elliptic integrals and must be tabulated or numerically calculated.

APPENDIX D

Chip Carriers and Wire Bonding

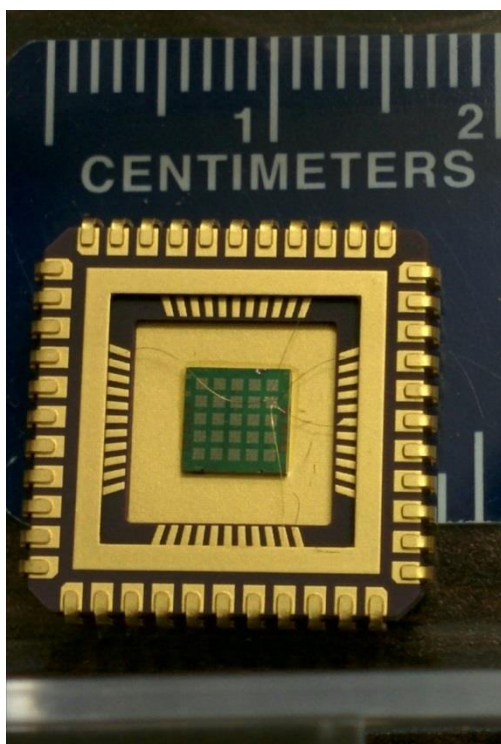


Figure D.1 Chip carrier connected to the hardwired devices through gold wires

Commercially available chip carriers model#CCJ04801 from Spectrum-Semi were used to make electrical connections to the hard-wired devices as discussed in Chapter 6. Wire bonding was done using West Bond Wire Bonder setup in Ben Hunt's Lab in the physics department. Wire leads with micro-grabber were then used to make electrical connections to the devices. This allows for the high-speed electronic measurements through the devices which otherwise is not possible with the C-AFM due to the limitation set by the high RC time constant of the scan head (~ 200 ns).

APPENDIX E

Current Spread in Hall cross- COMSOL Simulations

I performed COMSOL simulations to estimate current density distribution within 8.7 μm wide Ta(3)Ru(5)/Ta(4) trilayer system that was used to pass charge current for generation of spin hall current. Due to hall cross type geometry of the current channel (see inset) a 38% reduction in current density was found at the center of the Hall cross below where the magnetic tunnel junctions were fabricated. From simulations, we estimate the effective charge current density $J_{c,\text{Ta}}=2.7 \times 10^6 \text{ A/cm}^2$ flowing through the top Ta layer that then generates the spin current. Using $\Theta_{\text{SHE}}=0.15$, spin current involved in SHE switching was estimated to be $J_{s,\text{Ta}}=3.5 \times 10^5 \text{ A/cm}^2$.

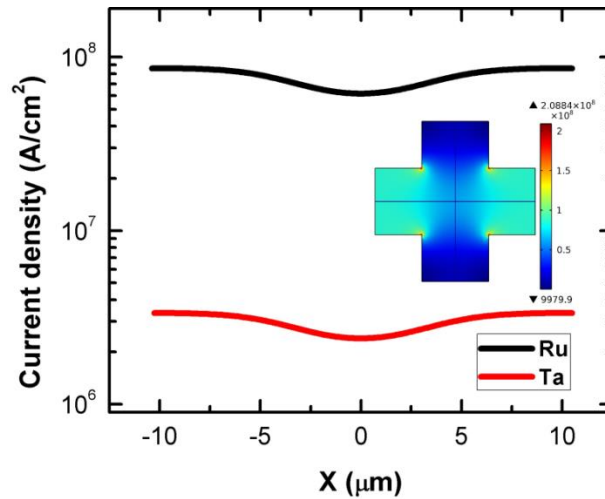


Figure E.1 Current density as measured at the center of the hall cross (see inset) perpendicular to the current flow.

REFERENCES

- [1] E. R. Evarts, L. Cao, D. S. Ricketts, N. D. Rizzo, J. A. Bain, and S. A. Majetich, *Appl. Phys. Lett.* **95**, 132510 (2009).
- [2] M. Julliere, *Phys. Lett. A* **54**, 225 (1975).
- [3] J. Bland and C. Anthony, *Ultrathin Magnetic Structures I* (Springer, 1994).
- [4] J. G. Simmons, *J. Appl. Phys.* **34**, 1793 (1963).
- [5] R. Meservey and P. M. Tedrow, *Phys. Rep.* **238**, 173 (1994).
- [6] W. H. Butler and X.-G. Zhang, in *Ultrathin Magn. Struct. III* (Springer-Verlag, Berlin/Heidelberg, n.d.), pp. 5–50.
- [7] W. H. Butler, X.-G. Zhang, T. C. Schulthess, and J. M. MacLaren, *Phys. Rev. B* **63**, 54416 (2001).
- [8] J. Mathon and A. Umerski, *Phys. Rev. B - Condens. Matter Mater. Phys.* **63**, 220403 (2001).
- [9] S. S. P. Parkin, C. Kaiser, A. Panchula, P. M. Rice, B. Hughes, M. Samant, and S. H. Yang, *Nat. Mater.* **3**, 862 (2004).
- [10] Shinji Yuasa, Rie Matsumoto, Akio Fukushima, Hitoshi Kubota, Taro Nagahama, D. D. Djayaprawira, Koji Tsunekawa, Hiroki Maehara, Yoshinori Nagamine, Motonobu Nagai, Shinji Yamagata, Yoshishige Suzuki, Masaki Mizuguchi, A. M. Deac, and Koji Ando, in *2006 IEEE Nanotechnol. Mater. Devices Conf.* (IEEE, 2006), pp. 186–187.
- [11] Z. Diao, M. Pakala, A. Panchula, Y. Ding, D. Apalkov, L.-C. Wang, E. Chen, and Y. Huai, *J. Appl. Phys.* **99**, 08G510 (2006).
- [12] M. K. Niranjana, C.-G. Duan, S. S. Jaswal, and E. Y. Tsymlal, *Appl. Phys. Lett.* **96**, 222504 (2010).

- [13] T. Maruyama, Y. Shiota, T. Nozaki, K. Ohta, N. Toda, M. Mizuguchi, A. A. Tulapurkar, T. Shinjo, M. Shiraishi, S. Mizukami, Y. Ando, and Y. Suzuki, *Nat. Nanotechnol.* **4**, 158 (2009).
- [14] S. K. Piotrowski, M. Bapna, S. D. Oberdick, S. A. Majetich, M. Li, C. L. Chien, R. Ahmed, and R. H. Victora, *Phys. Rev. B-Condensed Matter* **94**, 14404 (2016).
- [15] D. C. Worledge, D. W. Abraham, J. Z. Sun, P. L. Trouilloud, J. Nowak, S. Brown, M. C. Gaidis, E. J. O. Sullivan, and R. P. Robertazzi, *Appl. Phys. Lett.* **98**, 22501 (2011).
- [16] W.-G. Wang, M. Li, S. Hageman, and C. L. Chien, *Nat. Mater.* **64**, 64 (2012).
- [17] H. Sato, M. Yamanouchi, K. Miura, S. Ikeda, H. D. Gan, K. Mizunuma, R. Koizumi, F. Matsukura, and H. Ohno, *Appl. Phys. Lett.* **99**, 42501 (2011).
- [18] W. G. Wang and C. L. Chien, *J. Phys. D. Appl. Phys.* **46**, 74004 (2013).
- [19] T. Liu, J. W. Cai, and L. Sun, *AIP Adv.* **2**, 32151 (2012).
- [20] H. Almasi, M. Xu, Y. Xu, T. Newhouse-Illige, and W. G. Wang, *Appl. Phys. Lett.* **109**, 32401 (2016).
- [21] J. Sun, *Phys. Rev. B* **62**, 570 (2000).
- [22] S. K. Piotrowski, M. Bapna, H. Almasi, W.-G. Wang, L. Tryputen, C. A. Ross, M. Li, C.-L. Chien, and S. A. Majetich, *IEEE Trans. Magn.* **51**, 4400504 (2015).
- [23] B. Sutton, K. Y. Camsari, B. Behin-Aein, and S. Datta, *Sci. Rep.* **7**, 44370 (2017).
- [24] N. Rangarajan, A. Parthasarathy, and S. Rakheja, *J. Appl. Phys.* **121**, 223905 (2017).
- [25] K. Y. Camsari, R. Faria, B. M. Sutton, and S. Datta, *Phys. Rev. X* **7**, 31014 (2017).
- [26] H. Lee, F. Ebrahimi, P. K. Amiri, and K. L. Wang, *AIP Adv.* **7**, 55934 (2017).
- [27] W. H. Choi, Y. Lv, J. Kim, A. Deshpande, G. Kang, J. P. Wang, and C. H. Kim, in *Tech. Dig. - Int. Electron Devices Meet. IEDM* (2015), p. 12.5.1-12.5.4.
- [28] B. Parks, M. Bapna, J. Igbokwe, H. Almasi, W. Wang, S. A. S. A. Majetich, I. Julianne, H. Almasi, W. Weigang, and S. A. S. A. Majetich, *AIP Adv.* **8**, 55903 (2018).

- [29] A. F. Vincent, J. Larroque, N. Locatelli, N. Ben Romdhane, O. Bichler, C. Gamrat, W. S. Zhao, J.-O. Klein, S. Galdin-Retailleau, and D. Querlioz, *IEEE Trans. Biomed. Circuits Syst.* **9**, 166 (2015).
- [30] A. Sengupta, P. Panda, P. Wijesinghe, Y. Kim, and K. Roy, *Sci. Rep.* **6**, 30039 (2016).
- [31] H. Sato, M. Yamanouchi, S. Ikeda, S. Fukami, F. Matsukura, and H. Ohno, *Appl. Phys. Lett.* **101**, 22414 (2012).
- [32] K. Watanabe, B. Jinnai, S. Fukami, H. Sato, and H. Ohno, *Nat. Commun.* **9**, 663 (2018).
- [33] J. J. Nowak, R. P. Robertazzi, J. Z. Sun, G. Hu, J.-H. Park, J. Lee, A. J. Annunziata, G. P. Lauer, R. Kothandaraman, E. J. O’Sullivan, P. L. Trouilloud, Y. Kim, and D. C. Worledge, *IEEE Magn. Lett.* **7**, 1 (2016).
- [34] J. E. Hirsch, *Phys. Rev. Lett.* **83**, 1834 (1999).
- [35] L. Berger, *Phys. Rev. B* **54**, 9353 (1996).
- [36] J. C. Slonczewski, *J. Magn. Magn. Mater.* **159**, L1 (1996).
- [37] E. B. Myers, F. J. Albert, J. C. Sankey, E. Bonet, R. A. Buhrman, and D. C. Ralph, *Phys. Rev. Lett.* **89**, 196801 (2002).
- [38] J. Z. Sun, M. C. Gaidis, G. Hu, E. J. O’Sullivan, S. L. Brown, J. J. Nowak, P. L. Trouilloud, and D. C. Worledge, *J. Appl. Phys.* **105**, 07D109 (2009).
- [39] G. Yu, P. Upadhyaya, Y. Fan, J. G. Alzate, W. Jiang, K. L. Wong, S. Takei, S. A. Bender, L.-T. Te Chang, Y. Jiang, M. Lang, J. Tang, Y. Wang, Y. Tserkovnyak, P. K. Amiri, and K. L. Wang, *Nat. Nanotechnol.* **9**, 548 (2014).
- [40] A. Van Den Brink, S. Cosemans, S. Cornelissen, M. Manfrini, A. Vaysset, W. Van Roy, T. Min, H. J. M. Swagten, and B. Koopmans, *Appl. Phys. Lett.* **104**, 12403 (2014).
- [41] Z. Wang, W. Zhao, E. Deng, J.-O. Klein, and C. Chappert, *J. Phys. D: Appl. Phys.* **48**, 65001 (2015).
- [42] J. P. Cascales, D. Herranz, J. L. Sambricio, U. Ebels, J. A. Katine, and F. G. Aliev,

- Appl. Phys. Lett. **102**, 92404 (2013).
- [43] M. Bapna, S. K. Piotrowski, S. D. Oberdick, M. Li, C.-L. Chien, and S. A. Majetich, Appl. Phys. Lett. **108**, 22406 (2016).
 - [44] Y. Yuzhelevski, M. Yuzhelevski, and G. Jung, Rev. Sci. Instrum. **71**, 1681 (2000).
 - [45] D. E. Endean, C. T. Weigelt, R. H. Victora, and E. D. Dahlberg, Appl. Phys. Lett. **104**, 252408 (2014).
 - [46] H. Sato, E. C. I. Enobio, S. Ikeda, S. Fukami, S. Kanai, F. Matsukura, and H. Ohno, Appl. Phys. Lett. **105**, 62403 (2014).
 - [47] J. Norpoth, S. Dreyer, and Ch, J. Phys. D. Appl. Phys. **41**, 25001 (2008).
 - [48] J. M. Shaw, S. E. Russek, T. Thomson, M. J. Donohue, B. D. Terris, O. Hellwig, E. Dobisz, and M. L. Schneider, Phys. Rev. B **78**, 24414 (2008).
 - [49] J. Cucchiara, Y. Henry, D. Ravelosona, D. Lacour, E. E. Fullerton, J. A. Katine, and S. Mangin, Appl. Phys. Lett. **94**, 12502 (2009).
 - [50] D. B. Gopman, D. Bedeau, S. Mangin, E. E. Fullerton, J. A. Katine, and A. D. Kent, Appl. Phys. Lett. **100**, 62404 (2012).
 - [51] T. Miyajima, T. Ibusuki, S. Umehara, M. Sato, S. Eguchi, M. Tsukada, and Y. Kataoka, Appl. Phys. Lett. **94**, 122501 (2009).
 - [52] S. Ikeda, K. Miura, H. Yamamoto, K. Mizunuma, H. D. Gan, M. Endo, S. Kanai, J. Hayakawa, F. Matsukura, and H. Ohno, Nat. Mater. **9**, 721 (2010).
 - [53] H. Meng, W. H. Lum, R. Sbiaa, S. Y. H. Lua, and H. K. Tan, J. Appl. Phys. **110**, 33904 (2011).
 - [54] W. X. Wang, Y. Yang, H. Naganuma, Y. Ando, R. C. Yu, and X. F. Han, Appl. Phys. Lett. **99**, 12502 (2011).
 - [55] Q. L. Ma, S. Iihama, T. Kubota, X. M. Zhang, S. Mizukami, Y. Ando, and T. Miyazaki, Appl. Phys. Lett. **101**, 122414 (2012).
 - [56] J.-H. Kim, J.-B. Lee, G.-G. An, S.-M. Yang, W.-S. Chung, H.-S. Park, and J.-P. Hong, Sci. Rep. **5**, 16903 (2015).
 - [57] H. Almasi, D. R. Hickey, T. Newhouse-Illige, M. Xu, M. R. Rosales, S. Nahar, J.

- T. Held, K. A. Mkhoyan, and W. G. Wang, Appl. Phys. Lett. **106**, 182406 (2015).
- [58] J. Zhou, W. Zhao, S. Peng, J. Qiao, J.-O. Klein, X. Lin, Y. Zhang, and A. Bournel, IEEE Trans. Magn. **53**, 1 (2017).
- [59] L. Thomas, G. Jan, J. Zhu, H. Liu, Y.-J. Lee, S. Le, R.-Y. Tong, K. Pi, Y.-J. Wang, D. Shen, R. He, J. Haq, J. Teng, V. Lam, K. Huang, T. Zhong, T. Torng, and P.-K. Wang, J. Appl. Phys. **115**, 172615 (2014).
- [60] R. Dorrance, J. G. Alzate, S. S. Cherepov, P. Upadhyaya, I. N. Krivorotov, J. A. Katine, J. Langer, K. L. Wang, P. K. Amiri, and D. Markovic, IEEE Electron Device Lett. **34**, 753 (2013).
- [61] H. D. Gan, H. Sato, M. Yamanouchi, S. Ikeda, K. Miura, R. Koizumi, F. Matsukura, and H. Ohno, Appl. Phys. Lett. **99**, 252507 (2011).
- [62] B. R. Gaines, in *Proc. April 18-20, 1967, Spring Jt. Comput. Conf. - AFIPS '67* (ACM Press, New York, New York, USA, 1967), p. 149.
- [63] B. Jun and P. Kocher, Cryptogr. Res. Inc. White Pap. **27**, 1 (1999).
- [64] M. Bucci, L. Germani, R. Luzzi, A. Trifiletti, and M. Varanono, IEEE Trans. Comput. **52**, 403 (2003).
- [65] S. G. Bae, Y. Kim, Y. Park, and C. Kim, IEEE J. Solid-State Circuits **52**, 605 (2017).
- [66] T. Devolder, P. H. Ducrot, J. P. Adam, I. Barisic, N. Vernier, J. Kim, B. Ockert, and D. Ravelosona, Appl. Phys. Lett. **102**, 22407 (2013).
- [67] A. Gayen, G. K. Prasad, S. Mallik, S. Bedanta, and A. Perumal, J. Alloys Compd. **694**, 823 (2017).
- [68] Q. Xiang, Z. Wen, H. Sukegawa, S. Kasai, T. Seki, T. Kubota, K. Takanashi, and S. Mitani, J. Phys. D: Appl. Phys. **50**, 40LT04 (2017).
- [69] L. E. Bassham, A. L. Rukhin, J. Soto, J. R. Nechvatal, M. E. Smid, S. D. Leigh, M. Levenson, M. Vangel, N. A. Heckert, and D. L. Banks, Spec. Publ. (NIST SP) - 800-22 Rev 1a (2010).
- [70] I. N. Krivorotov, N. C. Emley, A. G. F. Garcia, J. C. Sankey, S. I. Kiselev, D. C.

- Ralph, and R. A. Buhrman, Phys. Rev. Lett. **93**, 166603 (2004).
- [71] Z. Li and S. Zhang, Phys. Rev. B - Condens. Matter Mater. Phys. **69**, 134416 (2004).
 - [72] A. Sengupta, C. M. Liyanagedera, B. Jung, and K. Roy, Sci. Rep. **7**, 11764 (2017).
 - [73] A. Fukushima, T. Seki, K. Yakushiji, H. Kubota, H. Imamura, S. Yuasa, and K. Ando, Appl. Phys. Express **7**, 83001 (2014).
 - [74] E. Chen, D. Apalkov, Z. Diao, A. Driskill-Smith, D. Druist, D. Lottis, V. Nikitin, X. Tang, S. Watts, S. Wang, S. A. Wolf, A. W. Ghosh, J. W. Lu, S. J. Poon, M. Stan, W. H. Butler, S. Gupta, C. K. A. Mewes, T. Mewes, and P. B. Visscher, IEEE Trans. Magn. **46**, 1873 (2010).
 - [75] N. Locatelli, A. Mizrahi, A. Accioly, R. Matsumoto, A. Fukushima, H. Kubota, S. Yuasa, V. Cros, L. G. Pereira, D. Querlioz, J. V. Kim, and J. Grolier, Phys. Rev. Appl. **2**, 34009 (2014).
 - [76] Won Ho Choi, Yang Lv, Jongyeon Kim, A. Deshpande, Gyuseong Kang, Jian-Ping Wang, and C. H. Kim, in *2014 IEEE Int. Electron Devices Meet.* (IEEE, 2014), p. 12.5.1-12.5.4.
 - [77] M. Bapna and S. A. Majetich, Appl. Phys. Lett. **111**, 243107 (2017).
 - [78] S. K. Piotrowski, M. F. Matty, and S. A. Majetich, IEEE Trans. Magn. **50**, 2303704 (2014).
 - [79] L. Néel, C. R. Hebd. Seances Acad. Sci. **255**, 1676 (1962).
 - [80] M. Cormier, K. March, J. Ferré, A. Mougin, and W. Raberg, Phys. Rev. B **77**, 54419 (2008).
 - [81] F. A. Shah, V. K. Sankar, P. Li, G. Csaba, E. Chen, and G. H. Bernstein, J. Appl. Phys. **115**, 17B902 (2014).
 - [82] W. F. Brown, Phys. Rev. **130**, 1677 (1963).
 - [83] C. E. Shannon, Bell Syst. Tech. J. **27**, 379 (1948).
 - [84] A. Brataas, A. D. Kent, and H. Ohno, Nat. Mater. **11**, 372 (2012).
 - [85] C. F. Pai, L. Liu, Y. Li, H. W. Tseng, D. C. Ralph, and R. A. Buhrman, Appl.

- Phys. Lett. **101**, 122404 (2012).
- [86] J. Katine, F. Albert, R. Buhrman, E. Myers, and D. Ralph, Phys. Rev. Lett. **84**, 3149 (2000).
 - [87] S. I. Kiselev, J. C. Sankey, I. N. Krivorotov, N. C. Emley, R. J. Schoelkopf, R. A. Buhrman, and D. C. Ralph, Nature **425**, 380 (2003).
 - [88] M. I. D'yakonov and V. I. Perel', JETP Lett. **13**, 467 (1971).
 - [89] E. Saitoh, M. Ueda, H. Miyajima, and G. Tatara, Appl. Phys. Lett. **88**, 182509 (2006).
 - [90] K. Ando, S. Takahashi, K. Harii, K. Sasage, J. Ieda, S. Maekawa, and E. Saitoh, Phys. Rev. Lett. **101**, 36601 (2008).
 - [91] I. M. Miron, K. Garello, G. Gaudin, P.-J. Zermatten, M. V Costache, S. Auffret, S. Bandiera, B. Rodmacq, A. Schuhl, and P. Gambardella, Nature **476**, 189 (2011).
 - [92] L. Liu, C.-F. Pai, Y. Li, H. W. Tseng, D. C. Ralph, and R. A. Buhrman, Science (80-.). **336**, 555 (2012).
 - [93] Y. Kajiwara, K. Harii, S. Takahashi, J. Ohe, K. Uchida, M. Mizuguchi, H. Umezawa, H. Kawai, K. Ando, K. Takanashi, S. Maekawa, and E. Saitoh, Nature **464**, 262 (2010).
 - [94] B. Heinrich, C. Burrowes, E. Montoya, B. Kardasz, E. Girt, Y. Y. Song, Y. Sun, and M. Wu, Phys. Rev. Lett. **107**, 66604 (2011).
 - [95] Z. Wang, W. Zhao, E. Deng, J. Klein, and C. Chappert, in *2015 IEEE Int. Magn. Conf. INTERMAG 2015* (2015).
 - [96] A. van den Brink, G. Vermijs, A. Solignac, J. Koo, J. T. Kohlhepp, H. J. M. Swagten, and B. Koopmans, Nat. Commun. **7**, 10854 (2016).
 - [97] K. Garello, I. M. Miron, C. O. Avci, F. Freimuth, Y. Mokrousov, S. Blügel, S. Auffret, O. Boulle, G. Gaudin, and P. Gambardella, Nat. Nanotechnol. **8**, 587 (2013).
 - [98] L. Liu, T. Moriyama, D. C. Ralph, and R. A. Buhrman, Phys. Rev. Lett. **106**, 36601 (2011).

- [99] D. Fang, H. Kurebayashi, J. Wunderlich, K. Výborný, L. P. Zârbo, R. P. Campion, A. Casiraghi, B. L. Gallagher, T. Jungwirth, and A. J. Ferguson, *Nat. Nanotechnol.* **6**, 413 (2011).
- [100] G. Yu, P. Upadhyaya, K. L. Wong, W. Jiang, J. G. Alzate, J. Tang, P. K. Amiri, and K. L. Wang, *Phys. Rev. B* **89**, 104421 (2014).
- [101] A. Pattabi, Z. Gu, J. Gorchon, Y. Yang, J. Finley, O. J. Lee, H. A. Raziq, S. Salahuddin, and J. Bokor, *Appl. Phys. Lett.* **107**, 152404 (2015).
- [102] J. Wunderlich, *Nat. Mater.* **16**, 284 (2017).
- [103] D. MacNeill, G. M. Stiehl, M. H. D. Guimaraes, R. A. Buhrman, J. Park, and D. C. Ralph, *Nat. Phys.* **13**, 300 (2016).
- [104] L. Liu, O. J. Lee, T. J. Gudmundsen, D. C. Ralph, and R. A. Buhrman, *Phys. Rev. Lett.* **109**, 96602 (2012).
- [105] S. Dutta, K. Sankaran, K. Moors, G. Pourtois, S. Van Elshocht, J. Bömmels, W. Vandervorst, Z. Tokei, and C. Adelmann, *J. Appl. Phys.* **122**, 25107 (2017).
- [106] J. W. Arblaster, *Johnson Matthey Technol. Rev.* **60**, 179 (2016).
- [107] S. Yakata, Y. Ando, T. Miyazaki, and S. Mizukami, *Japanese J. Appl. Physics, Part 1 Regul. Pap. Short Notes Rev. Pap.* **45**, 3892 (2006).
- [108] H. Almasi, C. L. Sun, X. Li, T. Newhouse-Illige, C. Bi, K. C. Price, S. Nahar, C. Grezes, Q. Hu, P. Khalili Amiri, K. L. Wang, P. M. Voyles, and W. G. Wang, *J. Appl. Phys.* **121**, 153902 (2017).
- [109] K.-S. Lee, S.-W. Lee, B.-C. Min, and K.-J. Lee, *Appl. Phys. Lett.* **102**, 112410 (2013).
- [110] M. Gajek, J. J. Nowak, J. Z. Sun, P. L. Trouilloud, E. J. O’Sullivan, D. W. Abraham, M. C. Gaidis, G. Hu, S. Brown, Y. Zhu, R. P. Robertazzi, W. J. Gallagher, and D. C. Worledge, *Appl. Phys. Lett.* **100**, 132408 (2012).
- [111] A. R. Mellnik, J. S. Lee, A. Richardella, J. L. Grab, P. J. Mintun, M. H. Fischer, A. Vaezi, A. Manchon, E.-A. Kim, N. Samarth, and D. C. Ralph, *Nature* **511**, 449 (2014).

- [112] T. Nozaki, A. K.-R. W. Skowroński, V. Zayets, Y. Shiota, S. Tamaru, H. Kubota, A. Fukushima, S. Yuasa, and Y. Suzuki, *Phys. Rev. Appl.* **5**, 44006 (2016).
- [113] F. Bonell, S. Murakami, Y. Shiota, T. Nozaki, T. Shinjo, and Y. Suzuki, *Appl. Phys. Lett.* **98**, 232510 (2011).
- [114] T. Seki, M. Kohda, J. Nitta, and K. Takanashi, *Appl. Phys. Lett.* **98**, 212505 (2011).
- [115] S. Kanai, M. Yamanouchi, S. Ikeda, Y. Nakatani, F. Matsukura, and H. Ohno, *Appl. Phys. Lett.* **101**, 122403 (2012).
- [116] F. Matsukura, Y. Tokura, and H. Ohno, *Nat. Nanotechnol.* **10**, 209 (2015).
- [117] M. Fechner, P. Zahn, S. Ostanin, M. Bibes, and I. Mertig, *Phys. Rev. Lett.* **108**, 197206 (2012).
- [118] P. Bruno, *Phys. Rev. B* **52**, 411 (1995).
- [119] Z. Wen, H. Sukegawa, T. Seki, T. Kubota, K. Takanashi, and S. Mitani, *Sci. Rep.* **7**, 45026 (2017).
- [120] Y. Shiota, S. Miwa, T. Nozaki, F. Bonell, N. Mizuochi, T. Shinjo, H. Kubota, S. Yuasa, and Y. Suzuki, *Appl. Phys. Lett.* **101**, 102406 (2012).
- [121] Y. M. Park, D. S. Ko, K. W. Yi, I. Petrov, and Y. W. Kim, *Ultramicroscopy* **107**, 663 (2007).
- [122] D.-X. Chen, J. A. Brug, and R. B. Goldfarb, *IEEE Trans. Magn.* **27**, 3601 (1991).